New Proton Radioactivity Measurements

Richard J. Irvine

Thesis submitted for the degree of Doctor of Philosophy

Department of Physics and Astronomy

University of Edinburgh

1998

Abstract

A series of experiments were carried out at Argonne National Laboratory to search for examples of proton emission from ground and low-lying states in odd-Z nuclei at the proton drip-line. Recoils from fusion evaporation reactions were separated from other reaction products and dispersed according to their mass to charge ratio by the Fragment Mass Analyser, before being implanted into a double-sided silicon strip detector system, where their subsequent particle decays (proton or alpha) were measured.

Proton emission from ^{157}Ta was measured for the first time, with a proton energy of 927 $\pm$ 7 keV and a half-life 10.1 $\pm$ 0.4 ms, This was assigned to a 3.4 $\pm$ 1.2 % proton branch from the $s_{1/2}$ ground state on the basis of comparisons of measured half-lives with those calculated using barrier penetration codes. Two new proton lines were observed from the $s_{1/2}$ ground state and $h_{11/2}$ state in ^{161}Re, with energies of 1192 $\pm$ 6 keV and 1315 $\pm$ 7 keV and half-lives of 0.37 $\pm$ 0.04 ms and 16 $\pm$ 1 ms, respectively. The proton branching ratios from these states were measured at 100 $\pm$ 7 % and 4.8 $\pm$ 0.6 %, respectively. New proton lines were also measured from states in ^{171}Au and ^{167}Ir. Proton radioactivity from the ground state of the deformed nucleus ^{141}Ho was measured with an energy of 1169 $\pm$ 8 keV and a half-life of 4.2 $\pm$ 0.4 ms and was assigned to the $7/2^-[532]$ Nilsson orbital on the basis of proton decay rate calculated using a deformed model of the nucleus.

Recent theoretical calculations which incorporate the above results, are presented and discussed, along with a new model for calculating spectroscopic factors for spherical nuclei in the region $65 \leq Z \leq 81$. The effect of a large deformation on proton decay rates is discussed with reference to ^{141}Ho.

Declaration

The experiments described in this thesis were carried out by myself and fellow collaborators. The data analysis is my own work and interpretation of the results was carried out by me and other members of the collaboration.

Richard Irvine

Acknowledgments

I would like to thank all members of the Edinburgh Nuclear Physics Group for their support and help on this project. Particular thanks must go to my supervisor, Phil Woods, for his encouragement, advice and enthusiasm which made the research both interesting and enjoyable. Thanks also to Cary Davids and Darek Seweryniak from Argonne, who spent much time and energy ensuring the success of the experiments, and to Tom Davinson whose technical advice was invaluable.

Funding for this PhD research was provided by the Engineering and Physical Sciences Research Council.

Contents

List of Figures

Chapter 1

Direct Proton Emission

1.1 Introduction

Beyond the proton and neutron drip-lines nuclei are energetically unstable to the spontaneous emission of a nucleon from their ground state. The onset of direct nucleon emission from nuclear ground states represents one of the fundamental limits of nuclear stability, as beyond the drip-lines, half-lives of nuclei drop rapidly, making their experimental observation and study extremely difficult. Figure 1.1 shows the chart of nuclides with the narrow band of stable isotopes marked by black squares. At low masses the stable nuclei have an approximately equal proton number (Z) and neutron number (N), but they become more neutron rich at higher masses due to the increasing influence of the repulsive Coulomb force between the constituent protons.

On either side of this stable region, nuclei undergo β-decay, which involves either the creation and ejection of an electron (or positron) or the capture of an atomic electron by the nucleus (only in proton-rich nuclei). These processes reduce a neutron or proton excess, bringing the nucleus closer to stability. β decay is allowed for small differences in parent and daughter binding energies. Further from stability, the energy available for decays increases and the β decay half-lives

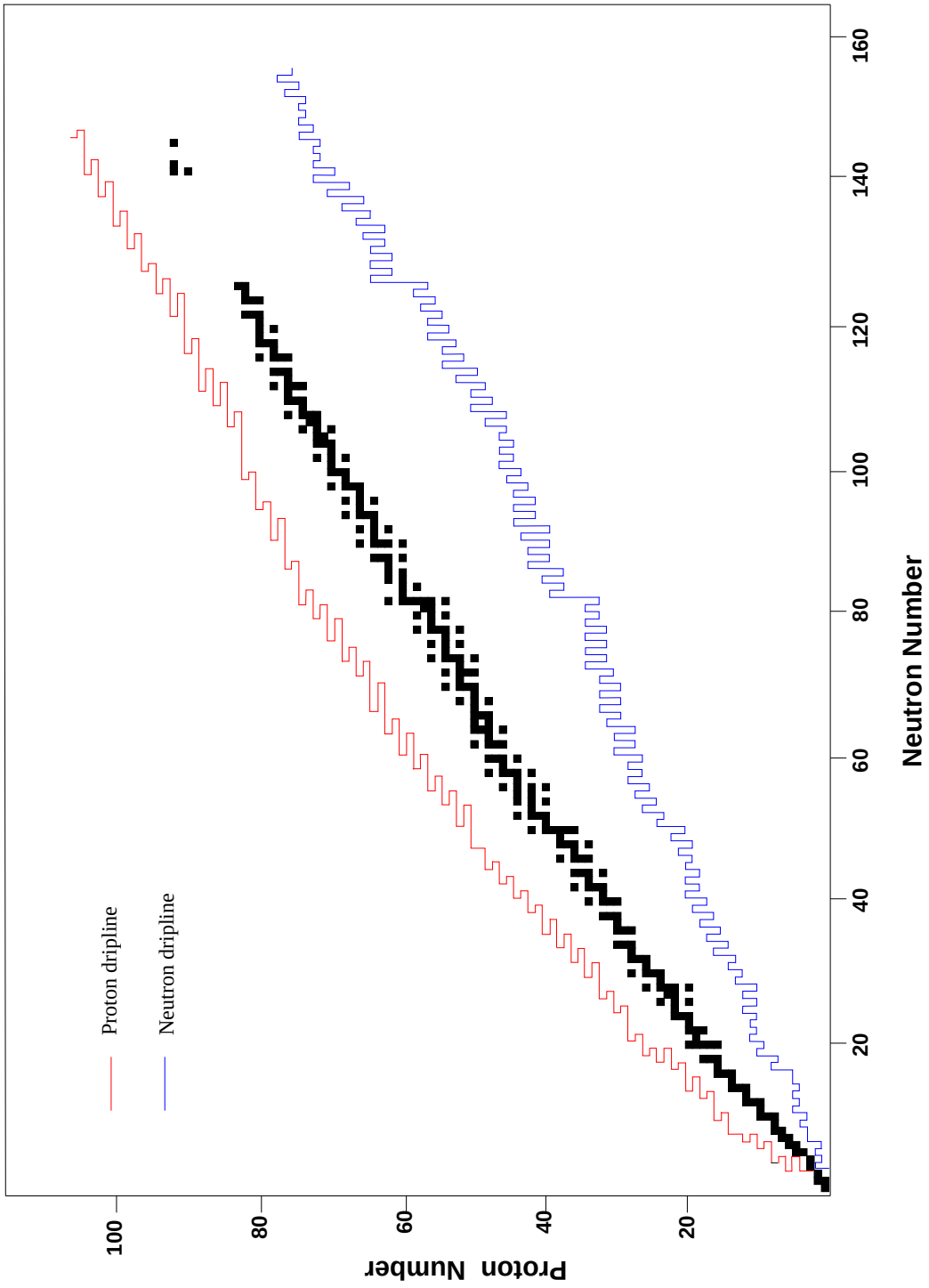

Figure 1.1: The chart of the nuclides. Stable isotopes are shown as black squares and the proton and neutron driplines as calculated by Möller *et al.* [Möl95] are indicated by the coloured lines.

correspondingly decrease, though quite modestly compared to alpha decay (see figure 1.2). However, other decay modes now become possible. β delayed nucleon emission can occur. In this process the initial β decay populates an excited state in the daughter nucleus which is unstable to the emission of one or more nucleons. The nucleon emission itself occurs very quickly, competing with γ emission, so that the whole decay occurs with a half-life characteristic of the β decay. Decay modes such as βp, βn and $\beta\alpha$ have been widely studied [Poe89] but analysis is often complicated by a high density of excited states, with spacings smaller than experimentally achievable energy resolutions. This results in spectra with a broad energy distribution.

The effect of Coulomb repulsion becomes increasingly important at higher masses due to the Coulomb potential energy increasing at a faster rate (as Z^2) than the nuclear binding energy (approximately as the mass number A). In heavier, proton-rich nuclides this results in spontaneous alpha emission which competes with beta decay. Alpha emission shows a much greater sensitivity to the available

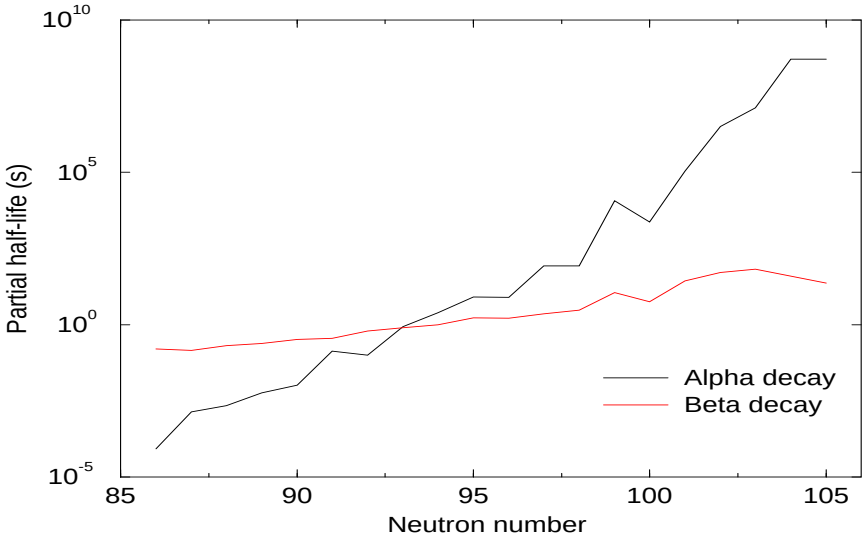

Fig 1.2: Partial alpha and beta decay half-lives for neutron-deficient isotopes of iridium, as calculated by Möller *et al.*[Möl97].

energy than β emission and the former quickly dominates moving further from stability. This is shown clearly in figure 1.2 which shows the alpha and beta partial half-lives for neutron-deficient isotopes of iridium (Z=77) from the tables of Möller *et al.* [Möl97]. Between neutron numbers 86 and 105 the beta decay partial half-life drops by around 2 orders of magnitude compared to 13 orders of magnitude for alpha decay. For highly proton-rich nuclei above N=83, alpha emission is the dominant decay mode.

Also shown in figure 1.1 are the proton and neutron drip-lines as predicted by the calculations of Möller *et al.* [Möl95]. They represent the nuclei where proton or neutron decay becomes energetically allowed ($Q_p>0$ or $Q_n>0$). Beyond the driplines partial half-lives for nucleon emission drop far more quickly than those for alpha and beta decay and this decay mode quickly dominates over them. Unlike alpha decay, direct proton or neutron emission requires no preformation of a cluster of nucleons within the nuclear surface. This simplifies its theoretical treatment, allowing new insights into nuclear structure. In particular, proton decay rates (and neutron resonance widths) are very sensitive to the orbital angular momentum of the nucleon. The determination of proton decay half-lives for a range of nuclei allows a unique insight into level orderings and the effects of deformation for nuclei much further from stability than previously possible. As is evident in figure 1.1, the proton drip-line lies much closer to stability than the neutron drip-line, a consequence of the extra Coulomb repulsion between the nucleus and a proton, although this interaction also effectively provides a potential barrier which hinders immediate emission of an unbound proton.

The experimental study of nuclei near the neutron drip-line is hindered by the relative remoteness of it and the difficulty of accessing it for even moderately high values of Z. Despite this, highly neutron-rich nuclei have provided much interesting physics including the neutron halo of ^{11}Li, discovered by Tanihata *et al.* [Tan85] at Berkeley. This very weakly bound system was found to have an unexpectedly

large cross-section which was attributed to a large matter radius associated with two very loosely bound valence neutrons. Nuclei lying beyond the drip-line can exist as short-lived resonances and are studied using direct reaction mechanisms. However, the measurement of direct neutron emission presents great experimental difficulties, not least its inaccessibility as mentioned above. The neutron drip-line has probably only been mapped up to Z=9 and it is unlikely that this will be extended much in the near future.

No conclusive evidence for proton halos exists [Tan88,Cso93], and the Coulomb barrier will tend to suppress extended proton wavefunctions. However this Coulomb barrier, combined with the centrifugal barrier, also hinders the immediate emission of an unbound proton from a nucleus, and for heavier nuclei (Z $>$ 50), decays can occur on a timescale long enough ($> 1\mu$s) to allow detection using current separator techniques. Lower-Z nuclei have a relatively low Coulomb barrier and exist only as short-lived resonances which cannot be observed directly but which are studied using direct reaction mechanisms. The use of radioactive beams has facilitated the study of such nuclei and the proton drip-line has now been mapped up to Z=21. Knowledge of nuclear properties in this region is required for an understanding of nucleosynthesis and energy generation in explosive hydrogen burning, thought to occur in nova explosions [Cha92,Woo97]. The reaction networks associated with such astrophysical processes are the focus of much current work.

In order to study proton unbound nuclei directly however, the search must concentrate on those nuclides with an expected half-life in the range (10^{-6} – 1s) to which current experiments are sensitive. At present, all observed ground state proton emitters have had Z$>$50. The study of this phenomenon allows us to extend our understanding of mass systematics and test existing models at the limit of nuclear stability. New proton radioactivity measurements for nuclei in regions of high expected deformation allow us to refine and develop theories of

the decay mechanism.

1.2 Production of Neutron Deficient Nuclei

A variety of techniques have been used with differing success over the last few decades to produce nuclei close to the proton drip-line. Transfer reactions, such as (^{4}He, ^{8}He) and (π^+,π^-) have been used to produce very light proton-rich nuclei, but these methods are limited to only these low-Z isotopes, since elsewhere the drip-line lies so far from stability. Projectile fragmentation has shown a more general application and has been used with great success at GANIL and the NSCL (examples in [Bor91, Moh91]) to search for drip-line nuclei up to about mass 100. High energy neutron-deficient beams are fragmented and the ions detected by their time of flight and energy loss in implantation detectors. The proton induced target spallation technique has been used at ISOLDE to study a wide range of proton-rich nuclei (example in [Hag79]), but ion release times are generally too long (usually $>$ 1s) to study proton decay, since many drip-line nuclei in the region of interest exhibit α-decays with sub-100ms half-lives. Fusion-evaporation has been by far the most successful method of producing intermediate and heavy nuclei close to and beyond the proton dripline. Indeed, all examples of ground state proton emitters observed so far have been produced in such reactions. Access to the proton drip-line is made easier by beam and target both being proton rich relative to heavier stable nuclei because the valley of stability veers towards the neutron rich side at higher masses.

However, such experiments are not without difficulty, as demonstrated by the quite small number of proton emitters identified until relatively recently. The first problem is accessing the proton drip-line, finding a method of synthesising these highly neutron-deficient nuclei with sufficient cross-section to allow their observation. Compound nuclei produced in these reactions favourably evaporate

protons over neutrons, so cross-sections for the production of nuclei beyond the proton drip-line are often very low. Candidate nuclei are produced among a sea of other reaction products and unreacted beam particles which would drown any decay signals detected, so any experimental system must incorporate a device to reject this massive background while maintaining as high a transmission as possible for those nuclei of interest. Additionally, the assignment of any observed decay to a parent nucleus requires some method of identifying the recoil nuclei. The detection system must also be as sensitive as possible to short half-lives since proton transition rates increase very quickly beyond the proton drip-line as this decay mode dominates over any others.

During the 1960s Macfarlane had searched for neutron-deficient nuclei in the region close to the N=82 shell closure using light ion fusion reactions and a helium-jet transport system [Mac65]. The highly neutron-deficient nuclei ^{155,156}Lu and ^{157,158}Hf were produced but the use of a low mass beam made impossible the observation of nuclei sufficiently far from stability to exhibit proton decay. The technique also limited the observation of nuclei to those with half-lives $>$ 30ms.

1.3 The Search for Proton Radioactivity

Initially it was expected that proton radioactivity from isomeric states in nuclei bound to ground state proton emission would be the best source of information on the decay mode since these nuclei would be closer to stability and hence easier to produce. However, strong γ-ray competition and very high angular momentum barriers in these states made the search difficult, though proton emission from ^{53m}Co [Jac70] was observed as an unforeseen result of some β-delayed proton experiments. No other examples of such nuclei were found so the focus moved to ground state proton emitters. Early experimenters were restricted by the limited number and low mass of projectile isotopes available, making it difficult to form

compound nuclei near the proton drip-line. Even if proton emitters were being produced, the low energy background from intense alpha groups produced in the reaction would have made the observation of the weak proton groups very difficult.

It was not until the use of heavy ion fusion evaporation reactions combined with in-flight separation of reaction products from the primary beam that ground state proton radioactivity was observed. The short transport time through in-flight separators ($\sim$ 1 μs) removed the half-life restrictions imposed by gas transport techniques. The development of ever more sophisticated separation and detection systems, described in the following sections, greatly increased our ability to study nuclei with much smaller production cross-sections.

1.3.1 Early Proton Decay Experiments

Proton radioactivity from a nuclear ground state was first discovered by Hofmann *et al.* [Hof81] using the UNILAC accelerator at GSI in Darmstadt, Germany. Developments in accelerator technology and, in particular ion-source techniques, allowed the acceleration of many more isotopes, removing the restriction on projectile species which had hindered earlier searches. The reaction of a ^{58}Ni beam on a ^{96}Ru target was used to produce the compound nucleus ^{154}Hf* at an excitation energy of 47 MeV. Reaction products then entered the SHIP in-flight velocity separator [Mun79] in which reaction residues are separated from the primary beam, before being implanted into a position sensitive silicon detector system. A low intensity, low energy line was observed in the decay spectrum far below the energies of the α-lines. On the basis of measured excitation functions and cross-sections the decay was assigned to ^{151}Lu. A later experiment [Hof82] confirmed the proton character of the line by a ΔE-E measurement and measured the energy of the proton to be 1233 $\pm$ 3 keV. The half-life was measured at 85 $\pm$ 10 ms indicating the proton comes from the $h_{11/2}$ orbital in the parent (see section 2.2.1).

The SHIP velocity filter uses two electric and four magnetic dipoles together

with two quadrupole triplets to separate reaction products from the faster moving beam particles. Flight time through the 11m long separator is typically around a microsecond and the total transmission efficiency through the filter varies from 3 - 20 % depending on the reaction channel. Beam suppression is also reaction dependent but is usually $>10^8$. In the SHIP experiments described, the recoiling residues passed out of the separator and were implanted into an array of one-dimensional position sensitive silicon detectors which recorded the energy, time and position of each implantation event and any subsequent decay events. Implant-decay discrimination was achieved using secondary electron transmission detectors in front of the silicon detectors. Implant-decay correlations were made by identifying events happening in the same position within a certain time window. Sensitivity to short half-lives was improved by 'switching off' the beam for 15ms between 5ms beam pulses, and to longer half-lives by using a rotating cylinder in front of the detectors to block evaporation residues for $\sim$ 300 ms intervals. Although this detection set-up was a big improvement on previous systems, by virtue of its sensitivity to far shorter half-lives by use of non-chemically selective transportation of activity, it was somewhat limited by the absence of an identifying mechanism for the recoil ions, which resulted in difficulty in identifying the origins of decay lines.

Klepper *et al.* [Kle82] used the on-line mass separator at GSI to search for proton emitters in the reaction ^{58}Ni + ^{92}Mo $\longrightarrow$ ^{150}Yb*. The technique used a tantalum catcher foil to stop the evaporation residues and the release time from the foil limited the search to nuclei with half-lives $>$ 100 ms. The mass separator provided unambiguous assignment of the implanted ion to a particular mass group, facilitating the identification of decay lines. A line with energy 1044 $\pm$ 25 keV and half-life 0.42 $\pm$ s was observed and assigned to the proton decay of ^{147}Tm on the basis of the mass determination provided by the mass separator along with energy and cross-section considerations.

Experimenters at the Munich Tandem Plus Post-Accelerator developed the Fast Catcher Detection System which was capable of seeing decays with half-lives down to 10 ns. Evaporation residues were collected by a catcher foil lying downstream of an annular gas detector. Their subsequent decays were measured by the gas detector during beam pauses. Faestermann *et al.* [Fae84] reported the discovery of proton radioactivities from ^{113}Cs and ^{109}I using this system. However, efficiencies were too low and background too high to detect other proton decaying nuclei with lower production cross-sections.

A series of experiments were performed at SHIP, remeasuring all of the proton decays mentioned up to this point and identifying two new lines, one tentatively assigned to an isomer in ^{147}Tm [Hof89, Lar83] and the other tentatively assigned to ^{150}Lu [Hof84, Hof89]. However, the identification of any weaker proton decay lines would require a more sensitive technique, including explicit mass identification, and a novel approach to detector design would be needed to assist the assignment of decays to states in parent nuclei.

1.3.2 The Daresbury Experiments

A breakthrough in the search for further examples of proton radioactivity came about with the the development of a purpose-built silicon strip detector system [Sel92a,Sel92b] by the Edinburgh group for use at the focal plane of the Daresbury Recoil Mass Separator. The technique was developed as a highly sensitive method for observing and identifying short-lived, low production cross-section proton emitting nuclei. It heralded the discovery of a large number of new isotopes at and beyond the drip-line, including many ground state proton emitters.

The layout of the Daresbury Recoil Separator is shown in figure 1.3(a). Two Wien filters provided beam rejection and velocity selection, and a dipole section was used to disperse the reaction products according to their mass to charge ratio. Critically, this mass dispersion allowed direct mass assignments of recoil

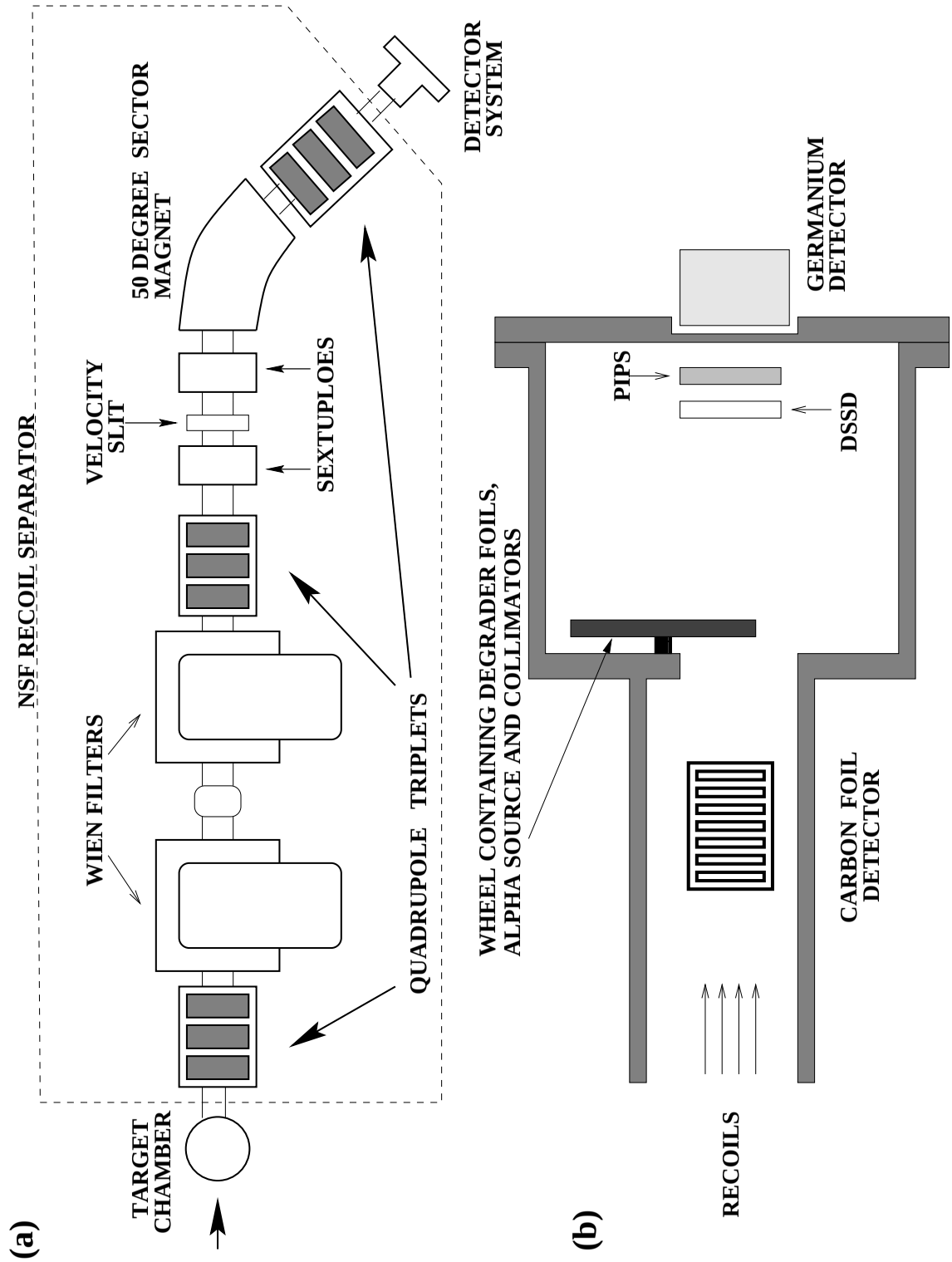

Figure 1.3: (a) The Daresbury Recoil Mass Separator. (b) Detectors used in the Daresbury proton decay experiments.

ions arriving at the focal plane of the separator.

In earlier experiments studying proton rich nuclei [Woo89], evaporation products were dispersed by the mass separator before being implanted into a 2d position sensitive silicon surface barrier detector at the focal plane. Mass identification of implanted ions was made by their horizontal position in the detector. The replacement of the surface barrier detector by a double-sided silicon strip detector (DSSD)[Sel92a,Sel92b], never before used in a nuclear physics experiment, greatly improved the energy and position resolution, the latter increasing correlation efficiencies, making possible the identification of even weaker decay lines. The design and use of the DSSD are more fully described in Chapter 3. The detector set-up for the Daresbury proton decay experiments is shown in figure 1.3(b). Evaporation residues transmitted through the Recoil Separator then passed through a carbon foil detector (used for recoil-decay discrimination) before being implanted into the DSSD. These experiments were sensitive to nuclei with half-lives as short as 1 μs, with sub-microbarn production cross-sections.

The first use of the DSSD [Sel92b] was in the study of the reaction ^{58}Ni + ^{54}Fe $\longrightarrow$ ^{112}Xe in which a 0.81 MeV peak had been previously observed and indirectly assigned [Fae84, Gil87] to ^{109}I on the basis of excitation function measurements and Q-value systematics. The Daresbury experiment provided unambiguous and direct assignment to ^{109}I by providing a correlation between the low energy peak and previous implantation events of mass 109, and between the proton peak and the subsequent known alpha decay of ^{108}Te at 3.32 MeV. A further experiment measured the proton transitions from ^{147}Tm with improved half-life values. Direct mass assignments and improved half-life measurements were also made for the proton lines from ^{150,151}Lu.

A further set of experiments was carried out to search for direct proton decay from ^{160}Re, ^{156}Ta, ^{146}Tm, ^{128}Pm, ^{132}Eu, ^{138}Tb and ^{142}Ho [Woo93]. Proton peaks from the first two of these were very cleanly identified [Pag92, Liv93a, Liv93b]

by implant-decay-decay correlation chains as daughter nuclei of proton emitting nuclei in this region decay by well known alpha transitions. Two low energy lines were observed [Liv93a, Liv93c] in the reaction ^{58}Ni + ^{92}Mo $\longrightarrow$ ^{150}Yb in the A=146 mass region and were assigned to proton emission from ^{146}Tm on the basis of the mass identification and cross-section measurements. The search for protons from the other nuclei mentioned above proved negative [Liv93a, Liv93d]. Finally, experiments in the region above ^{100}Sn yielded the discovery of proton radioactivity from ^{112}Cs [Pag94], identified directly as following a mass 112 implantation event and correlated with two alphas from ^{111}Xe and ^{107}Te, its daughter and grand-daughter nuclei respectively. An improved half-life measurement for ^{113}Cs was also made.

The closure of the Nuclear Structure Facility at Daresbury brought to an end a highly successful series of experiments. However, the basic technique developed in these experiments was to be continued with even greater success in the proton decay experiments at Argonne National Laboratory, the discussion of which form the major part of this work.

Assignments of the proton decays mentioned above to shell-model orbitals in the parent nuclei were made on the basis of comparison of the experimentally measured half-lives to barrier penetration calculations assuming spherical nuclei (see theory chapter). The predicted half-lives were found on the whole to be in reasonably good agreement with the measured values, with the exception of those for ^{109}I and ^{112,113}Cs, which are expected to have a more deformed structure. The new data on proton emission presented in this thesis allows us to refine the current theory of proton decay from spherical and deformed nuclei.

Chapter 2

Theory

For proton decay to be energetically allowed, it must have a positive Q_p-value, defined as the difference between initial and final masses of the system:

$$Q_p = (M_{Z+1} - M_Z - m_p - m_e)c^2 > 0 \tag{2.1}$$

where M_{Z+1} and M_Z are the atomic masses of the parent and daughter nuclei, m_p is the proton mass and m_e is the electron mass. Expressed in terms of binding energies, this condition is simply

$$Q_p = B_Z - B_{Z+1} > 0 \tag{2.2}$$

where the binding energy $B_Z = (Z M_H + N M_n - M_Z)c^2$ is the energy required to break up a nucleus of proton number Z and neutron number N into its constituent nucleons. Conservation of momentum demands that the kinetic energy of the decay be divided between the proton and residual nucleus in inverse proportion to their masses. Therefore the proton and recoil energies are:

$$E_p = \frac{M_Z}{M_Z + m_p} \times Q_p \tag{2.3}$$

$$E_R = \frac{m_p}{M_Z + m_p} \times Q_p \tag{2.4}$$

A theoretical treatment of proton decay requires that a correction be made to the above Q-value to take into account the energy loss of the proton as it passes

through the electron cloud. This screening correction E_{SC} is the difference in the electron binding energies of the parent and daughter atoms [Ras66]. Thus:

$$Q_{p,nuc} = Q_p + E_{SC} = E_p(M_Z + m_p)/M_Z + E_{SC} \tag{2.5}$$

2.1 Spherical Proton Emitters

Various theoretical approaches to proton emission from nuclei have been investigated. Unlike alpha decay, it requires no preformation of a cluster of nucleons within the nucleus, so problems involving absolute decay rates are alleviated. Otherwise proton decay can be treated in an analogous way to alpha decay with the inclusion of a spin-orbit term in the interaction, as the proton has a spin $\sigma = 1/2$ compared to zero for the alpha particle. The simplest theories of proton decay assume nucleons occupy single-particle orbits given in the spherical shell model, described below.

2.1.1 Spherical shell model

The success of the atomic shell model in providing clarification of the complicated details of atomic structure prompted nuclear physicists to adopt a similar approach to attack the problems of nuclear structure. Discontinuities in various physical quantities, such as 2-proton separation energies and nuclear radii, at the 'magic' numbers of nucleons give supporting evidence for the existence of nuclear shells.

In the shell model the motion of each nucleon is considered to be governed by an average potential caused by all the other nucleons, which can be represented initially by a spherically symmetric potential. The Hartree Fock method attempts to determine a self-consistent average potential by considering the sum of the two-body interactions, but a simpler and quite effective method of reproducing observed shell orderings and closures is to use a one-body potential determined

from basic nuclear properties. Solving the time-independent Schrödinger equation

$$\left\{\frac{-\hbar^2}{2m}\nabla^2 + V(r)\right\}\phi_i(\vec{r}) = \epsilon_i\phi_i(\vec{r}) \tag{2.6}$$

for this potential one can calculate the energies of the subshells which the nucleons occupy. The Woods-Saxon potential [Woo54], which reflects the mass distribution within the nucleus, is considered a good approximation to the real nuclear potential with no force experienced for a nucleon close to the centre and a strong attractive force at the nuclear surface. Outside the nuclear surface the potential drops rapidly to zero, reproducing the short range of the nuclear force:

$$V_{WS}(r) = -V_0\left[1 + exp(\frac{r - R_0}{a})\right]^{-1} \tag{2.7}$$

where R_0 is the mean radius of the nucleus and a represents the surface diffuseness. This produces the energy level diagram shown on the left of figure 2.1. The inclusion of a spin-orbit term in the interaction splits the l degeneracies and results in a level sequence shown on the right of figure 2.1. The magic numbers given by each potential are indicated and the inclusion of the spin-orbit term reproduces well the observed shell closures. In this model, each level can contain $2j + 1$ nucleons, where j can take the two values $j = l \pm 1/2$, for $l > 0$.

In principle for a shell model nucleus, the Fermi level can be determined by filling the single-particle orbitals in order of ascending energy. The angular momentum of the outermost proton is given by the l value of the highest filled level.

The spherical shell model description of the nucleus is expected to describe well nuclei near the shell closures and calculations assuming these shell model single-particle levels give results which agree reasonably well with experiment for such nuclei. However, nuclei further away from the closed shells are expected to have high prolate deformations, and the spherical shell model becomes inadequate, as demonstrated by the failure of such calculations for nuclei such as ^{109}I and ^{112,113}Cs which are expected to be moderately deformed (see section 2.6).

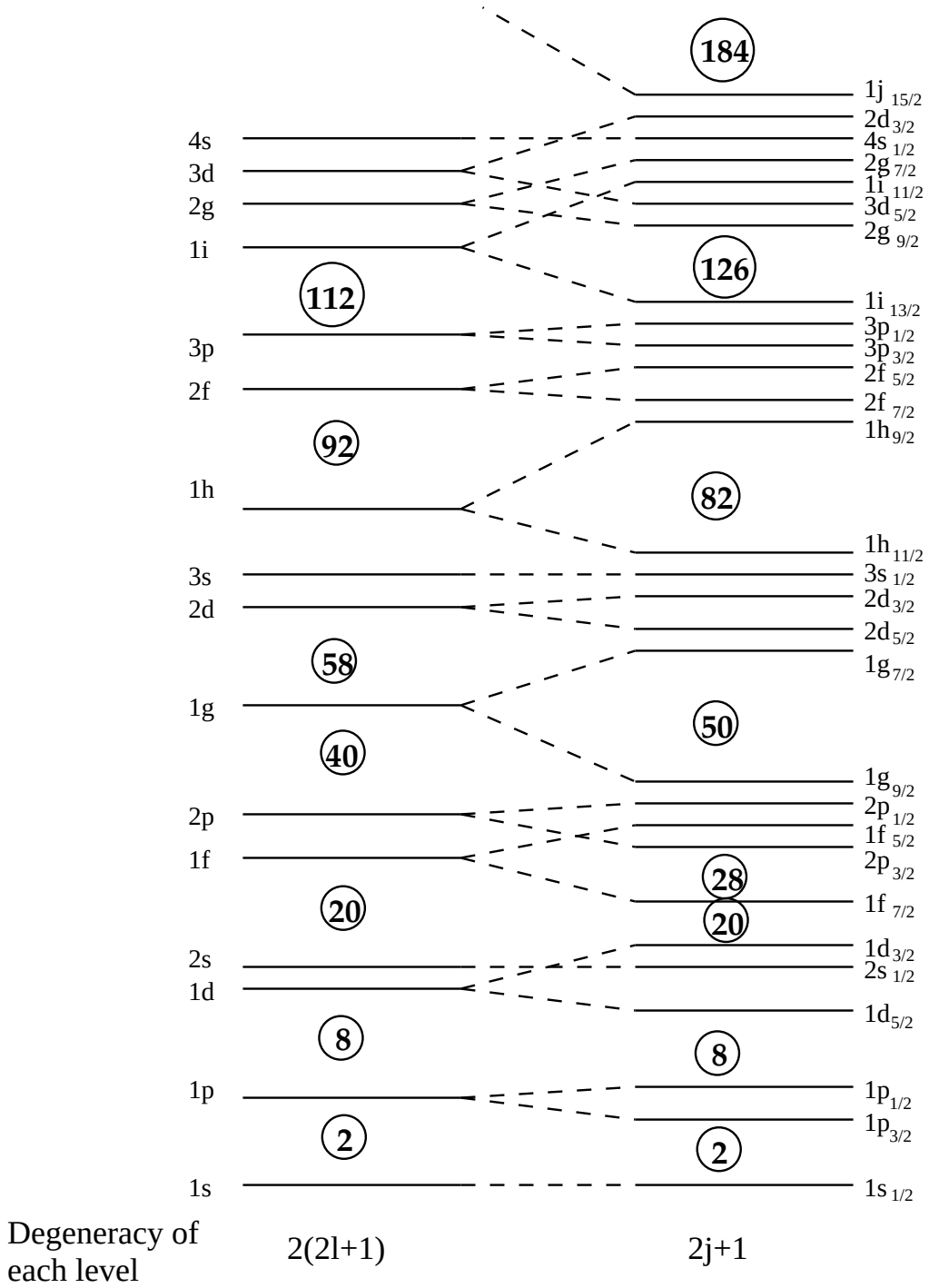

Figure 2.1: Level schemes deuced for a Woods-Saxon type potential (left) and Woods-Saxon plus spin-orbit interaction (right).

2.2 Proton Decay Transition Rates

Proton decay can be treated as a quantum tunneling process. The proton sits in the potential $V(r)$ of the daughter nucleus which is treated as the sum of central nuclear V_{nuc}, spin-orbit V_{SO}, Coulomb V_C and centrifugal V_l terms.

$$V(r) \;=\; V_{nuc}(r) + V_{SO}(r) + V_C(r) + V_l(r) \tag{2.8}$$

The shape of the potential is shown in Fig 2.2. The proton sits in the well at energy $Q_{p,nuc}$ and must tunnel through the barrier subject to the usual conditions

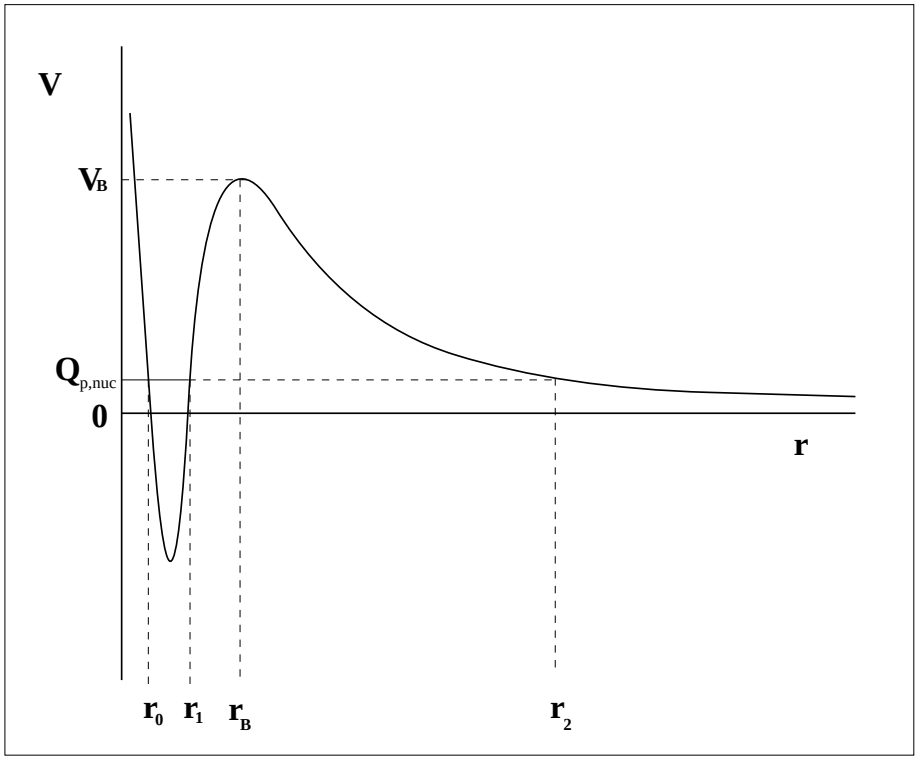

Figure 2.2: Proton-nucleus potential

of conservation of spin and parity.

Early treatments [Gam28,Gur28] of alpha emission in terms of quantum mechanical tunneling through a barrier assigned a semi-classical decay constant

λ ($= ln2/t_{1/2}$) equal to the product of a frequency factor in the potential well ν and a transmission coefficient T:

$$\lambda \ = \ \nu T \tag{2.9}$$

Hofmann [Hof89] used the expression

$$\nu \ = \ \frac{\sqrt{2}\pi^2\hbar^2}{\mu^{3/2}R_c^3(zZe^2/R_C - Q_{p,nuc})^{1/2}} \tag{2.10}$$

μ = reduced mass of the system

$R_C = 1.21$ fm $\times A^{1/3}$

z, Z = charge of proton and daughter nucleus

for the frequency factor in analogy to one obtained by Bethe [Bet37] and Rasmussen [Ras66] for alpha decay rates. The WKB (Wentzel, Kramers, Brillouin) approximation gives the transmission coefficient T as

$$T \ = \ T_{jl} \ = \ e^{-2G_{jl}} \tag{2.11}$$

where the Gamow factor G_{jl} is an integral over the forbidden region of the potential between the classical turning points r_1 and r_2:

$$G_{jl} \ = \ \sqrt{2\mu/\hbar^2}\int_{r_1}^{r_2}(V(r) - Q_{p,nuc})^{1/2}dr \tag{2.12}$$

2.2.1 Sensitivity of the Decay Mode

The transmission probablility T (Eqn 2.11) has an exponential dependence on the integral of the potential over the width of the barrier between the classical turning points, which is strongly dependent on the angular momentum and energy of the proton. Thus the proton partial half-lives are extremely sensitive to l and $Q_{p,nuc}$. Fig 2.3 shows the predicted proton partial half-lives of the proton transitions from the $s_{1/2}$, $d_{3/2}$ and $h_{11/2}$ orbitals in ^{167}Ir to the 0^+ ground state in ^{166}Os as calculated by the method described above.

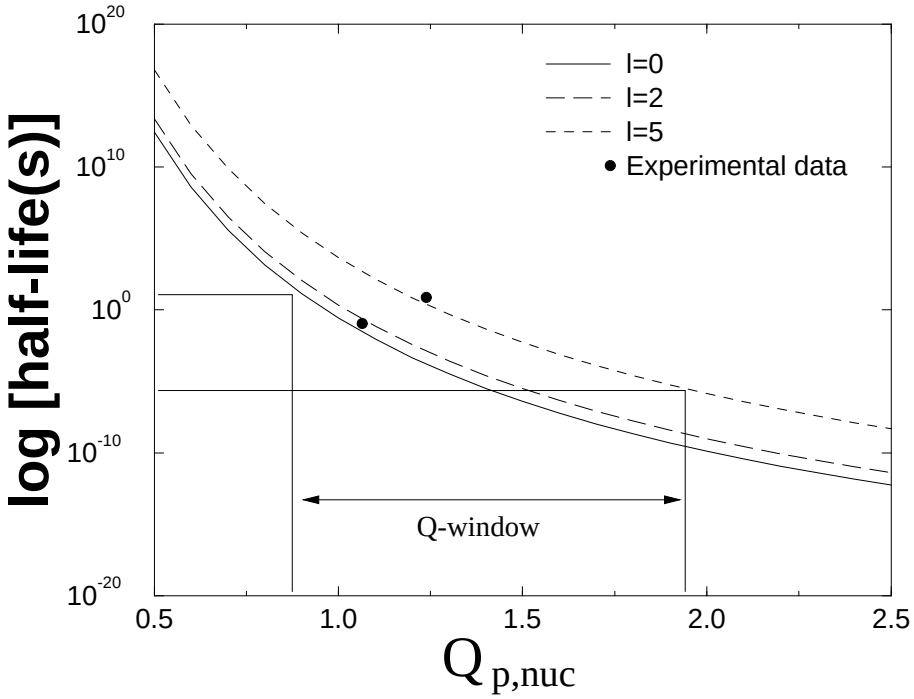

Figure 2.3: Predicted proton partial half-lives for proton decay from the $s_{1/2}$, $d_{3/2}$ and $h_{11/2}$ levels in ^{167}Ir to the 0^+ ground state of ^{166}Os. The Q window represents the range of energies for which protons have an experimentally observable half-life.

The proton partial half-life decreases by more than 24 orders of magnitude for the three cases as $Q_{p,nuc}$ goes from 0.5 MeV to 2.5 MeV. In-flight separation techniques only allow observation of decays with half-lives in the range 1 μs to 1 s and therefore only decays with Q-values within a small energy range, about 0.8-1.8 MeV for a typical rare-earth nucleus as shown in Fig 2.3, are detectable. For lighter nuclei this Q window becomes even narrower (for Z=21, energy window $\sim$ 130-240 keV), and this is one explanation for the non-observation of proton emitters in the light nuclei.

The centrifugal term in the total potential (Eqn 2.6) has an l^2 dependence and its importance is illustrated by the separation of the three curves in fig 2.2.

Q-values can be accurately determined experimentally, so identification of the proton orbital in the parent nucleus can be made by comparison of measured and calculated half-lives. The data for proton emission from ^{167}Ir are plotted in Fig 2.3 and the assignments are discussed in chapter 4.

2.3 Recent Work on Spherical Proton Emitters

The recent explosion in the number of proton emitters discovered has prompted theorists to re-examine the proton decay mechanism. A review of the various theoretical approaches to proton emission from spherical nuclei, which incorporate some of the measurements presented in this thesis, is given in a recent paper by Åberg, Semmes and Nazarewicz [Åbe97]. These approaches are outlined below.

Proton emitters can be considered as extremely narrow scattering resonances which can be interpreted in terms of isolated quasistationary states. A perturbative approach to calculating transition rates, based on standard reaction theory[Sat83], is expected to be very accurate because of the very narrow widths of the resonances. Ground-state proton emission can be considered as one specific reaction channel,

$$ {}^{A+1}_{Z+1}X \longrightarrow {}^{A}_{Z}Y + p \tag{2.13} $$

characterised by a transition amplitude $T_{A+1,Z+1;A,Z}$. The resonance width can be expressed through the transition amplitude as [Fes92, Kad71]

$$ \Gamma = 2\pi |T_{A+1,Z+1;A,Z}|^2 \tag{2.14} $$

where the transition amplitude is given, in the distorted-wave Born approximation (DWBA) for example, by the expression:

$$ T_{A+1,Z+1;A,Z} = < \psi_{Ap} \Psi_{Ap} | V_{Ap} | \Psi_{A+1} > \tag{2.15} $$

where ψ_{Ap} is the incoming spherical wave representing the relative motion of the proton with respect to the daughter nucleus, Ψ_{Ap} is the product of the intrinsic

wavefunctions of the proton and daughter, Ψ_{A+1} is the metastable state of the parent nucleus and V_{Ap} is the interaction between the proton and the daughter nucleus.

Once the decay width is calculated, the half-life of the proton decay can be obtained as

$$t_{1/2,p} = \frac{\hbar}{\Gamma} \times ln2 \tag{2.16}$$

I shall present three different methods used to calculate Γ as described in [Abe97]: the DWBA method, the modified two potential approach of Gurvitz [Gur88] and a quasi-classical approximation.

2.3.1 The DWBA method

The distorted wave Born approximation calculation of the transition amplitude [Eq. (2.15)] requires knowledge of the initial state wavefunction, the final state wavefunctions and the interaction potential V_{Ap}. V_{Ap} is strictly a sum of two body terms describing the interaction between the outgoing proton and each of the A nucleons in the daughter nucleus, but is approximated by a simpler one body potential V which is a sum of a simple optical nuclear potential V_N, and the Coulomb potential V_C.

$$V = V_N + V_C \tag{2.17}$$

The Gell-Mann, Goldberger transformation [Fes92, Sat83] can be used to rewrite Eq. (2.15) as

$$T_{A+1,Z+1;A,Z} = < \Psi_{Ap} \psi^C_{Ap} | V - V^0_C | \Psi_{A+1} > \tag{2.18}$$

where ψ^C_{Ap} is a positive energy eigenstate of the Hamiltonian $T + V^0_C$ where V^0_C $= Ze^2/r$, the point-charge Coulomb potential. The interaction $V - V^0_C$ can be written as the sum of the nuclear optical potential V_N and the correction δV^C to the Coulomb potential due to the finite charge distribution. Therefore

$$T_{A+1,Z+1;A,Z} = < \Psi_{Ap} \psi^C_{Ap} | V_N + \delta V^C | \Psi_{A+1} > \tag{2.19}$$

In this work, the daughter nucleus is treated as an inert core and the wavefunction Ψ_{Ap} can be written as a product of the intrinsic wave functions of the proton (in the ground state) and that of the daughter nucleus, Φ_A. The radial component of ψ^C_{Ap} is

$$\psi_l(r) = \sqrt{\frac{2\mu}{\pi\hbar^2 k}} \times \frac{F_l(r)}{r} \tag{2.20}$$

where $k = \sqrt{2\mu E}/\hbar$, μ is the reduced mass of the system and F_l is the normal Coulomb function. The k-dependent factor in this equation ensures proper renormalisation of the function ψ. The initial state wavefunction, Ψ_{A+1}, describes the proton quasi-bound to the core and can be written as a product of the daughter nucleus wavefunction Ψ_A and the proton wavefunction. The radial wavefunction of the proton in the quasi-bound state,

$$\Phi_{nlj}(r) = \frac{\phi_{nlj}(r)}{r} \tag{2.21}$$

is found by numerically integrating the Schrödinger equation with the potential (2.17). The quasi-bound proton wavefunction $\phi_{nlj}(r)$ is found by smoothly joining the wavefunction from the interior region with the irregular part of the Coulomb wavefunction, $G(r)$, which asymptotically describes the proton wavefunction as $r \longrightarrow \infty$.

Combining (2.19), (2.20) and (2.21), the resonance width becomes

$$\Gamma = \frac{4\mu}{\hbar^2 k} \left| \int_0^\infty F_l(r)[V_N + \delta V^{Coul}]\, \phi_{nlj}(r) dr \right|^2 \tag{2.22}$$

The nuclear interaction between the proton and the core, V_N, is taken to comprise central and spin-orbit components, both of Woods-Saxon type.

2.3.2 The Two Potential Approach

Gurvitz[Gur88] considered the tunneling problem as the decay of a prepared state using a modified two-potential approach. This provides a perturbative method for calculating the decay widths of isolated quasistationary states. The proton moves

in an effective potential $V(r)$, as shown in fig 2.4(a), with an energy E lower than the barrier height. The potential $V(r)$, which includes the centrifugal term, can be split into two parts as shown in figs 2.4(b) and (c):

$$V(r) \;=\; U(r) + W(r) \tag{2.23}$$

where

$$U(r) \;=\; \begin{cases} V(r) & \text{if } r \leq r_B \\ V_B & \text{if } r > r_B \end{cases} \tag{2.24}$$

and

$$W(r) \;=\; \begin{cases} 0 & \text{if } r \leq r_B \\ V_R - V_B & \text{if } r > r_B \end{cases} \tag{2.25}$$

Initially , one can consider the proton in a bound eigenstate Φ_0 of the Hamiltonian $H_0 = -\hbar^2(\nabla^2/2\mu) + U(r)$ with an energy $E_0 < V_B$. The perturbing potential $W(r)$, transforms the stationary state into a quasistationary one, an eigenstate of the full Hamiltonian $H = H_0 + W(r)$ with energy E. In general, $E \neq E_0$. An expression for Γ can be obtained by solving the coupled equations provided by standard time-dependent perturbation theory. First however, one must introduce a 'shifted' potential $\tilde{W} = W(r) + V_B$ as shown in fig 2.4(d), in order to satisfy the condition that the perturbing potential vanishes as $r \to \infty$.

From this one can obtain a simple expression for the decay width

$$\Gamma \;=\; \frac{4\mu}{\hbar^2 k} \left| \int_{r_B}^{\infty} \phi_{nlj}(r) W(r) \chi_l(r) dr \right|^2 \tag{2.26}$$

where $k = \sqrt{2\mu E}/\hbar$, ϕ_{nlj} is the radial wavefunction of Φ_0 and $\chi_l(r)$ is the regular radial wavefunction of the Hamiltonian $T + \tilde{W}$, with the asymptotic behaviour

$$\chi_l(0) = 0 \;\text{ and }\; \chi_l(r) \to sin(kr - \pi l/2 + \delta_l) \;\text{ for }\; r \to \infty \tag{2.27}$$

For $r \;>\; r_B$ the radial wavefunction $\phi_{nlj}(r)$ is

$$\phi_{nlj}(r) \;=\; \phi_{nlj}(r_B) \exp[-\alpha(r - r_B)], \tag{2.28}$$

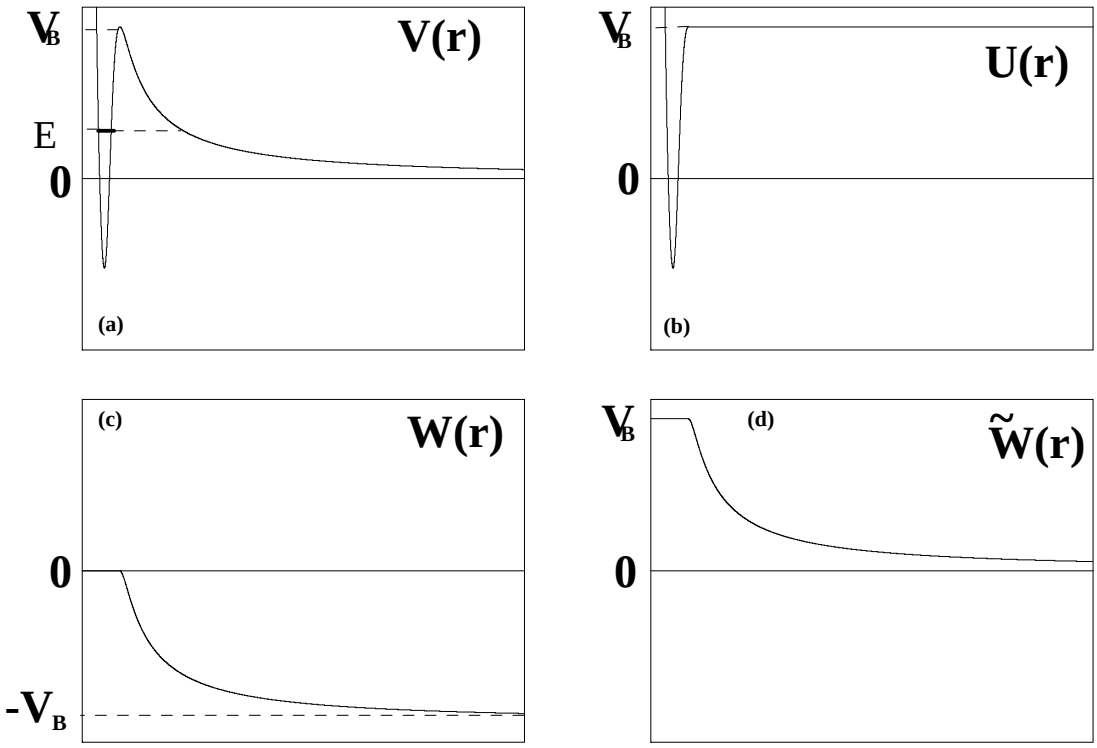

Figure 2.4: The two potential approach.(a) The proton-nucleus potential V(r). (b)+(c) The potential can be split into two parts U(r) and W(r) such that V(r)=U(r)+W(r). (d) The shifted potential $\tilde{W}(r)$

and therefore the integral in (2.26) can be carried out analytically, giving

$$\Gamma \;=\; \frac{\hbar^2}{\mu k}|\phi_{nlj}(r_B)[\alpha\chi_l(r_B) \;+\; \chi_l'(r_B)]|^2 \tag{2.29}$$

where $\alpha \;=\; \sqrt{2\mu(V_B - E_0)}/\hbar$ and $\chi_l'(r) \;=\; d/dr(\chi_l(r))$. Note the final result depends only on the value of the wavefunctions at r_B although the contribution to the integral in eqn (2.26) comes entirely from the region $r > r_B$. However, the result depends only very weakly the particular choice of r_B as variation of this parameter increases the penetration in the classically forbidden region for one of the wavefunctions, but simultaneously decreases the penetration for the second one, so that the result Γ tends to stay the same.

In the approach of Aberg, Semmes and Nazarevich [Abe97] the scattering wave function χ_l is given by

$$\chi_l(r) \;=\; \chi_l(r_B)\frac{\sinh(\alpha r)}{\sinh(\alpha r_B)} \;\text{ if } r < r_B \tag{2.30}$$

$$\chi_l(r) \;=\; \cos\delta_l F_l(kr) - \sin\delta_l G_l(kr) \;\text{ if } r > r_{big}, \tag{2.31}$$

where F_l and G_l are the regular and irregular Coulomb wavefunctions, respectively, and r_{big} is the cut-off radius beyond which the contribution from the nuclear potential is unimportant. This condition is fulfilled for $r_{big} \;>\; 1.5r_B$. In the intermediate region between r_b and r_{big} the scattering wavefunction is obtained by direct integration of the Schrödinger equation. The relative phase δ_l is calculated by matching logarithmic derivatives at $r = r_{big}$.

By neglecting the nuclear contribution to the scattering state for $r > R_B$, a simple approximation can be made to eqn 2.29, giving the phase shift as

$$\tan\delta_l \;=\; \frac{kF_l'(kr_B) - \alpha\coth(\alpha r_B)F_l(kr_B)}{kG_l'(kr_B) - \alpha\coth(\alpha r_B)G_l(kr_B)} \tag{2.32}$$

2.3.3 Quasi-classical Approximation

In the quasi-classical limit, the expression for Γ in the two potential approach above becomes [Gur88]

$$\Gamma \;=\; N\frac{\hbar^2}{4\mu}\exp\{-2\int_{r_1}^{r_2}|k(r)|dr\} \tag{2.33}$$

where $\hbar k(r) \;=\; \sqrt{2\mu[E-V(r)]}$ is the classical momentum, $r_{1,2}$ are the classical turning points indicated in fig 2.2 and $E \;=\; Q_{p,nuc}$. The normalisation factor N is usually evaluated considering only the classically allowed region,

$$N^{-1} \;=\; \int_{r_0}^{r_1}\frac{dr}{k(r)}\cos^2[\int_{r_0}^{r}k(r')dr' - \frac{\pi}{4}] \tag{2.34}$$

although in principle, the contribution from the forbidden region, if not small, should also be considered.

2.3.4 Model Parameters

For the proton-nuclear potential, it is normal to use a Woods-Saxon field, consisting of central and spin-orbit terms.

$$V_N(r) \;=\; -V^0_{Nuc}\,f(r,R_{Nuc},a_{nuc}) \;+\; V^0_{so}\sigma.l\lambda^2_\pi(1/r)(d/dr)f(r,R_{so},a_{so}) \tag{2.35}$$

where

$$f(r,R_{Nuc,so},a_{nuc,so}) \;=\; [1+\exp\{\frac{r-R_{Nuc,so}}{a_{Nuc,so}}\}]^{-1} \tag{2.36}$$

$$\sigma.l \;=\; \begin{cases} l & \text{for } j=l+1/2 \\ -(l+1) & \text{for } j=l-1/2\,(l>0) \end{cases} \tag{2.37}$$

$$\lambda_\pi \;=\; \sqrt{2}\text{fm (pion Compton wavelength)} \tag{2.38}$$

with the WS form factor defined by the radius $R_{Nuc} = R_0A^{1/3}$, and diffuseness a. The effect on calculated half-lives of varying these two parameters within the range of their uncertainties has been shown to be small [Abe97, Hof96] and the results

quoted in the following sections were calculated using the values of Becchetti and Greenlees [Bec69]: $R_{Nuc} = 1.17$, $a_{Nuc} = 0.75$, $R_{so} = 1.01$, $a_{so} = 0.75$. For the depth of the central nuclear potential, Hofmann used the Becchetti-Greenlees expressions

$$V^0_{Nuc} = 54.0 - 0.32\,Q_{p,nuc} + 0.4\,Z/A^{1/3} + 24.0(N-Z)/A \quad (2.39)$$

$$V^0_{so} = 6.2 \quad (2.40)$$

but in the calculations of Aberg et al, V^0_{Nuc} was adjusted to reproduce the energies of quasistationary states and V^0_{so} was taken as $-0.2\,V^0_{Nuc}$. In all the results presented, the Coulomb potential assumes uniform charge distribution within the nucleus and is given by

$$V_C(r) = \begin{cases} (\frac{Ze^2}{4\pi\epsilon_0 R_C}) \times (3 - \frac{r^2}{R_c^2}) & \text{for } r \le R_C \\ \frac{Ze^2}{4\pi\epsilon_0 r} & \text{for } r > R_C \end{cases} \quad (2.41)$$

$$(2.42)$$

where $R_C = 1.21\ A^{1/3}$ fm. The quasi-classical and TPA theories use a centrifugal term strongly dependent on the angular momentum l of the proton:

$$V_l(r) = \frac{l(l+1)\hbar^2}{2\mu r^2} \quad (2.43)$$

2.4 Spectroscopic factors

So far this work has treated proton emitting nuclei in the ideal case as inert cores with a proton occupying a single particle level with a well defined angular momentum l. The WKB calculations neglect nuclear structure effects, apart from a change in angular momentum. The theoretical calculations of the proton partial half-lives presented earlier in this chapter ignored nuclear structure effects. For spherical nuclei this is sufficient for assignments of decays to particular orbitals, but a more complete description of proton decay should include effects due to the

incomplete overlap of parent and daughter wavefunctions, which are described by the use of the spectroscopic factor S_j.

The experimental spectroscopic factor can be defined as the ratio of calculated and measured half-lives,

$$S_p^{exp} = t_{1/2}^{th}/t_{1/2}^{exp} \tag{2.44}$$

The theoretical spectroscopic factor is a measure of the probability that, in the initial nuclear state, all but one of the nucleons will find themselves in an arrangement corresponding to the final state. It is defined as [Boh69]

$$S_p^{th} = \frac{1}{2I_i+1}| < I_i||a_{nlj}^{\dagger}||I_f > |^2 \tag{2.45}$$

in analogy to a proton pick-up reaction. A proton with angular momentum j is removed from the parent nucleus with angular momentum I_i leaving the daughter nucleus in the state $I = I_f$. $a_{nlj}^{\dagger}$ is a creation operator [Boh69]. The overlap of the states might not be complete if, for example, the parent state of an odd-A proton emitter consists of a hole in a particular orbital, while the daughter state has this orbital completely filled. The effect of an incomplete overlap of parent and daughter wavefunctions is hindrance of any decay, hence an increase in the decay half-life.

Following the discovery of several new proton emitters at Argonne, a low-seniority shell model calculation of the wavefunctions for the parent and daughter states has been carried out [Dav97a] in order to quantify the above approach for proton emitters in the region $65 \leq Z \leq 82$. The model space consisted of 18 particles in the $s_{1/2}$, $d_{3/2}$ and $h_{11/2}$ proton orbitals above the Z=64 sub-shell closure, with neutrons assumed to be spectators only, i.e., the neutron configuration does not change during the decay. The residual interaction used was a pairing force and the single particle energies for the three orbitals were assumed to be degenerate.

The two-body pairing Hamiltonian has the form

$$H = \sum_j \epsilon_j n_j + G \sum_{j,j'} (-1)^{l+l'} [(j+1/2)(j'+1/2)] \times A^{0\dagger}(j^2) A^0(j'^2)$$

where ϵ_j and n_j are the single-particle energy and number of particles in orbital j, G is the strength of the pairing interaction and $A^{0\dagger}(j^2)(A^0(j'^2))$ is the creation (annihilation) operator for a pair of protons in orbital j coupled to spin 0.The assumption of degenerate levels ($\epsilon_j = \epsilon$) allows the use of the quasispin lowering and raising operators:

$$S^+ = \sum_j (-1)^l (j+1/2)^l A^{0\dagger}(j^2)$$

$$S^- = \sum_{j'} (-1)^{l'} (j'+1/2)^l A^{0\dagger}(j'^2)$$

so we obtain the quasispin Hamiltonian

$$H = N\epsilon + GS^+S^-$$

Quasispin operators obey the usual commutation relations for angular momentum operators, and we have

$$[S^+, S^-] = 2S_0 = N - \sum_j \frac{2j+1}{2} = N - \Omega$$

where Ω is the total number of pair states and $N = \sum_j n_j$. In the case of even Z, the lowest seniority(J=0) eigenfunction of the quasispin operator is

$$\phi^{S=\Omega/2}_{S_z=1/2(N-\Omega)}$$

and for odd Z, the lowest seniority(J=j) eigenfunction is

$$\phi^{S=(\Omega-1)/2}_{S_z=1/2(N-\Omega)}$$

We have a total of 18 protons in the $s_{1/2}$, $d_{3/2}$ and $h_{11/2}$, so Ω=9. If p is the number of proton hole pairs counting down from Z=82, the even-Z daughter nuclei have N=18-2p, and the odd-Z proton emitters have N=10-2p, with $1 \leq p \leq 9$. The

spectroscopic factor, defined as the overlap between parent and daughter states is given by

$$S_j(p) = |\langle \phi^4_{5-p}(J=j)|a^{1/2\dagger}_{1/2}(j)|\phi^{9/2}_{9/2-p}J=0\rangle|^2$$

which can be reduced to

$$S_j(p) = \left(\frac{9}{2}\frac{1}{2}\frac{9}{2} - p\frac{2}{2}\right)^2 |\langle \phi^4||a^{1/2\dagger}||\phi^{9/2}\rangle|^2$$

where the p dependence is now contained in the Clebsch-Gordan coefficient. The reduced matrix element can be evaluated for the case of p=9, where $S_j(9) = 1$, yielding the final simple result:

$$S_j(p) = \frac{p}{9}$$

A more sophisticated approach is presented in [Åbe97] using the independent-quasiparticle approximation (BCS theory) in which the spectroscopic factor is given by

$$S^{th}_p = u^2_j$$

where u^2_j is the probability that the spherical orbital (nlj) is empty in the daughter nucleus. This assumes the nuclear core does not change during the decay process, ie. all other nucleons behave as spectators. The authors used a proton pairing strength of

$$G_p = \frac{1}{A}[17.9 + 0.176(N-Z)]$$

and the pairing-active space consisting of the lowest Z degenerate single-particle proton levels to calculate theoretical spectroscopic factors.

A comparison of experimental spectroscopic factors with those using the two approaches above is made in chapter 5.

2.5 Deformed nuclei

Nuclei away from closed shells can exhibit large quadrupole moments, and the use of a self-consistent spherical potential to calculate the energies and properties of

states is no longer feasible. Nilsson [Nil55] used a shell model potential approximating the deformed nuclear shape, i.e. spheroidal. The energy of the states are given by the eigenvalues of the Hamiltonian H

$$H = H_0 + H_\delta + C\vec{l}.\vec{s} + D\vec{l}^2 \quad (2.46)$$

$$H_0 + H_\delta = -\frac{\hbar^2}{2m}\nabla^2 + \frac{1}{2}m\omega_0^2 r^2 - \frac{4}{3}\sqrt{\frac{\pi}{5}}\delta m\omega_0^2 r^2 Y_{20} \quad (2.47)$$

and depend on the nuclear deformation, characterised by the quadrupole deformation parameter β_2. The resulting wavefunctions are quantised along the symmetry axis and described by quantum numbers N, the principal quantum number, l, the orbital angular momentum, and $\Lambda\Sigma$, the projections onto the symmetry axis of l and σ respectively. The component of the total angular momentum along the symmetry axis of the core is denoted by Ω. The degeneracies of the zero deformation shell model states are split into $j + 1/2$ sub-shells, each two-fold degenerate, and characterised by $|\Omega|$.

Fig 2.5 shows the proton one-particle levels for nuclei with $50 \leq \mathrm{Z} \leq 82$, calculated as described by by Bengtsson and Ragnarsson [Ben85], as a function of the deformation parameter ϵ_2, which can be defined in terms of $\delta = \Delta\mathrm{R}/\mathrm{R}_{rms}$, where R_{rms} is the root mean square nuclear radius and ΔR is the difference between the semi-major and semi-minor axes of the nuclear ellipsoid, as

$$\epsilon_2 = \delta + \frac{1}{6}\delta^2 + \frac{5}{18}\delta^3 + \frac{37}{216}\delta^4 + \ldots$$

The deformation parameter β_2 is related to ϵ_2 by

$$\beta_2 = \sqrt{\pi/5}\left[\frac{4}{3}\epsilon_2 + \frac{4}{9}\epsilon_2^2 + \frac{4}{27}\epsilon_2^3 + \ldots\right]$$

In figure 2.5 the single particle energies are plotted in units of the oscillator frequency

$\hbar\omega = 41\ \mathrm{A}^{-1/3}$ MeV and the effects of a hexadecapole deformation $\epsilon_4 = \epsilon_2^2/6$ are taken into account.

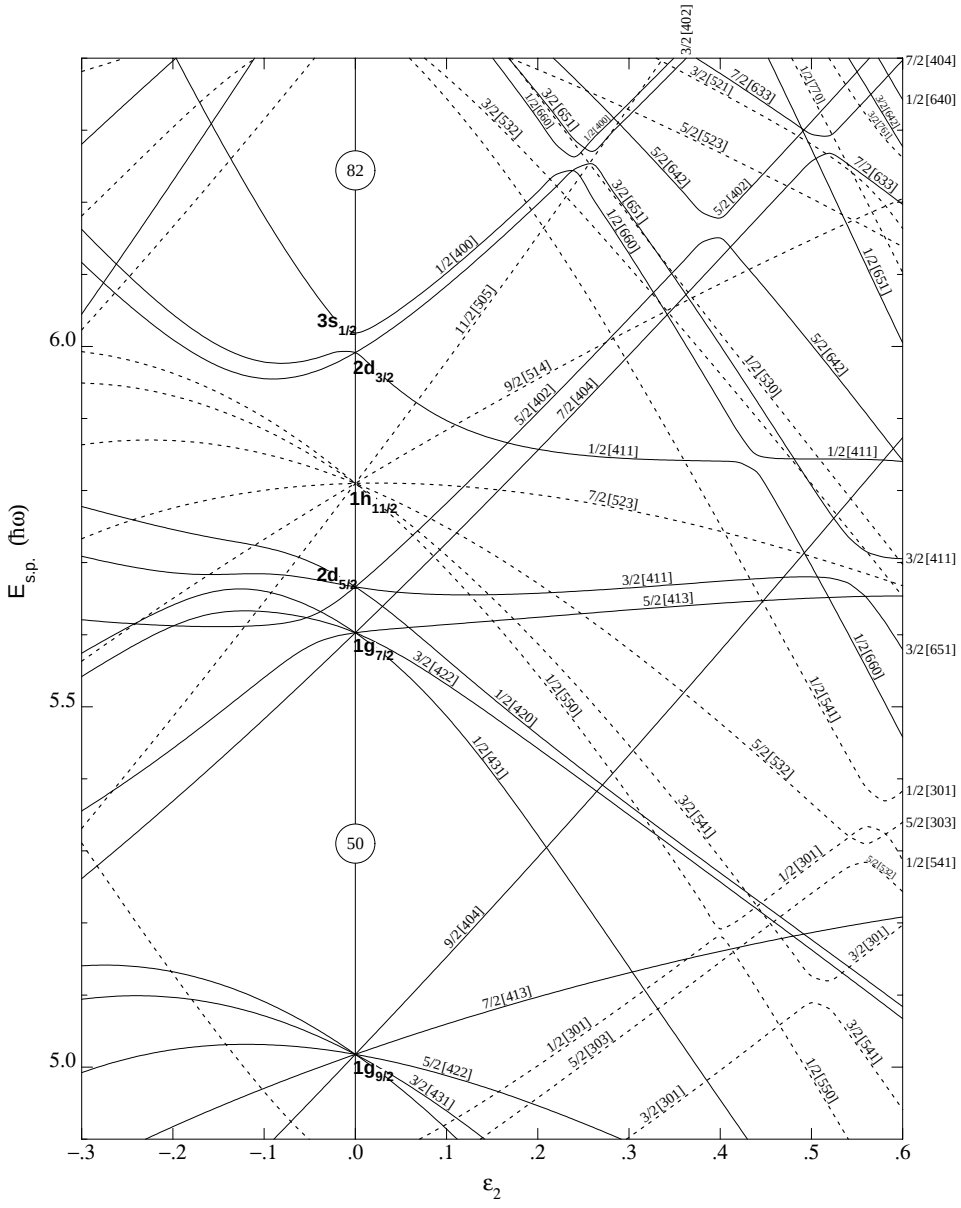

Figure 2.5: Nilsson diagram for protons, $50 \leq Z \leq 82$.

In a similar way to the spherical shell model, the levels can be filled up in order of increasing energy to determine the orbital angular momentum of the fermi level protons. By minimising the total energy of the summed single particle energies with respect to the deformation, one can calculate the ground-state deformation.

2.5.1 Theory of proton emission from deformed nuclei

Bugrov *et al.* [Bug85a,Bug85b] developed a multiparticle theory of proton radioactivity to calculate proton decay probabilities for a wide range of nuclei. Bugrov and Kadmensky [Bug89,Bog90] later included deformation effects in these calculations in order to account for the anomalous decay rates of ^{109}I and ^{113}Cs, and then to assign Nilsson proton shell configurations to known proton decays from ^{147}Tm, ^{147m}Tm, ^{150}Lu and ^{151}Lu [Kad96].

Their model can be shown to be equivalent to the DWBA method (section 2.3.1) adapted to deformed nuclei, and treats the axially-symmetric deformed odd-A nucleus as an inert core plus an odd proton in a quasi-bound state. The wavefunction of the odd proton in the body-centred coordinate system of the nucleus can be expressed as a sum of spherical components having constant l,j and projection Ω:

$$\psi(N\Omega) = \sum_{jl} c_{jl}(N\Omega)|Nlj\Omega >,$$

where n denotes the number of oscillator quanta. Only the parity and Ω are good quantum numbers. The coefficients $c_{jl}(N\Omega)$ determine the probability that the proton has a given j and l. The proton decay amplitude B is given as [Bug89]

$$B = \left[\frac{2(2J_f+1)}{2J_i+1}\right]^{1/2} \langle J_f j_p 0 K_i | J_i K_i\rangle U_f(K_i) \sum_{lj,m_s} c_{jl}(NK_i)\langle l_p \frac{1}{2} K_i - m_s m_s | j_p K_i\rangle$$

$$\times\langle l\frac{1}{2}K_i - m_s m_s | jK_i\rangle \left\langle Y_{lp}^{K_i-m_s}(\theta',\phi')\frac{F_{l_p}(kr,\nu)}{r}|V_{pA}(r) + V_{Coul}^{nonspher}(r)|\frac{R_{nlj}(r)}{r}Y_l^{K_i-m_s}(\theta',\phi')\right\rangle$$

Here J_i and K_i are the total angular momentum and its projection onto the symmetry axis for the deformed parent nucleus, J_f is the angular momentum of the

daughter nucleus, $U_f(K_i)$ is the probability amplitude that the K_i orbital in the daughter nucleus is not occupied $F_l(kr, \nu)$ is the regular Coulomb function and $R_{nlj}(r)$ is the radial part of the proton quasi-bound state wavefunction. In the multiparticle calculations presented in this work, the potential $V_{pA}(r)$ consists of the real part of the deformed optical potential between the proton and the daughter nucleus, and includes the spin-orbit term. The nuclear surface is described by the expression

$$R(\theta') = R_0 A^{1/3} c(\beta)[1 + \beta_2 Y_{20}(\theta')].$$

where the function $c(\beta)$ ensures the nuclear volume is kept constant. The deformed optical potential form-factor is of the form

$$f(r, \beta, a_i) = \{1 + exp[\Delta(r, \beta)/a_i]\}^{-1}$$

where $\Delta(r, \beta)$ is the shortest distance form the point $\mathbf{r}$ to the nuclear surface, and the a_i are the various diffuseness parameters. The nonspherical Coulomb potential $V_{Coul}^{nonspher}(\mathbf{r})$ is comprised of quadrupole and hexadecapole components. The effect of having $Y_{20}(\theta')$ terms in the deformed nuclear potential is to permit angular momentum exchange between the outgoing proton and the core during the decay. Thus the decay amplitude contains the diagonal matrix element $\langle l_p j_p | V | l_j \rangle$ with $l = l_p$ and $j = j_p$, as well as non-diagonal matrix elements having other l-values of the same parity as l_p and $j = l \pm 1/2$ with $N + 1/2 \geq j \geq K_i$.

The radial part of the spherical wavefunction $R_{nlj}(r)$ was obtained by numerically integrating the Schrödinger equation using the Störmer method [Hen62]. In this case the spherical Becchetti-Greenlees potential was used, with the Coulomb potential inside the nucleus calculated with a uniform charge density. Using experimentally obtained proton Q-values as energy eigenvalues, the logarithmic derivatives of inward and outward integrations were matched at a point inside the nucleus by adjusting together the real and spin-orbit well depths.

The $c_{jl}(NK_i)$ spherical expansion coefficients were obtained using the eigen-

value procedure described by Anderson, Back and Bang [And70], giving the advantage of allowing the same potential to be used for the calculation of both the spherical expansion coefficients and the spherical wavefunctions. The $c_{jl}(NK_i)$ coefficients obtained in this way are similar to those obtained using a deformed harmonic oscillator potential.

The results of the above calculation for proton emission from ^{141}Ho are presented and discussed in chapter 5.

2.6 Mass models

Predictions of proton decay Q-values for nuclei far from stability are made using mass models which incorporate various nuclear structure effects beyond the scope of present shell model calculations. The two commonly used models outlined below both include a deformation dependent shape term, an odd-even staggering term and shell corrections but differ in the number of adjustable parameters and the goodness-of-fit to the experimentally determined mass surface. All models use adjustable parameters to fit the data to the known masses and generally models with a larger number of these give a better fit to the known data, although not necessarily beyond it. Recent models also tend to incorporate the latest experimental results on proton decay into their database, making it difficult to assess their predictive powers relative to earlier models. The following sections describe and compare two commonly used nuclear mass models.

2.6.1 Möller-Nix mass model

Möller *et al.* [Möl81, Möl88, Möl95] have used a macroscopic-microscopic model to predict ground-state masses from ^{16}O to ^{318}122. The most recent of these uses the finite range droplet model, which is an improved version of the original droplet model [Mye77]. The total ground state energy of a nucleus is given as a sum of

a semi-empirical term describing general trends over a wide range of N and Z, and a 'microscopic' correction term due to the non-uniform distribution of single particle levels in the nucleus.

$$E(Z, N, shape) \; = \; E_{macro}(Z, N, shape) \; + \; E_{micro}(Z, N, shape) \qquad (2.48)$$

The macroscopic energy is given by a sum of volume and surface energy terms with additional corrections to account for Coulomb energy, charge asymmetry, the proton form factor, Wigner energy, pairing energy and the energy of the bound electrons.

The microscopic term is given in terms of a shell-correction term and a pairing term, both evaluated from a set of Nilsson single-particle levels deduced from solving the Schrödinger equation for a deformed nucleus. The shell-correction term is then calculated using Strutinsky's method [Str67, Str68] and the pairing term using the Lipkin-Nogami [Pra73] version of BCS theory.

The ground state masses are calculated by minimising the total energy with respect to deformation parameters. Proton separation energies can be calculated simply from the ground state masses. The model also provides predictions of ground-state deformations, which is of particular interest since deformation is thought to be the cause of anomalous decay rates in lighter proton emitters. Figure 2.6 shows the quadrupole deformation predicted by the macroscopic-microscopic model. The black squares represent the stable nuclides and the black line is the predicted position of the proton drip-line.

2.6.2 Liran-Zeldes model

Liran and Zeldes [Lir76] calculated the masses excesses of 5563 nuclei using a semi-empirical shell model mass equation based on a strong pairing interaction complicated by excitations within sub-shells and shells due to deformation and core polarisation. The nuclear part of the ground state energy of the nucleus is

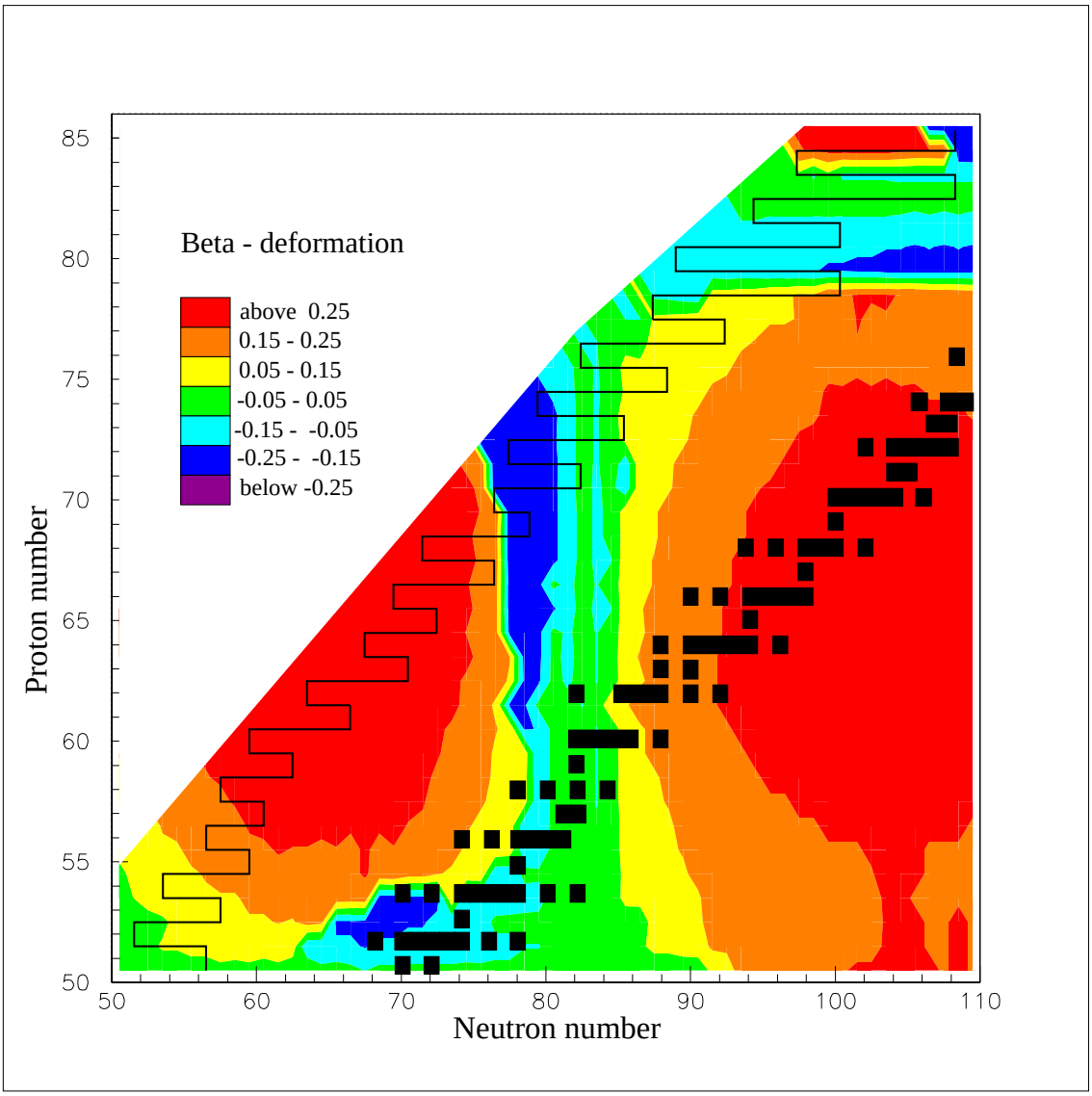

Figure 2.6: Plot of beta deformation parameter β_2 versus proton and neutron number as calculated from the mass model of Möller *et al.* [Möl95]. Black squares represent stable nuclei and the expected position of the proton drip-line is indicated by the black line.

written as the sum of a pairing energy E_{pair}, a deformation energy E_{def} due to a configuration interaction and the Coulomb energy E_{Coul}.

$$E(N,Z) \;=\; E_{pair}(N,Z) \;+\; E_{def}(N,Z) \;+\; E_{Coul}(N,Z) \tag{2.49}$$

Shell regions with valence protons and neutron filling the same major shell are treated differently from those in non-diagonal regions, where they fill different shells.

The 178 independent coefficients of the mass equation were determined in each shell region separately, by least squares adjustment to the experimental data, with the requirement that the mass surface be continuous at the boundaries.

2.6.3 Comparisons between models

Table 2.1 compares some aspects of the two mass models. The macroscopic-microscopic model of Möller *et al.* uses far fewer parameters, and indeed only five of these are adjusted to fit the experimental masses, the rest being taken from previous work. Both models use an extensive database of experimentally

Model	Number of parameters	Number of database nuclei	Number of predicted nuclei	RMS deviation (keV)
Möller *et al.*	26	1593	4635	849
Liran and Zeldes	178	1818	5563	197-276

Table 2.1: Comparison of the mass models

determined masses for parameter adjustment and, as expected, the Liran-Zeldes model, with its far greater number of parameters, produces predictions with a smaller root mean square deviation from the measured values. However, beyond the range of known masses, models with fewer parameters are expected to give better predictions.

The predictions of proton separation energies, along with considerations such as access to the drip-line and fission competition at higher masses, form the basis of the search for new proton radioactivities.

Chapter 3

Experimental Technique

3.1 Introduction

Any technique used in the search for examples of proton radioactivity must be able to overcome the many problems [see chapter 1] associated with the production, detection and identification of such exotic species. The technique used in these experiments is based on the method used for the proton decay experiments which took place at the Daresbury Recoil Separator in the early 1990s, a description of which can be found in [Sel92]. A schematic layout of the current experiments is shown in Fig 3.1. The separate components of the detection system are described

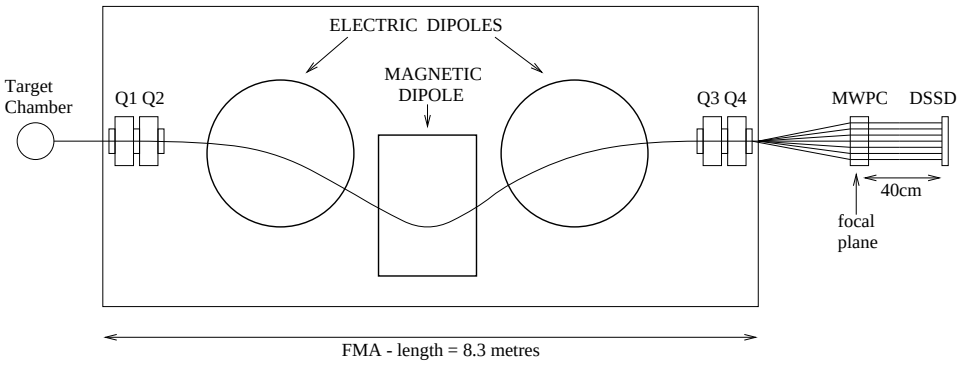

Figure 3.1: Schematic layout of experiment

more fully in the following sections. This section briefly explains how the detection system works as a whole.

A heavy ion beam from the ATLAS accelerator at Argonne National Laboratory hits a thin ($\sim$1 mg/cm^2) target. Fusion evaporation residues pass through the Fragment Mass Analyser (FMA), where they are separated from the primary beam then dispersed horizontally according to their mass to charge state ratio (A/Q). A thin multi-wire proportional counter (MWPC) at the focal plane of the FMA provides position and energy loss signals for the recoil ions, which are then defocused to approximately uniformly illuminate the surface of a double-sided silicon strip detector (DSSD). The DSSD, which is described in sections 3.4.2 and 3.4.3, has 48 strips on each face, orthogonally crossed, providing 2304 'quasi-pixels' and is effectively transparent to β radiation. Once implanted into the strip detector, the ions undergo a series of decays until they reach stability. Both implantation and decay events are recorded by the DSSD and identified by DSSD-MWPC coincidences and anti-coincidences respectively. Explicit mass identification of an implanted ion is obtained from its horizontal position as it passes through the MWPC. The high degree of granularity in the strip detector ensures that firm correlations between implanted ions and their subsequent decays can be made. Decay-decay correlations can also be made, and often a decay chain can be mapped out for several generations. Thus, a previously unseen decay can be correlated to both the preceding implanted ion of known mass and a subsequent known alpha decay, and so can be unambiguously assigned to a specific nuclide. Background can be almost entirely eliminated, allowing assignments for even very weak decay lines.

The higher energy acceptance of the FMA compared to the Daresbury Recoil Mass Separator and its transmission of up to three charge states of the central mass (compared to 1 at Daresbury) result in a higher transmission efficiency of the evaporation residues (typically 15% compared to 3% for the RMS), increasing

the sensitivity of the experiments to nuclei with smaller cross-sections.

The major difference from the Daresbury experiments is the positioning of a MWPC rather than the DSSD at the focal plane of the mass separator. In these experiments the silicon detector was placed 40 cm downstream of the focal plane to ensure reasonably uniform illumination of the detector over almost its entire area. This diffusion of the recoils over the whole area rather than the focusing of them on particular parts of the detector results in lower local implantation rates in these regions, improving the correlation efficiency which further reduces background and allows us to search for decays with longer half-lives. Radiation damage to these regions is also reduced, extending the useful lifetime of the detector.

The high degree of segmentation in the detector (48 strips on each face) requires the use of a large number of preamplifiers and amplifiers to handle the signal processing. The use of high density detector instrumentation specifically designed for the DSSD is described in section 3.5.2.

Later experiments incorporated an array of gamma ray detectors around the target position in addition to the experimental set-up described above. This method of recoil decay tagging (RDT) [Pau95] allows gamma-ray spectroscopy on nuclei much further from stability than previously possible. Nuclei are identified by their particle (alpha or proton) decays in the silicon detector and gamma rays associated with the correlating recoils are studied.

3.2 Beam and Target Choice

The heavy ion beams used in these experiments were provided by ATLAS (the Argonne Tandem Linear Accelerator System) at Argonne National Laboratory, Illinois, USA. This was the world's first superconducting linear accelerator for particles heavier than the electron and uses either a 9 MV tandem Van de Graff or a 12 MV electron cyclotron resonance (ECR) ion source to inject the beam into

two linear accelerators providing beams of elements from hydrogen to uranium at energies of up to 17 MeV per nucleon. The reliability and versatility of the beams from ATLAS, and in particular the high energies available compared to the tandem accelerator at Daresbury, contributed much to the success of the experiments. The ECR source also allows acceleration of noble gases such as krypton, which could not be produced as a negative ion at Daresbury Laboratory.

In these experiments the proton drip-line was accessed using fusion-evaporation reactions. Careful choice of beam and target species was needed to produce a compound nucleus as close to the proton drip-line as possible. An initial choice of beam energy was made after consideration of the optimum compound nucleus excitation energy for the desired evaporation channel. The beam energy was occasionally 'tweaked' if observation of the implantation rates of various nuclei in the DSSD suggested the beam energy was not optimised for the fusion-evaporation channel. A choice of target thickness was made taking into account that a thicker target produces a higher yield of evaporation products, but that too thick a target results in multiple scattering and gives recoils with an energy spread larger than the acceptance of the FMA, therefore reducing overall efficiency. Actual target thickness used also depended on availability and the properties of the target material and was typically about 1mg/cm^2. The beam energy was chosen to produce the desired compound nucleus excitation energy at the centre of the target so that a range of energies around the theoretical optimum could be covered.

Targets were mounted on a ladder which could be lowered or raised to change target type. In later experiments, we had the option to rotate the target, so an off-centre beam spot would trace a circular path on the target, dispersing the deposited energy over a larger area and so minimising damage to the target.

A thin (20μg/cm^2) carbon reset foil was placed a few centimetres downstream of the target, to equilibrate the charge state of recoil ions leaving the target.

3.3 The Fragment Mass Analyser

The Fragment Mass Analyser (FMA) (Fig. 3.2) is an electromagnetic separating device for nuclear reaction products. The main elements are two electric dipoles and a 40^o magnetic dipole which serve to first separate the reaction products from the primary beam and then disperse them according to their mass to charge state ratio. Figure 3.1 shows the layout of the FMA. The elements are spaced such that

Figure 3.2: The FMA

the energy dispersion vanishes to first order, increasing the energy acceptance and providing achromatic M/Q dispersion at the focal plane. Quadrupole doublets at either end of the FMA provide geometric focusing and solid-angle enhancement. The device can be rotated about the target position but for these experiments it lay along the primary beam direction in order to collect as many reaction

products as possible. In this position, the beam stops on the anode of the first electric dipole. Multiple scattering means that some beam inevitably reaches the focal plane but beam rejection is of the order of 10^{-12}. The high A/Q, energy and solid angle acceptances of $\pm$ 7 %, $\pm$ 20 % and $\sim$ 8 msr make it a powerful tool in the search for exotic nuclei. Overall transmission efficiency is reaction dependent but is typically 10-20 %.

The FMA is controlled by a dedicated microcomputer, a Macintosh IIcx, running a customised application program, which constantly monitors vacuums, fields, currents and voltages. The setting-up of the FMA for a particular experiment is simply done by entering the energy, mass and charge-state of the particle which will follow the central trajectory through the FMA. The fields and necessary currents and voltages are calculated and implemented by the computer. Indeed, the optimum charge state of the particle is calculated too, but it is often necessary to change the charge state setting to avoid coincident A/Q values for recoils and beam, which might cause a large beam flux at the focal plane.

At the focal plane of the FMA, the reaction products are separated horizontally, usually with a dispersion of around 10mm/%. A typical image seen in the focal plane can be seen in fig. 3.3(a), which is an x,y plot of data taken in the focal plane detector. The mass groups can be seen clearly. In this experiment the FMA transmitted 3 charge states of the central mass as indicated in fig 3.3(b). The mass resolution (ΔM/M) achieved by the FMA is typically about 1/350.

3.4 Detection System

The layout of the basic detection system can be seen in fig. 3.4 as viewed from above. A multi-wire proportional counter lies at the focal plane of the FMA and this records the position and energy loss of the recoils as they pass through. The ions travel a further 40cm before being implanted into the silicon strip de-

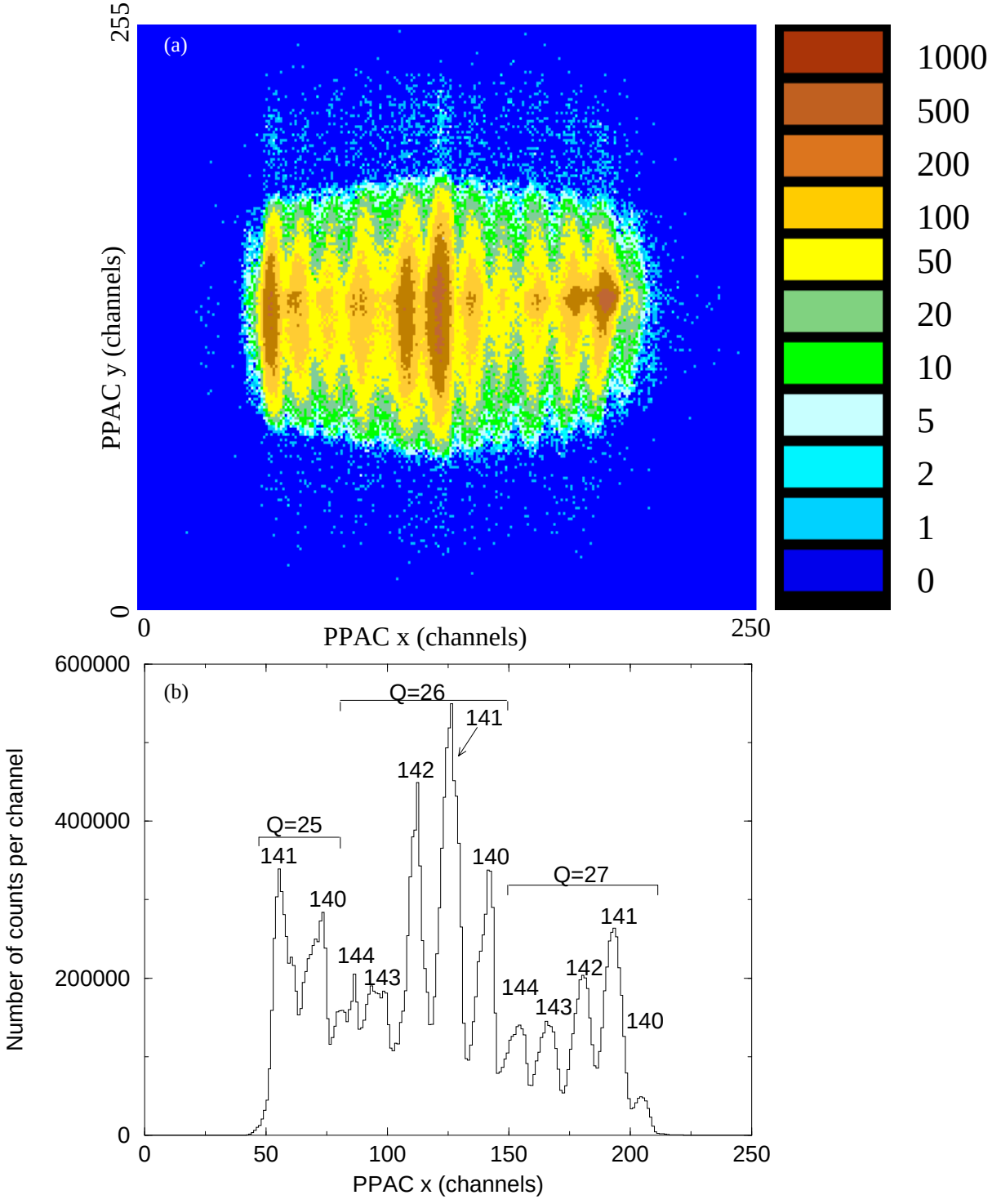

Figure 3.3: (a) x,y position of recoils in focal plane detector. (b) projection of the above onto the x-axis, indicating the mass groups and charge states.

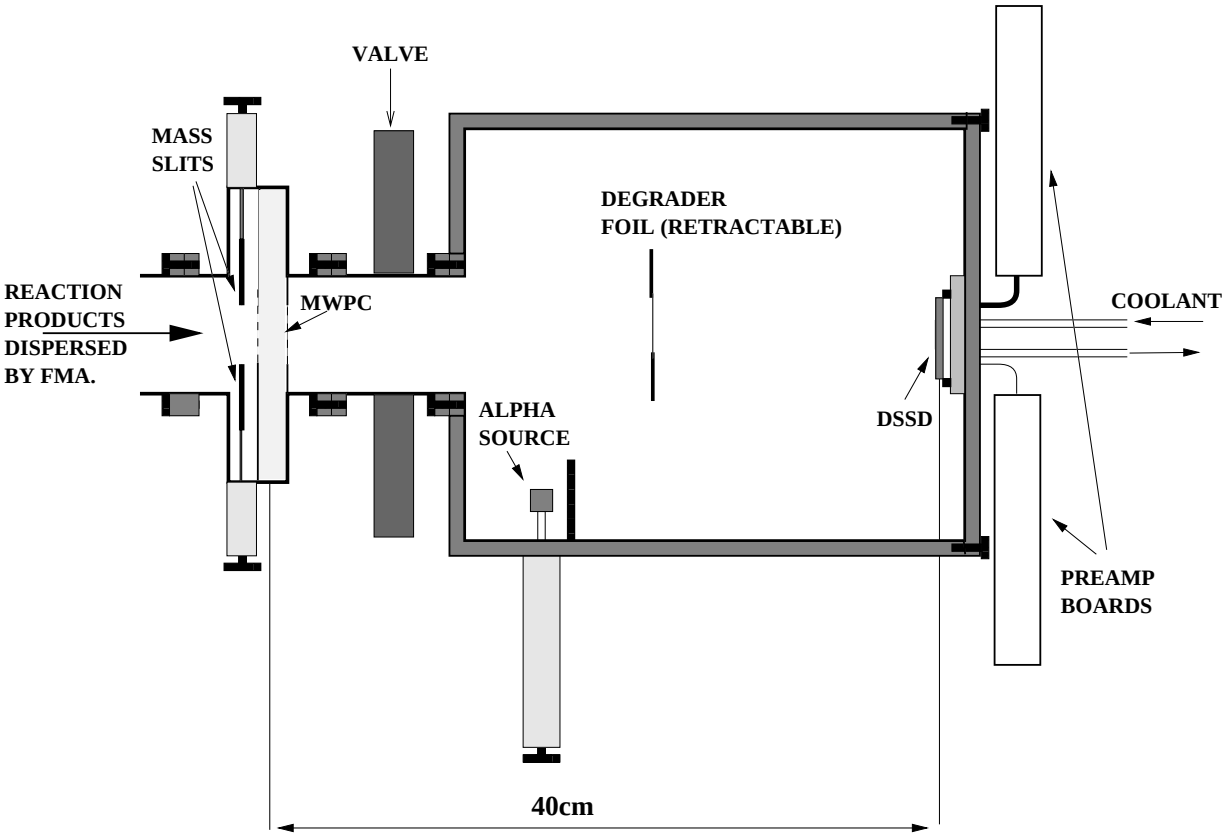

Figure 3.4: Detection system at the focal plane and beyond

tector where each event, the implant or any subsequent decay is recorded and time-stamped. An implantation event in the silicon detector is identified by a coincidence of signals from the DSSD and MWPC. Similarly, a decay (alpha or proton) event is identified by a DSSD signal without the presence of a MWPC signal. An aluminium degrader foil can be introduced in front of the DSSD to lower the implantation energy and prevent excessive overload of the decay amplifiers, although greater implantation depth is desirable to ensure that as few emitted particles as possible escape from the front face of the detector.

Implant-decay and decay-decay correlations within a pixel on the DSSD are used to identify known decays and assign new transitions to parent nuclei. The decay half-lives ultimately put a limit on the rate ions can be implanted into

the detector since one cannot be certain of the correlation of a decay with the preceding implantation event if the time between implantation events in any one pixel is comparable to the decay half-life. The dead time of the data acquisition system also limits the implantation rates in the detector. The high granularity of the DSSD and the positioning of it beyond the focal plane of the FMA both lower pixel implantation rates, and so mitigate this effect. Half-lives of proton-decaying nuclei are generally hundreds of milliseconds or less and an implantation rate of 2kHz in the DSSD is a normal figure. Mass slits can be introduced at the focal plane to focus on a particular mass group and cut out recoils from other masses and any scattered beam. However, this also eliminates other charge states of the same mass (the FMA passes three charge states of the central mass at A>100) so is not normally desirable unless background from scattered beam or a neighbouring mass group is expected to be large.

The alpha source can be introduced in front of the DSSD for the calibration and gain-matching of the 96 strips, and can be useful for monitoring any degradation in resolution due to radiation damage [Liv93].

3.4.1 Focal Plane Detector - PPAC

The detector used at the focal plane of the FMA is a multi-wire proportional counter, colloquially known as the PPAC (parallel plate avalanche counter). Recoil ions pass through a 0.8 micron thick mylar window, through a series of grids (cathode, x-position, anode, y-position) then out through the exit window. The detector is filled with isobutane at a pressure of 3 torr. Position information for the particle passing through is derived from delay line readouts from the ends of the two position grids. Energy loss information is derived from the cathode signal. The PPAC anode signal starts a TDC which is stopped by the silicon detector signal to provide time-of-flight information of the recoil from PPAC to DSSD. This proves useful in discriminating between real recoils and any scattered beam

which may have passed through the FMA (see section 3.7.1).

3.4.2 The DSSD

40cm beyond the focal plane of the FMA lies the double-sided silicon strip detector (DSSD) which lies at the heart of the detection system. A full description of this detector can be found in [Sel92a, Sel92b]. The DSSD was specifically designed for detecting and identifying proton emitters and is an extremely powerful tool for doing so, especially in the region of the drip-line above the N=82 shell closure where neutron deficient nuclei exhibit alpha decay. The recoil nuclei are defocused after they leave the PPAC and are then implanted into the front face of the DSSD, where they subsequently decay towards stability by alpha, proton and beta emission.

Being effectively transparent to beta radiation, the DSSD overcomes the problems associated with observing the particle decay of exotic nuclei, namely the large beta decaying background which swamps the alpha and proton decays. A high degree of granulation allows assignment of decays to the correct parent nuclei.

3.4.3 Design

The detectors used in these experiments were manufactured by Micron Semiconductors Ltd. and designed by the Edinburgh group. They consist of 48 p+ implanted strips on the front face orthogonally crossed with 48 n+ implanted strips on the back, creating 2304 pixels each referenced by its x and y coordinates (front and back strip numbers). Each strip is 300 μm wide by 16mm long at a pitch of 335 μm, making an active detector surface area of 225 mm^2. The thickness of the detector is 60 μm. These dimensions were chosen with several purposes in mind. The thickness was chosen to stop alpha particles (range of a 6MeV alpha in Si $\sim$30 μm) emitted in the forward direction while remaining effectively transparent to β-particles (range of a 1MeV β in Si $\sim$ 1000μm). The

small inter-strip separation (35 μm) minimises dead area and the small pixel size ensures good correlations between implantation and decay events. A larger pixel size would limit the rate on the DSSD because random correlations would confuse half-life calculations and mass assignments. A smaller pixel size would result in more complicated instrumentation and a higher proportion of dead area on the detector.

Detector depletion is achieved at 5–10 V but the DSSD is overbiased at $\sim$ 30 V to minimise any charge recombination. The detector is also cooled to -25^{o}C by a coolant pumped through the detector mount on the rear flange of the detector chamber in order to reduce noise. The energy resolution achieved with this set-up was about 20 keV FWHM for 5 MeV alpha particles, although this increased as the detector suffered radiation damage from the implanted ions.

3.4.4 Recoil-decay tagging

In the first experiment of this thesis, looking for proton radioactivity from rhenium and tantalum isotopes, a set of gamma-ray and neutron detectors known as the AYEball was positioned around the target chamber. This array consisted of 9 EUROGAM shields, 9 TESSA style shields, 7 EUROGAM germanium detectors, 1 GAMMASPHERE prototype germanium, 1 Yale germanium and an assortment of other detectors filling the TESSA shields. A photograph of the AYEball array is shown in figure 3.5. The purpose of this was to take advantage of the technique of recoil-decay tagging (RDT) to do gamma-ray spectroscopy on neutron deficient nuclei in this region. The technique is described in fig. 3.6 below and in more detail in [Pau95].

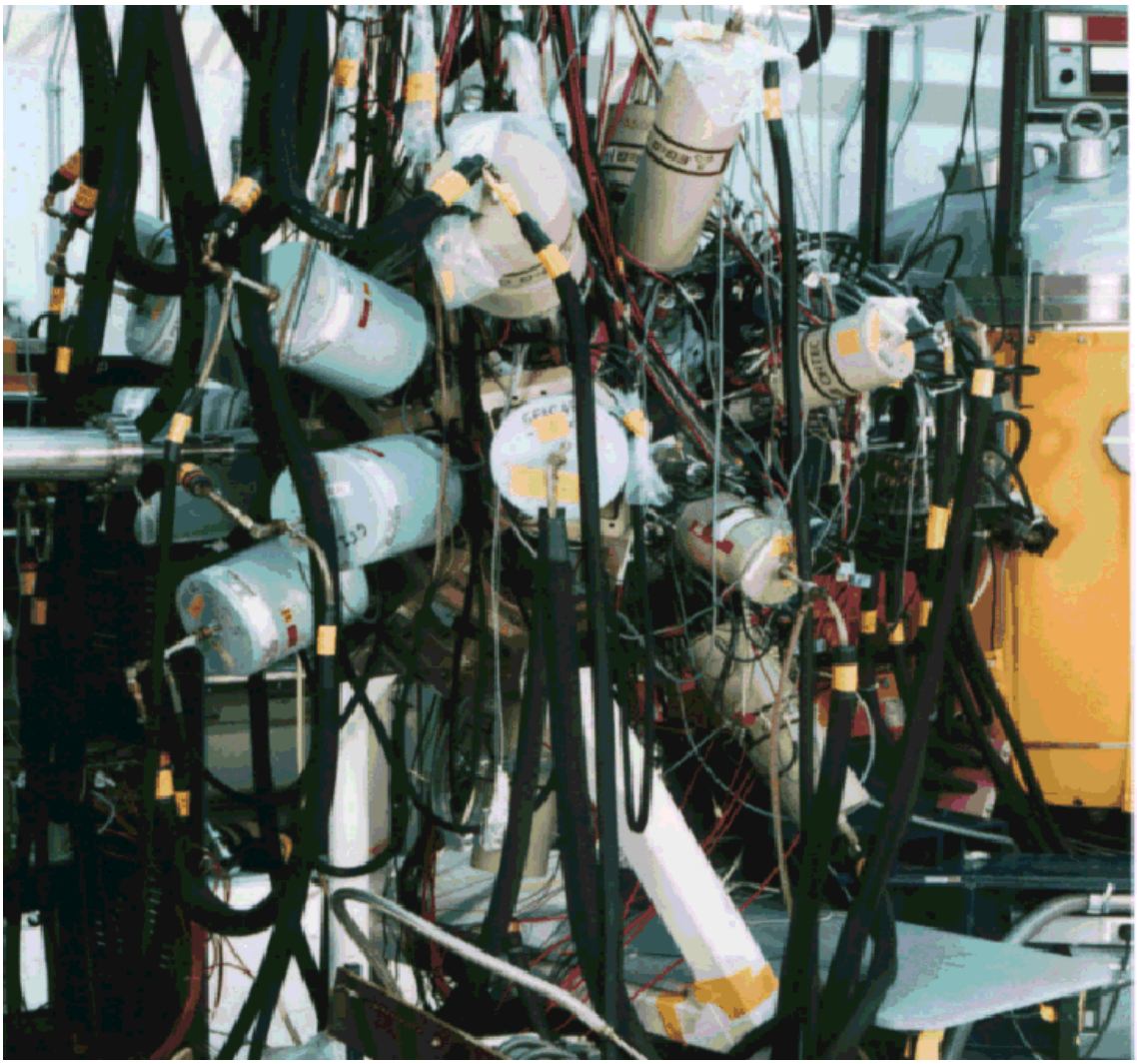

Figure 3.5: The AYEball array of gamma detectors

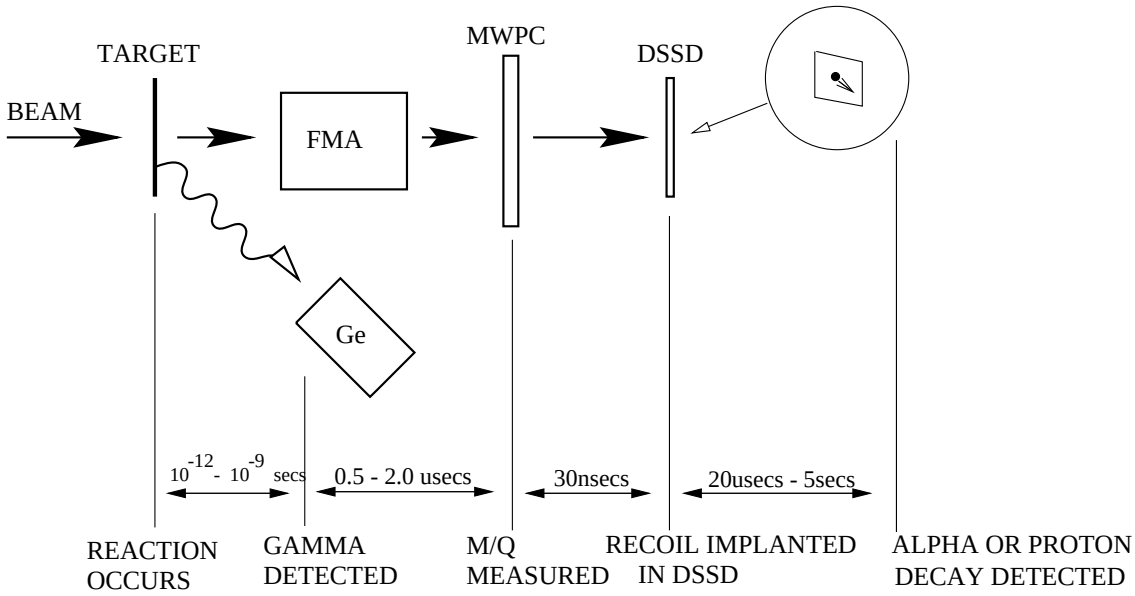

1. Prompt gamma-rays correlated with M/Q and (x,y) position of recoil in DSSD.
2. Decay proton or alpha identifies nucleus that emitted the gamma-rays.

Figure 3.6: The technique of recoil decay tagging.

A decay is identified in the DSSD and gamma-rays associated with the preceding recoil can be studied. The photopeak efficiency of the Germanium detectors was about 1% for 1 MeV γ rays, meaning that a minimum of around a few thousand alpha or proton counts would be needed in any peak in the DSSD spectrum to obtain a meaningful gamma spectrum of the nucleus from which the decay originated. The gamma-ray analysis is outside the scope of this thesis but results on gamma-rays from ^{147}Tm, a proton emitter used as a calibration for this run can be found in [Sew97].

3.4.5 Box and Back silicon Detector

In the experiment measuring proton radioactivity from ^{141}Ho there were additional detectors around the DSSD. There was another set of single sided strip detectors (known as the BOX) in front of the DSSD. The positioning of the BOX is shown in fig. 3.7. The BOX forms four sides of an open-fronted box with the DSSD board forming the back. The purpose of the BOX is to detect alphas or protons

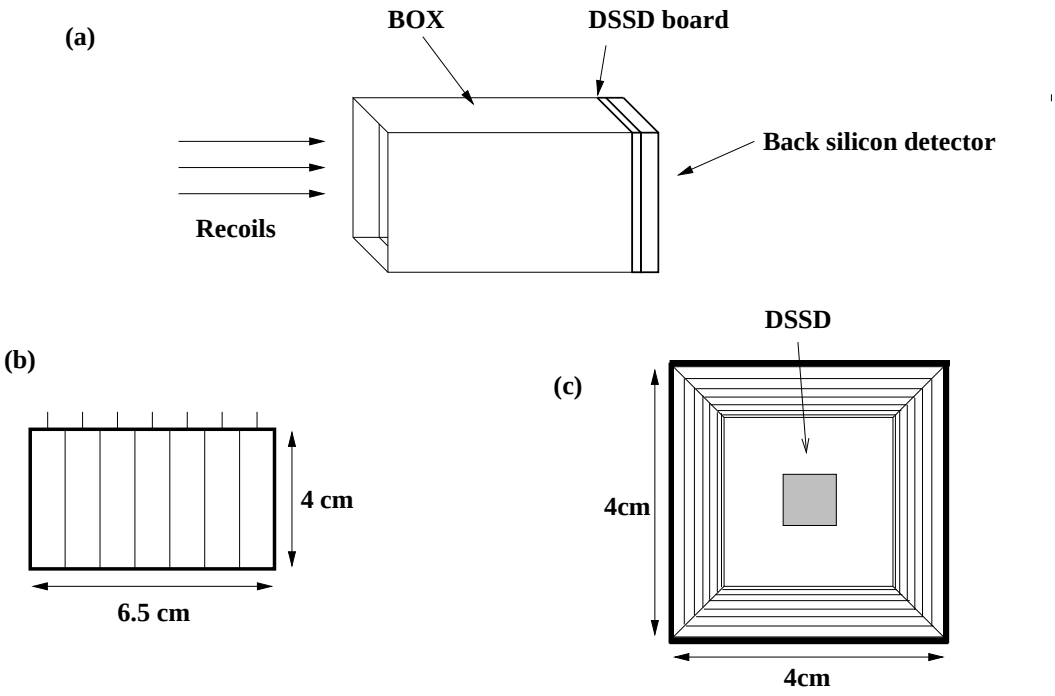

Figure 3.7: (a) Detector set-up with BOX and back silicon detectors. (b) one of the BOX detectors. (c) looking downstream into the detectors.

which escape from the front face of the DSSD without depositing their full energy in the silicon. Typical implantation depth of evaporation residues into the DSSD is about 6-10 μm, meaning that about 45% of decay particles are emitted in the backward direction such that there is insufficient silicon to stop them. These particles produce a background in the decay spectrum peaking at around 1-2 MeV, a region where some proton decays are likely to be seen. The BOX was designed to measure the position and energy of these escaping particles and BOX signals, in coincidence with DSSD signals, can either be used as a veto to eliminate these events, or as a basis for reconstructing the full energy of the decay. The solid angle for detecting backward emitted particles from the DSSD is $\sim$ 75% of 2π. In the ^{141}Ho experiment the BOX was used as simply as a veto because of the difficultly in achieving good energy resolution when reconstructing decay energies. This was a

consequence of the uncertainty in the direction of the escape particles which meant that energy losses in the BOX dead layer could not be determined accurately. An additional feature of the BOX is the possibility of observing extremely short-lived decays, previously undetectable due to the overload recovery time of the decay amplifiers (~ 30 μs) limiting the minimum detectable time between implant and decay signals. The BOX could detect fast escaping particles, although only a proportion of the full decay energy would be measured.

Behind the DSSD was a thick (300 μm) silicon detector, which was used to distinguish between direct proton emission and β-delayed proton emission. Back Si detector signals in coincidence with DSSD signals are used to veto the latter type of event. Fig 3.8 shows the effect of applying the BOX and back Si detector vetos to the decay spectrum. Background from the β^+-delayed proton continuum and alpha escape hump is much reduced.

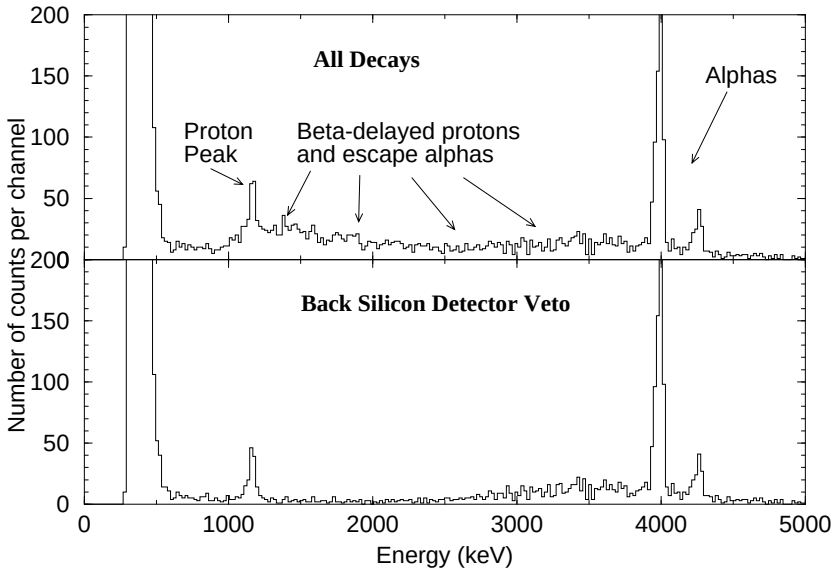

Figure 3.8: (a) Energy spectrum of all decays in the DSSD. (b) is the same as data as (a) with BOX and back Si vetos in place.

3.5 Electronics

3.5.1 Data Acquisition

The system used was the MSU/NSCL data acquisition system. A basic view of the system architecture is shown in fig 3.9. Several independent processes are involved in acquiring, monitoring and recording events to tape. The front end is

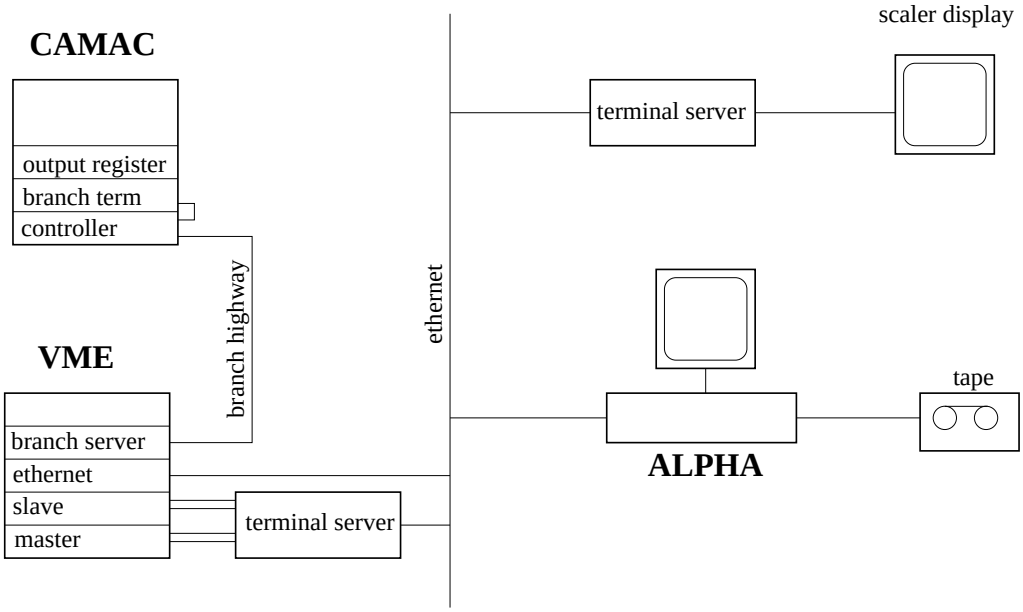

Figure 3.9: Acquisition system.

a VME based multiprocessor system in which the master packs the events into buffers and sends them out on the ethernet. The slave talks to the CAMAC crate and reads the data. When a trigger is accepted, the slave looks at the event type word to see what type of event has occurred and reads the clock, pattern register and appropriate ADCs. The slave program is written in C to be as versatile as possible, allowing customisation to minimise readout time. Readout time though is typically a few hundred microseconds and decays with implant-decay times shorter than this are measured in the following way: when a trigger is detected,

the event type word is read from the event bit register. If it is an implantation event, then once the electronics common to both implantation and decays is read out the decay busy signal is vetoed allowing it to receive new strobes. Then the recoil electronics are read and the event type word read again to see if a decay has occurred in this period. If it has, a 1 is put in the event stream to indicate a fast decay and the decay data is read out. This reduces the implant-decay dead time to about 30 μs compared to an implant-implant dead-time of 500 μs.

The back end of the acquisition system is a DEC Alpha which receives data buffers over the ethernet from the front end. A ROUTER program distributes these to processes which monitor scalers, write the data to tape and do the on-line analysis.

3.5.2 DSSD Electronics

A dedicated set of electronics has been designed for the DSSD comprising high-density preamplifiers and shaping amplifiers. Signals from the 96 DSSD strips are fed into two preamp boxes, one for the 48 p+ front strips and the other for the 48 n+ back strips, mounted on the end plate of the target chamber (see fig. 3.4) as close to the detector as possible. The signals are then fed along ribbon cables and split into two sets of 96 shaping amplifiers, to handle implantation and decay events separately. The shaping amps are mounted eight to a Eurocard mother-board and produce pulses suitable for inputs into analogue-to-digital converters (ADCs). The rise time of the output pulse is about 1 μs and the tail extends to a few microseconds. The recoil amps have a low gain ($\sim$ 5) giving a dynamic range of 200 MeV full scale, using 20mV/MeV preamps, whereas the decay amps have a higher gain (50) producing a dynamic range of 20MeV full scale. The amps are designed to have good overload recovery since both types of signal (recoil and decay) pass into both sets of amps with the effect that the high-gain decay amps are saturated by high energy implantation events. Recoils with implantation energies

of over four times the maximum range of the decay amps (80 MeV) produce a long-lived ($\sim$ 200 μs) DC pedestal which renders the amplifier insensitive to any decay signals which come in during this period. Therefore it is desirable to ensure that the recoils have an energy lower than this, introducing a degrader foil in front of the DSSD if necessary. Two potentiometers allow pole-zero and DC offset adjustments to be made for each amplifier. Analogue outputs from the recoil and decay amplifiers are fed into Philips and Silena ADCs respectively. Each shaping amp also has a leading-edge discriminator circuit producing logic pulses used for timing and event identification.

3.5.3 DSSD Logic

Fig. 3.10 shows the DSSD Logic. The ECL outputs from the decay amps go into two LeCroy 4564 modules which produce an OR of input signals 1-16, 17-32, and 33-48 in outputs 1, 2, and 3 respectively for the front and back faces. These signals then go through an ECL-NIM converter and a gate delay generator (gdg) to set bits in the ADC hit pattern register. The #10 outputs from the 4564s give an OR of all front strips and an OR of all back strips and a coincidence between these (DF.DB) fulfills the required condition for an event that at least one strip on both faces should fire. A signal from the MWPC anode is used to generate a $PPAC$ and a $\overline{PPAC}$ and coincidences between the DF+DB and these generate IMPLANT and DECAY signals respectively. These signals are used to set the ADC gates, set the relevant bit in the event type word, strobe the ADC pattern register, latch the clock and trigger the acquisition. When the event has been read out a signal is sent to clear the recoil and decay ADCs.

A schematic of the logic circuitry is shown in fig. 3.11 for the experimental setup including the BOX detector. Signals from the discriminator outputs of the BOX amplifiers set bit #5 in the event type word and set gates for the Silena ADCs to which the analogue output of the BOX decay amps are fed. A TAC

also measures the time between DSSD and BOX signals. In the ^{141}Ho experiment BOX signals were only recorded if in coincidence with DSSD signals.

3.6 Setting Up Experiments

When starting an experiment there was usually a number of uncertainties including what the actual implantation rate into the DSSD would be, how much scattered beam would pass through to the focal plane and what the optimal FMA settings are. The DSSD is quickly damaged by a high flux of recoils or beam so great care must be taken while setting up to ensure the implantation rate is kept low enough to avoid any damage.

Initially a valve is inserted immediately downstream of the PPAC to completely mask the DSSD. A computer program calculates the initial FMA settings when given the beam energy and species, target species and thickness, recoil ion of interest and other parameters relevant to the set-up. These are entered into the FMA control computer and beam is allowed to hit the target. The on-line spectra generated from the focal plane PPAC detector can be used to determine if it is safe to open the valve to the DSSD and if the FMA is optimally set up to transmit as many of the ions of interest as possible. If the mass to charge ratio of the beam is similar to that of the recoils of interest, the implants can be dominated by beam particles passing through the FMA. Therefore it is sometimes necessary to alter the FMA settings to transmit a neighbouring charge state of the recoil. The settings may also need to be altered to ensure transmission of the maximum number of charge states of the recoils (usually 3 for A>100, see fig 3.3).

Gain-matching of the 96 DSSD strips for online analysis is done by introducing a Californium/Plutonium alpha source in front of the detector for a few minutes. Gain and offset values are calculated and implemented into the online software. After making dead layer corrections this also provides a rough energy calibration

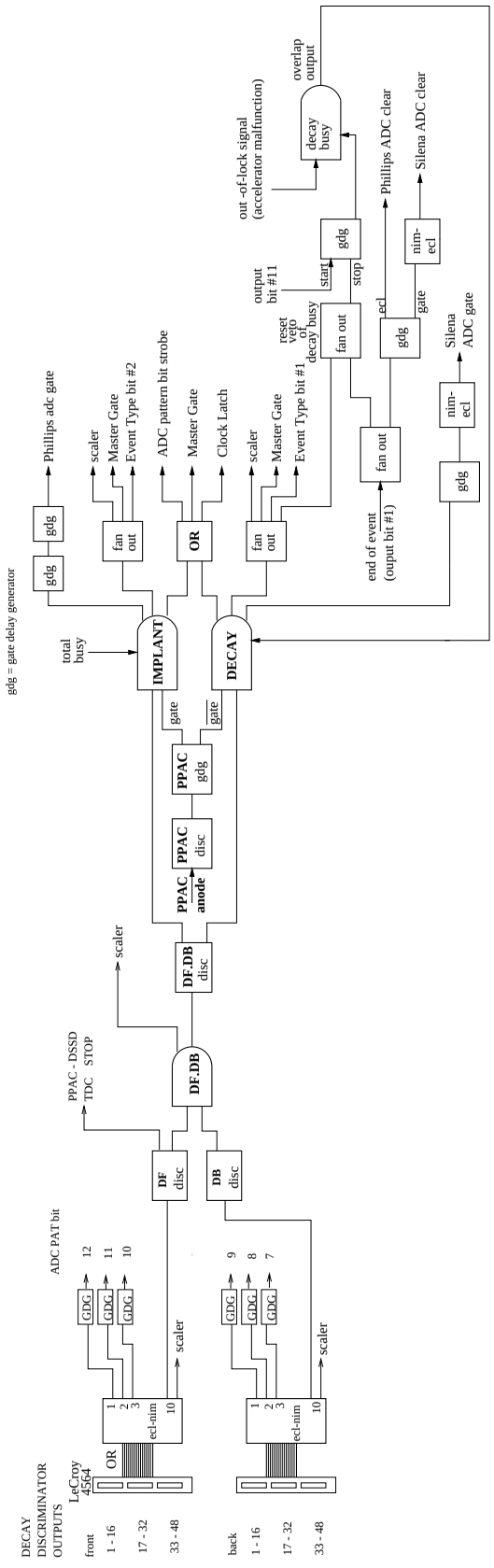

Figure 3.10: DSSD Logic.

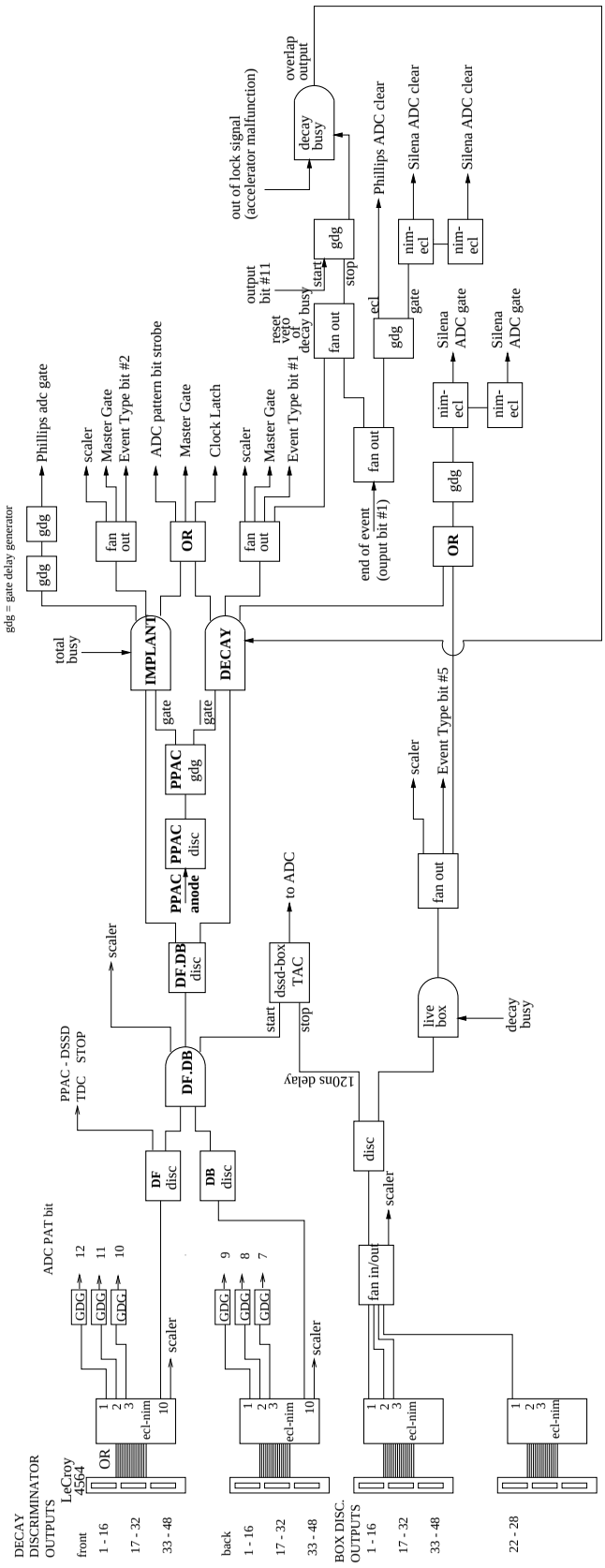

Figure 3.11: DSSD + BOX Logic.

for the decay spectra in the main run.

Once the valve to the DSSD is opened, the response of the decay amplifiers to implants can be checked and pole-zero and DC offset adjustments made to minimise baseline recovery time after overload. The overload recovery response is also checked for the pedestal effect mentioned in section 3.5.2 and a degrader foil can be introduced to reduce the energy of the recoils if necessary.

Rates in all the detectors are monitored by the SCALER process and displayed on a separate monitor at all times. These give a quick indication of any problems arising such as a hole in the target, electric discharge in the MWPC or drop-off of beam current.

3.7 Data Analysis

The analysis uses implant-decay and decay-decay correlations to identify peaks seen in the DSSD decay energy spectrum. A decay is correlated with the preceding implantation event in the same pixel and this allows a mass assignment to be made for the parent nucleus. Implantation and decay events are treated separately in the sort program, although it is made conditional for both types of event that there should be present at least one signal from each (front and back) face of the DSSD. This condition should be implemented in the DSSD electronics but a small number of multiplicity zero events 'get through' for implantation events, probably due to pickup in the electronics causing false triggers.

3.7.1 Implantation Events

No gain-matching was attempted for implantation events since good energy resolution was unimportant in the analysis. Once the strip multiplicity condition was checked, the front and back strips with the largest signal were used to reference the position, and the total energy was calculated from the sum of the two

ADC outputs for these strips. An implantation event can be one of two types, a scattered beam particle or an evaporation residue (recoil). The relative ratio of these depends on the reaction but in general a greater beam-to-target mass ratio will produce more scattered beam at the back end of the FMA. Similar mass-to-charge ratios for beam particles and recoils might also result in a high beam flux into the detectors. Beam particles passing through the FMA produce a background in the focal plane and confuse genuine recoil-decay correlations, so it is desirable to eliminate as much of them as possible. This is possible by gating on the implantation energy vs. PPAC-DSSD time-of-flight spectrum, as shown in fig 3.12. The energy-TOF characteristics are different for the recoil and beam particles and the two groups are indicated. A focal plane x spectrum gated on the recoils is shown in fig 3.13(a) and the mass groups can clearly be seen. Fig 3.13(b) shows a similar spectrum is gated on the scattered beam events and a strong peak can be seen at the left edge of the spectrum indicating some beam was being focussed onto the detector. The rest of the scattered beam is spread fairly uniformly over the focal plane. The background caused by beam particles being implanted into the DSSD would confuse any correlations between decays and the recoil implantation events. Therefore implantation events outside the recoil window in the energy – TOF spectrum are rejected. When the sort program sees a valid recoil event, its horizontal position in the focal plane detector (a measure of its mass) and its implantation time are stored in an array in a position referenced by the DSSD strip numbers into which it was implanted.

3.7.2 Decay Events

The proportion of decay events with single strip multiplicity on each face was approximately 95% of the total, the remainder reflecting a charge sharing effect between adjacent strips. Events with strip multiplicities greater than 1 were rejected because the full energy of the decay is not detected, and this would

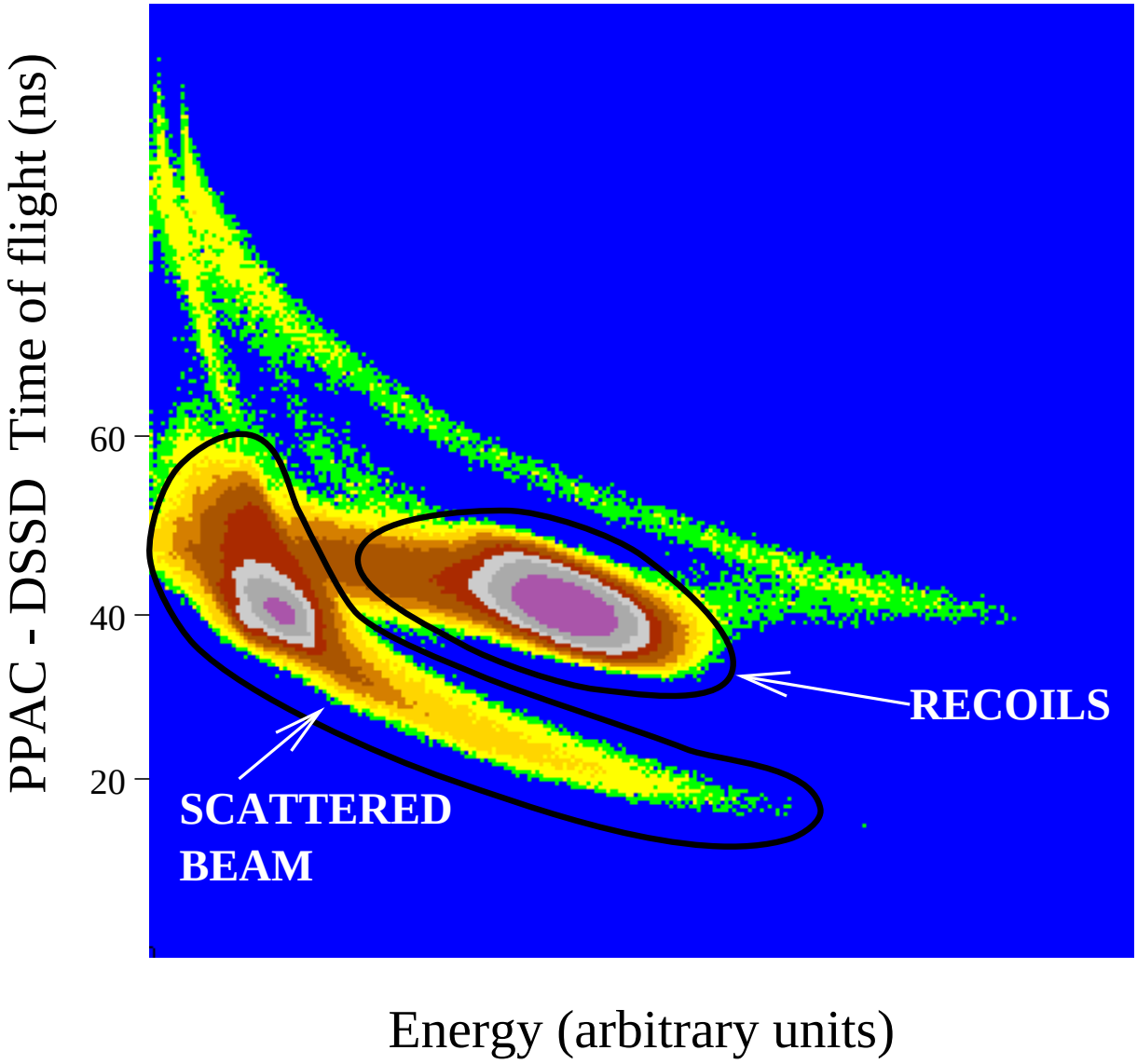

Figure 3.12: Energy – Time-of-flight spectrum for implantation events.

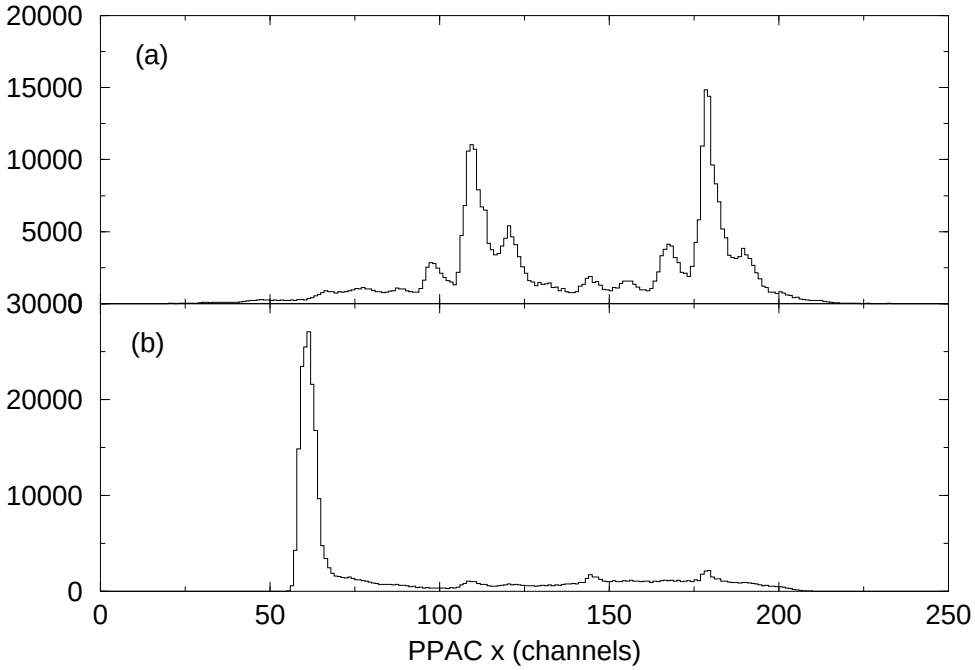

Figure 3.13: (a) Focal plane x spectrum gated on recoils. (b) Focal plane x spectrum gated on beam particles.

impair energy resolution of the alpha and proton peaks. Gain-matching strips for decay events was done using alphas lines produced in the main run which gave gain and offset values to scale peak centroids in each strip to common values. A condition was made for the front and back energies to be equal within a window of $\pm$ 50 keV, and events which failed this condition ($\sim$ 10 %) were rejected. These conditions produced an energy resolution of $\sim$ 25 keV FWHM for the alpha peaks in the main experiment. A typical energy spectrum for valid decay events fulfilling the above conditions is shown in fig 3.14(a). The peaks from 4-6 MeV are the alphas and the broad continuum down to $\sim$ 1 MeV is the escape alpha hump mentioned in section 3.4.5.

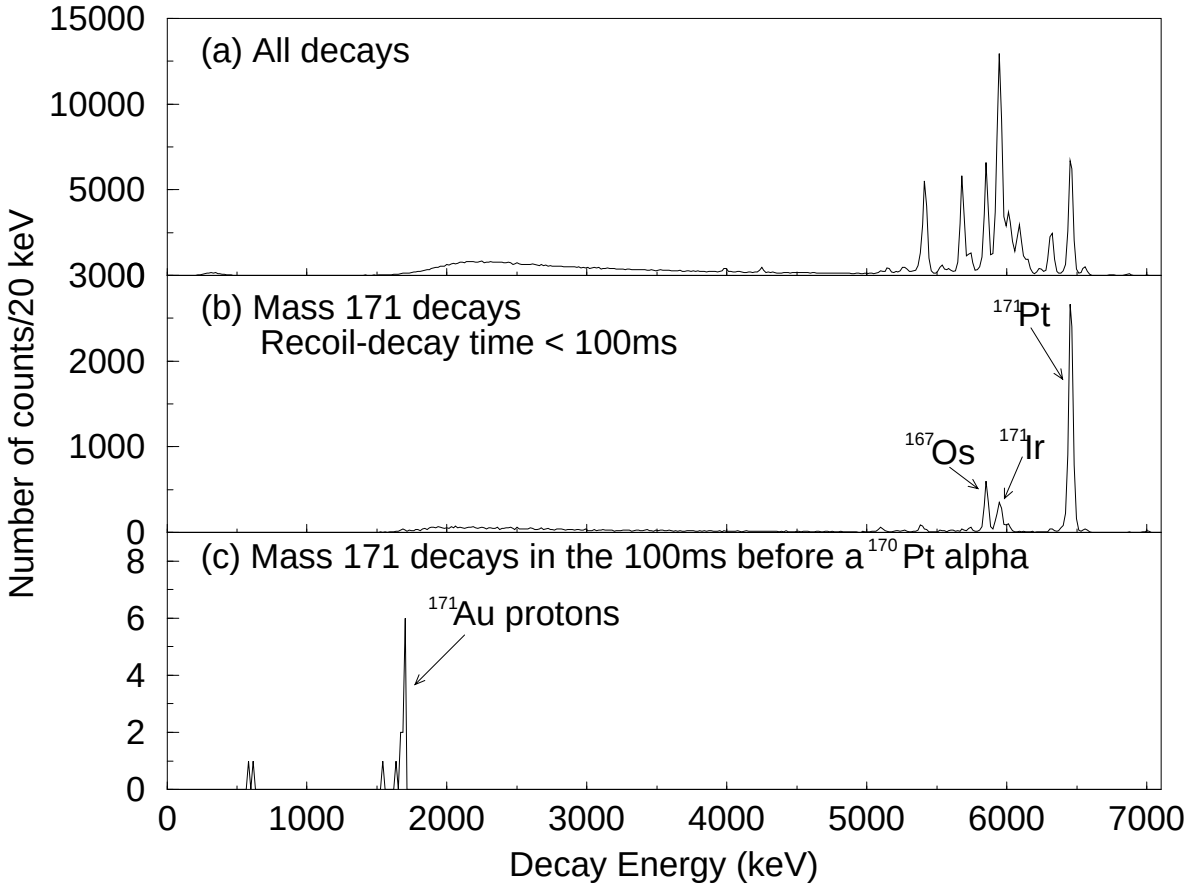

Figure 3.14: (a) A typical DSSD decay spectrum, in this case for the reaction of 390 MeV ^{78}Kr on a ^{96}Ru target. (b) Mass 171 gated decay spectrum. (c) Mass 171 gated spectrum requiring a further correlation with the subsequent alpha decay of ^{170}Pt.

3.7.3 Mass Assignment of Decays

When the sort program sees a decay event it looks in the recoil array mentioned in section 3.7.1 at the position referenced by the front and back strip numbers, to find information on the preceding implantation event at that location on the DSSD. There is a certain probability, depending on the half-life of the nucleus, the implantation rate in the detector and the time between implantation and decay events, that the decay originated from that implanted nucleus. By insisting on the condition that the decay occurs within a time window short relative to the average time between implantation events in one pixel (usually around a few seconds), a firm correlation can be made to the parent nucleus.

Then the mass of the nucleus from which the decay originated can be derived from the x position of the recoil in the focal plane detector. A plot of decay energy against mass of implanted recoil for the reaction ^{78}Kr(390 MeV) + ^{96}Ru is shown in figure 3.15 for those events with recoil-decay times < 100 ms. The

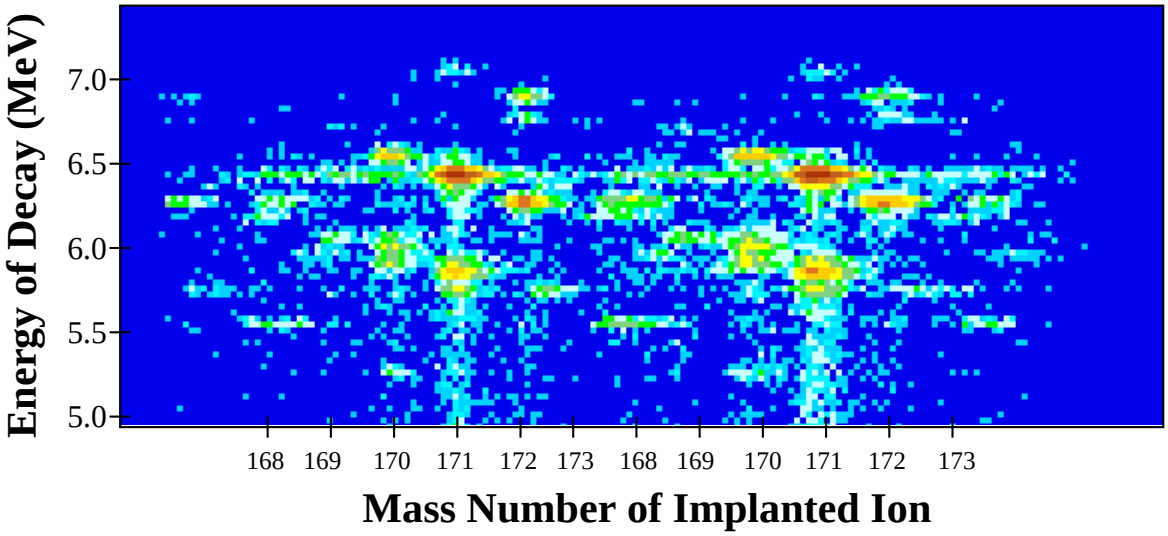

Figure 3.15: Decay Energy vs. Mass of Previous Implant

decay peaks are clearly associated with particular mass groups and this facilitates

initial identification of the peaks, which can be complicated when 20 - 30 alphas are present in the decay spectrum as in fig 3.14(a). Once the strong lines are assigned to known alpha peaks, an accurate energy calibration can be obtained. An energy spectrum of mass 171 gated decay events with an implantation decay time of < 100 ms can be seen in fig 3.14(b).

Decay-decay correlations allow unambiguous assignment of a decay to a particular isotope for those proton and alpha emitters whose daughter nuclei have an alpha decay branch. Fig 3.16 shows the region of the isotopic chart being investigated in these experiments. Alpha decay is not seen across or below the N=82 shell closure indicated by the dark lines, and below N=84 nuclei decay by β emission alone, making decay-decay correlations impossible. Nuclei in this region with N$\geq$84 do exhibit alpha decay and for some high Z nuclei, decay chains can be mapped for several generations by examining decay sequences in single pixels.

An example of how the implant-decay-decay correlation can be used is shown in figure 3.14 for the reaction ^{78}Kr(390 MeV) + ^{96}Ru $\longrightarrow$ ^{184}Hg. (a) shows the energy spectrum of all valid decay events seen in the DSSD. (b) is an energy spectrum of decays occurring within 100 ms of a mass 171 implantation event. The mass gate provides a fairly clean selection of decays originating from a mass 171 implantation event. The ^{167}Os peak is present as the daughter alpha decay of ^{171}Pt. (c) shows the data of (b) with a further correlation required, that of the subsequent decay in the same pixel within 100 ms with an energy corresponding to the alpha decay of ^{170}Pt. The proton peak is clearly observed with no background.

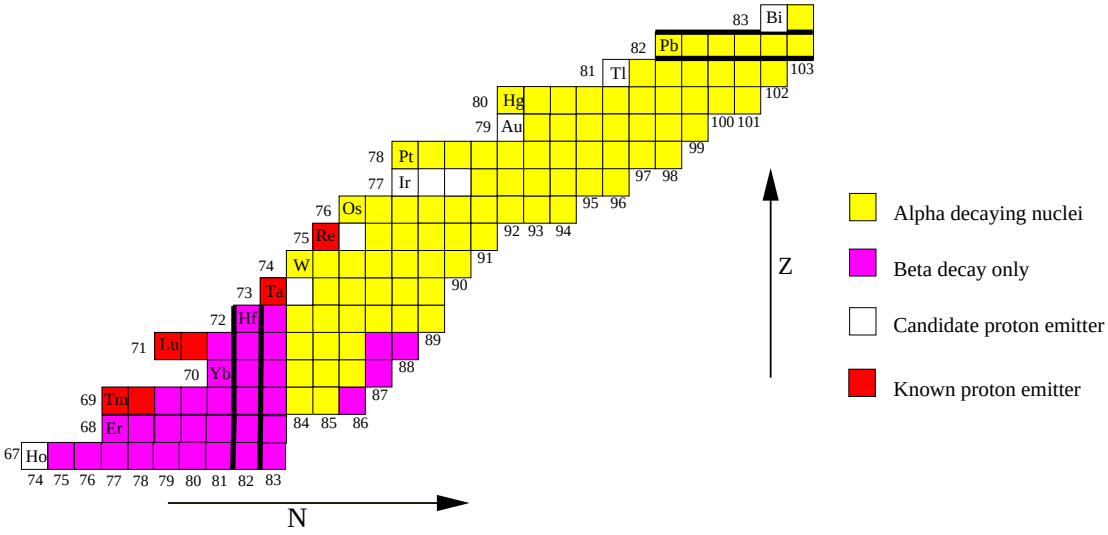

Figure 3.16: Region of the isotopic chart being studied in this work.

Chapter 4

Results

Results are presented here for a series of experiments performed at Argonne National Laboratory to search for new proton radioactivities in the region around the N=82 shell closure. The main work, for which I personally did the analysis, focuses on transitions from states in ^{157}Ta, ^{161}Re and ^{141}Ho and gives details of measurements from a preliminary experiment on proton emission from ^{171}Au and ^{167}Ir, which were repeated later with new electronics. Major results from contemporary experiments at the FMA on nuclei near the proton drip-line are also presented.

The results on proton emission from ^{157}Ta and ^{161}Re are reported in [Irv97], from ^{141}Ho in [Dav98] and from ^{171}Au and the Ir isotopes in [Dav97].

4.1 Proton Decay from ^{157}Ta and ^{161}Re

Previous experiments [Pag92, Liv93] succeeded in identifying ground state proton emission from ^{156}Ta and ^{160}Re, both of which have 25 neutrons fewer than their closest stable isotopes. Mass models predict neighbouring isotopes one neutron closer to stability also to be proton-unstable and experimentally observable, although with greater competition from alpha decay. The odd-even nature of these

two nuclei simplifies the deduction of the level schemes compared to their odd-odd neighbours and they were considered as good candidates for providing useful information on the phenomenon of proton radioactivity.

4.1.1 Experimental details

For these experiments the detector set up was a 48X48 DSSD downstream of the focal plane of the FMA and the AYEball array around the target position to do gamma ray spectroscopy using recoil-decay tagging. In the first experiment a 270 MeV, 3 particle nA beam of ^{58}Ni ions was used to bombard a 1 mg/cm^2 thick ^{102}Pd target for a period of 33 hours to produce the compound nucleus ^{160}W at a centre-of-target excitation energy of 53 MeV, calculated to produce the highest yield of ^{157}Ta via the 1p2n evaporation channel. Initially the FMA was set up to transmit a mass 157 recoil in charge state 26 in its central trajectory to transmit 3 charge states (25^+,26^+,27^+) of the central mass through to the focal plane. However on-line spectra revealed that the outer charge states were being passed with much reduced efficiency so the FMA charge setting was changed to 25.5, which had the effect of producing two mass 157 groups, in charge states 25 and 26 symmetrically either side of the central position in the focal plane, as shown in fig 4.1. This had the desired effect of producing a substantial increase in the yield of mass 157 residues at the DSSD.

The second reaction used a 1.1 mg/cm^2 ^{106}Cd target, which was irradiated for a period of 38 hours with a beam of 270 MeV ^{58}Ni ions, again designed to maximise the 1p2n evaporation yield to produce the candidate proton emitter ^{161}Re. The FMA settings for the central projectile were mass(M)=161, charge state(Q)=+26.75 and energy(E)=83.7 MeV, so that 2 charge states of the central mass were transmitted through to the focal plane. Again, it was found in the setting-up stage that this was the optimal setting for maximum transmission of the required reaction residues.

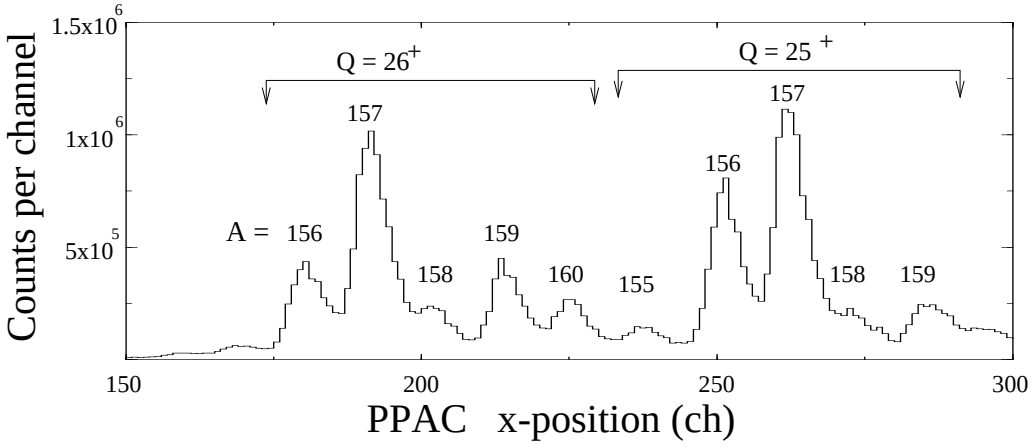

Figure 4.1: x position of recoils in focal plane detector for the ^{157}Ta experiment. Mass and charge state for each group is indicated.

4.1.2 Decays from ^{157}Ta

The energy spectrum of all decays observed in the reaction

$$^{58}\mathrm{Ni}(270MeV) + ^{102}\mathrm{Pd} \longrightarrow ^{160}\mathrm{W}^{*} \xrightarrow{1p2n} ^{157}\mathrm{Ta}$$

is shown in figure 4.2. There is a large number of alpha emitters in this region and the decay spectrum contains around 25 discernible alpha peaks between 3.5 MeV and 9 MeV. The broad structure extending down to $\sim$ 1 MeV is due to alphas escaping from the front face of the DSSD and it obscures any proton peaks there might be in this region. Three high energy alpha peaks were assigned to known isomeric states in ^{155}Lu, ^{156}Hf and ^{158}W, and all the remaining lines except one were assigned on the basis of their energies, half-lives and recoil mass assignments to known alpha transitions, as indicated in figure 4.3. The peak marked with a question-mark in figure 4.3 has an energy of 6117 $\pm$ 4 keV and has never been observed before. It has a half-life of 10.4 $\pm$ 0.4 ms and it correlated with a preceding implanted ion of mass 157. This line was assigned to a new alpha decay from ^{157}Ta on the basis of the mass assignment and a correlation between the

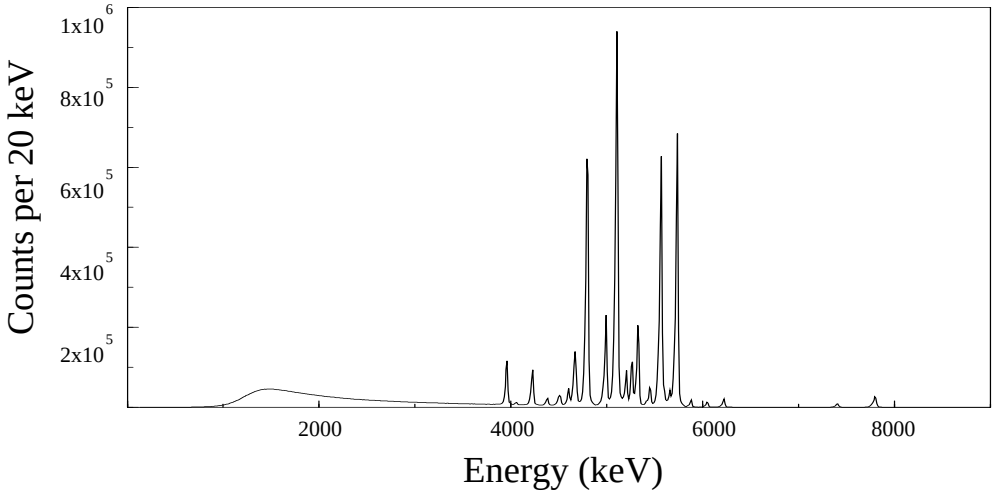

Figure 4.2: Energy spectrum of all decays observed in the DSSD in the reaction

peak and the subsequent alpha decay of ^{153}Tm, the great-granddaughter of ^{157}Ta, the two intermediate nuclei being β emitters are not observed in the DSSD.

The identification of the proton peak from ^{157}Ta was made using correlations with preceding implantation events and subsequent decay events, and the process is illustrated in figure 4.4. (a) shows all the decay events observed in the reaction. (b) shows only those events which occurred in a 50 ms time interval in the same pixel in the DSSD after a mass 157 recoil implantation event. The short time gate was imposed to minimise background from unwanted alpha peaks. Only short-lived or very strong mass 157 peaks should survive these conditions although the spectrum does show a small amount of contamination from other masses in a neighbouring charge state and due to 'leakage' from neighbouring and slightly overlapping mass groups. Despite the short time gate the escape alpha hump is still too large however for any weak proton line to be observed. (c) shows an energy spectrum of those decays with the above mass gate and the extra requirement that a subsequent decay, with energy 5873 $\pm$ 100 keV, occur in the same pixel within 100ms. This energy range was used to select as much as possible of the alpha

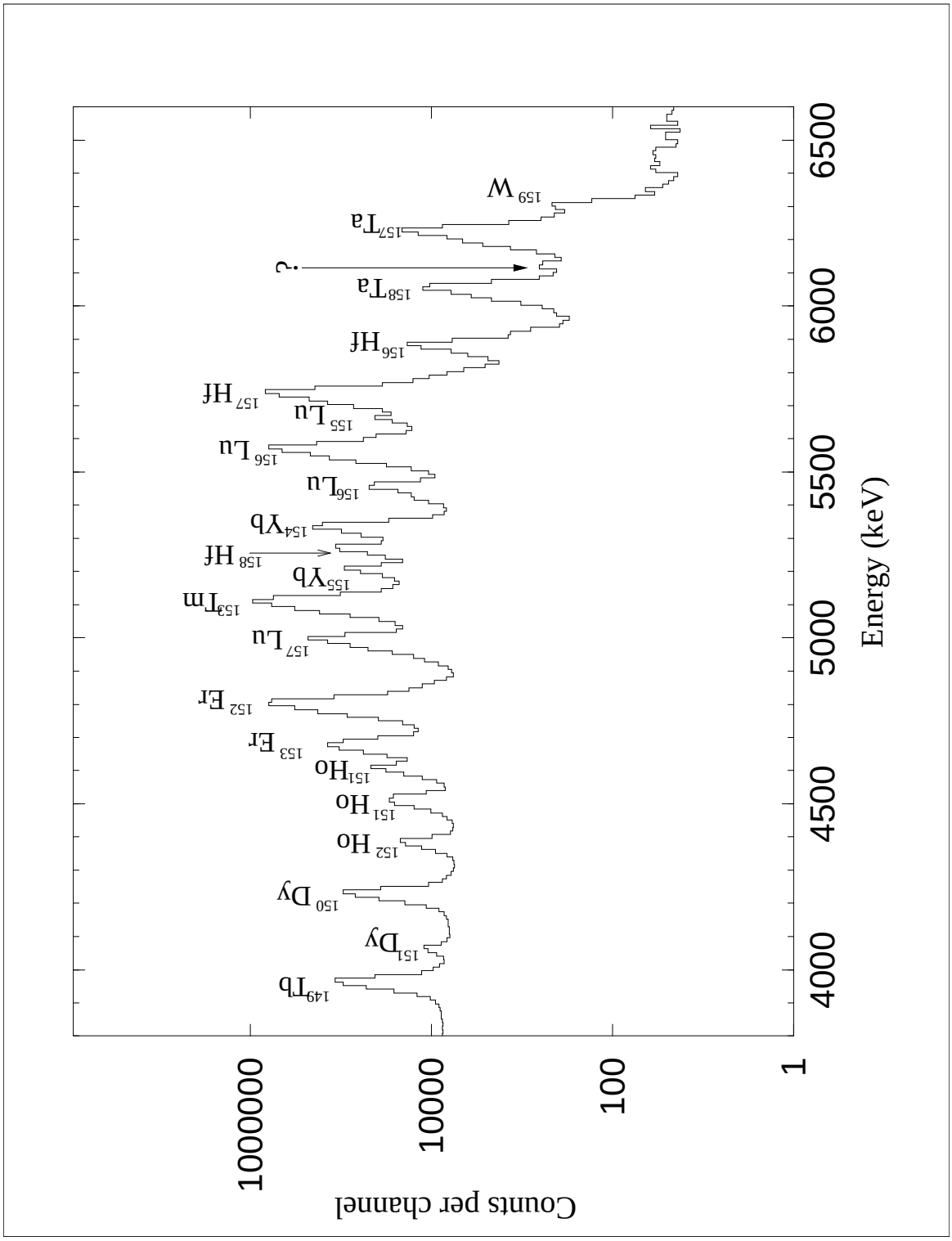

Figure 4.3: Assignment of alpha peaks produced in the reaction ^{58}Ni + ^{102}Pd.

peak from ^{156}Hf (E_α = 5873 ± 4 keV) as the subsequent decay. Clearly present is a sharp peak at 927 ± 7 keV which can be unambiguously assigned to proton decay from ^{157}Ta on the basis of the above correlations.

The energy of the proton peak was measured using data from the strong, well-known alpha peaks and the ^{147}Tm proton peak produced in a calibration run at the end of the experiment. Corrections were made for pulse height deficit due to non-ionising energy loss [Len90], and the recoil contribution to the measured pulse height [Hof89]. Details are given in table 4.1. There were 18 counts in the full

Peak energy E_{PEAK}	925.6 ± 6.8 keV
Proton pulse height deficit PHD_p	2.8 keV
Recoil Energy E_R	5.9 keV
Recoil contribution to pulse height E_{RC}	1.2 ± 0.6 keV
Proton screening correction E_{sc}	14.3 keV
Proton energy $E_p = E_{PEAK} + PHD_p - E_{RC}$	927 ± 7 keV
$Q_p = E_p + E_R$	933 ± 7 keV
$Q_{p,nuc} = Q_p + E_{sc}$	957 ± 7 keV

Table 4.1: Calculation of proton energy for ^{157}Ta.

energy proton peak, corresponding to a production cross-section of 20 nb. Due to the small number of counts in the peak, the method of maximum likelihood was used for the half-life, which was calculated as $12.1^{+3.1}_{-2.3}$ ms. Therefore the proton cannot originate from same state as the previously observed alpha line at 6213 ± 4 keV, which has a half-life of 4.3 ± 0.1 ms [Pag96]. However, within uncertainties, this value is in agreement with the value of 10.1 ± 0.4 ms obtained for the half-life of the new alpha line assigned to ^{157}Ta, at E_α = 6117 ± 4 keV. It is therefore probable that the proton and the new alpha come from the same state in the parent nucleus. On this basis the proton branching ratio from this state is calculated to be 0.034 ± 0.012 and the proton partial half-life, 300 ± 110 ms,

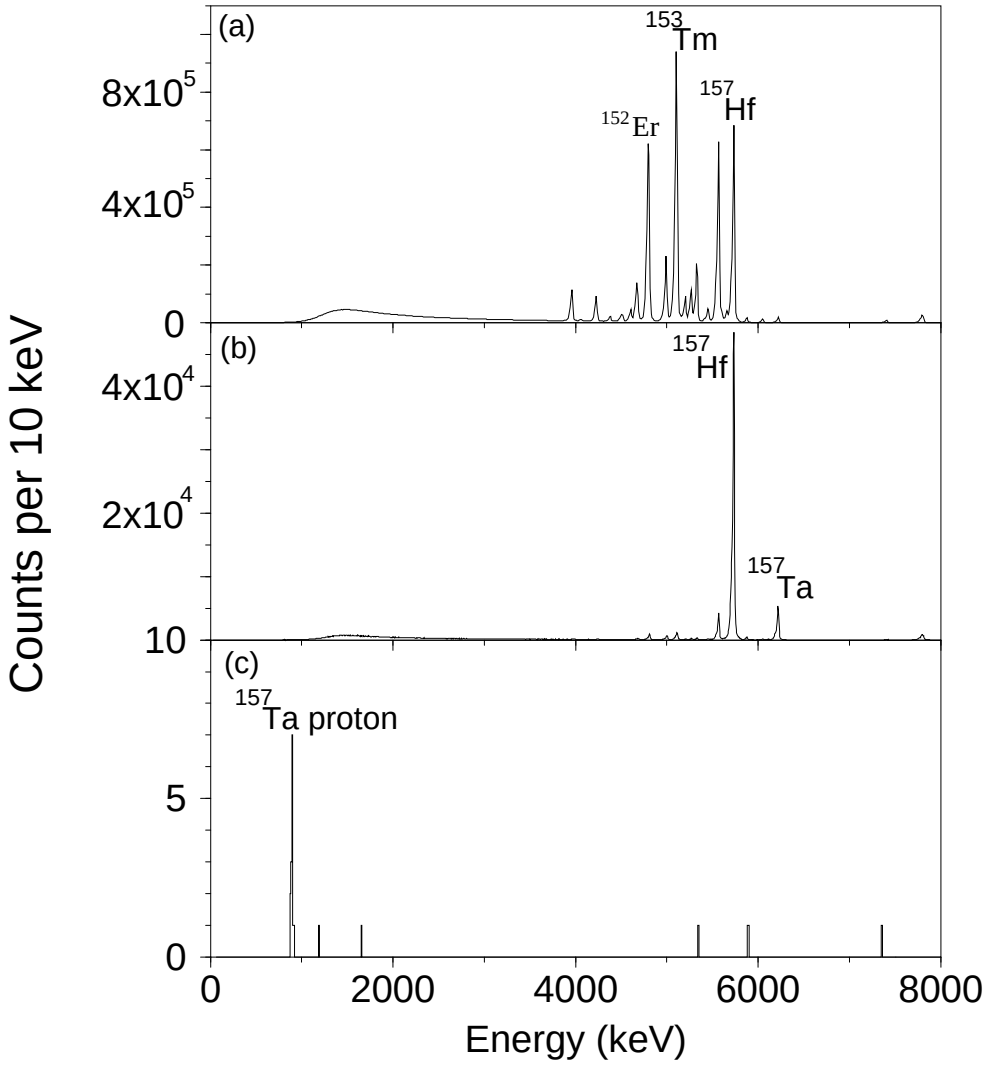

Figure 4.4: (a) Energy spectrum of all decay events in the DSSD in the reaction of 270 MeV ^{58}Ni ions on a ^{102}Pd target. Assignments are indicated for the most intense alpha decay lines. (b) Decay data after requiring that a mass 157 implant was the parent and that the first generation decay took place within 50 ms of the implantation. (c) Same data as (b) subject to the additional requirement that a second generation decay occurred in the same pixel within 100ms of the first one, with an energy of 5873 $\pm$ 4 keV, the known alpha decay of ^{156}Hf.

assuming that β-decay from this state is negligible. This last assumption is valid because the 10.1 ms half-life is short compared to characteristic β-decay half-lives in this region of around a few seconds.

4.1.3 Decays from ^{161}Re

The reaction

$$^{58}\mathrm{Ni}(270MeV) + ^{106}\mathrm{Cd} \longrightarrow ^{164}\mathrm{Os}^{*}(E_{ex} = 53MeV) \xrightarrow{1p2n} {}^{161}\mathrm{Re}$$

was used to search for proton emission from ^{161}Re. Figure 4.5(a) shows an energy spectrum of all decays observed in the reaction. Again, there is a large number of alpha decays (identified and labelled in figure 4.6) and a sizeable escape alpha hump which hides the region of interest for proton decays. Figure 4.5(b) shows decays occurring in the the same pixel as, and in the 50ms immediately after, a mass 161 implantation event. The main peaks in the spectrum are the ^{161}W alpha (E_α=5775 $\pm$ 5 keV) produced via the 2p1n evaporation channel, the ^{161}Re alpha (E_α=6265 $\pm$ 6 keV) and its daughter alpha decay ^{157}Ta (E_α=6213 $\pm$ 4 keV). This last peak is present because the half-lives of the α decays from ^{161}Re and ^{157}Ta are 15.1 $\pm$ 3.6 ms and 5.5 $\pm$ 1.7 ms, respectively, and therefore most ^{161}Re nuclei undergo a double decay within the 50ms time interval after the implantation. It should be noted that the alpha from ^{161}Re feeds the state producing the previously observed alpha at 6213 keV , not the new state mentioned in section 4.1.2. This mass and recoil-decay time gate substantially reduces the background caused by the alpha escape hump and two small peaks can be observed in this spectrum between 1000 and 1500 keV.

By requiring a further correlation with the subsequent alpha decay of ^{160}W (E_α = 5912 $\pm$ 5 keV) within 1 s, the spectrum can be effectively 'cleaned' of all background. Figure 4.5(c) shows the decay spectrum with this additional condition and the proton peaks can be clearly seen. The two main peaks are at

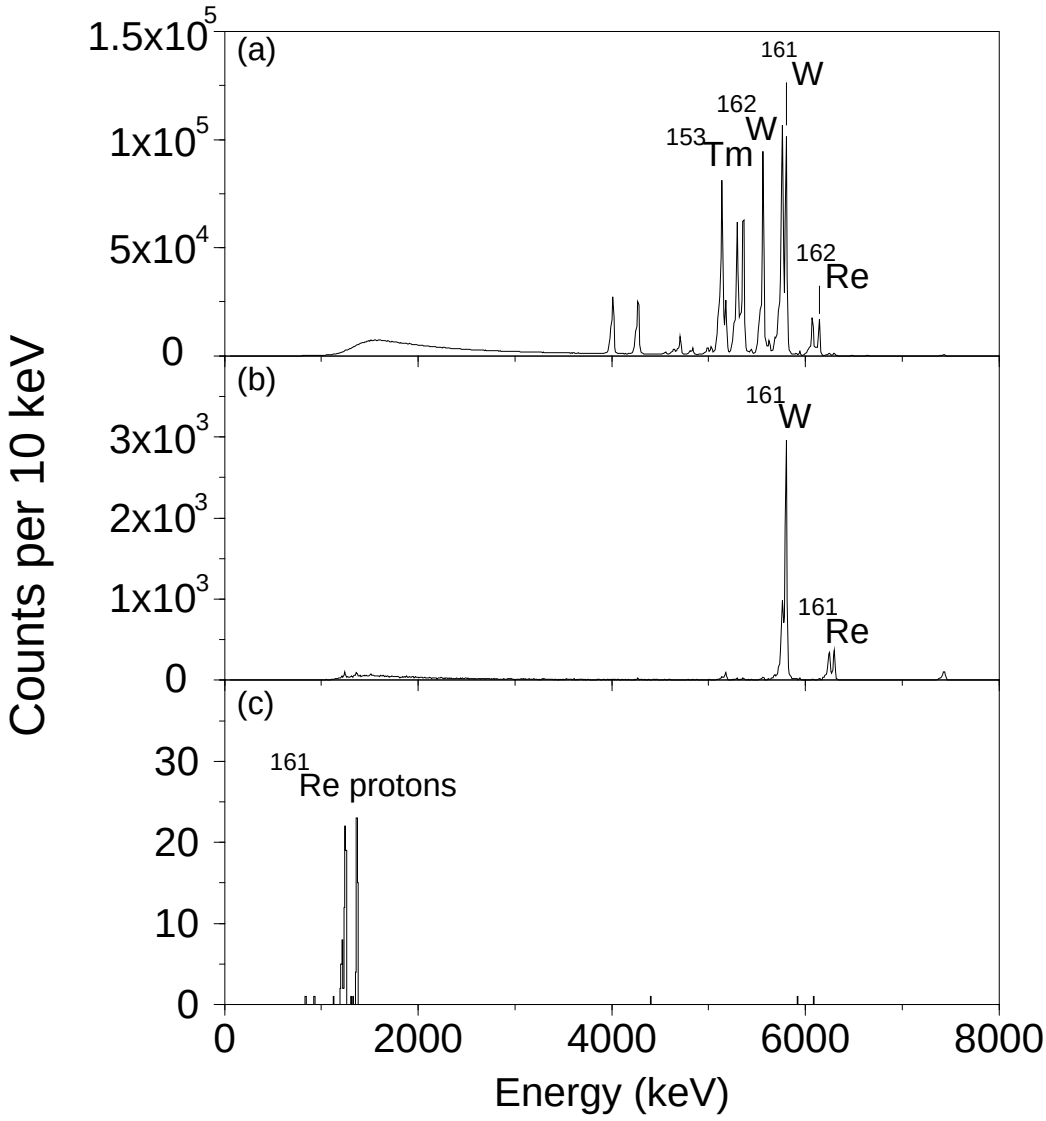

Figure 4.5: (a) All decays observed in the DSSD in the reaction of 270 MeV ^{58}Ni ions on a ^{106}Cd target. (b) First generation decays occurring within 50 ms of a mass 161 implantation. (c) Same data as (b) with the extra condition that a second generation decay occurred in the same pixel within 1 s of the first one, with an energy corresponding to the known alpha decay of ^{160}W.

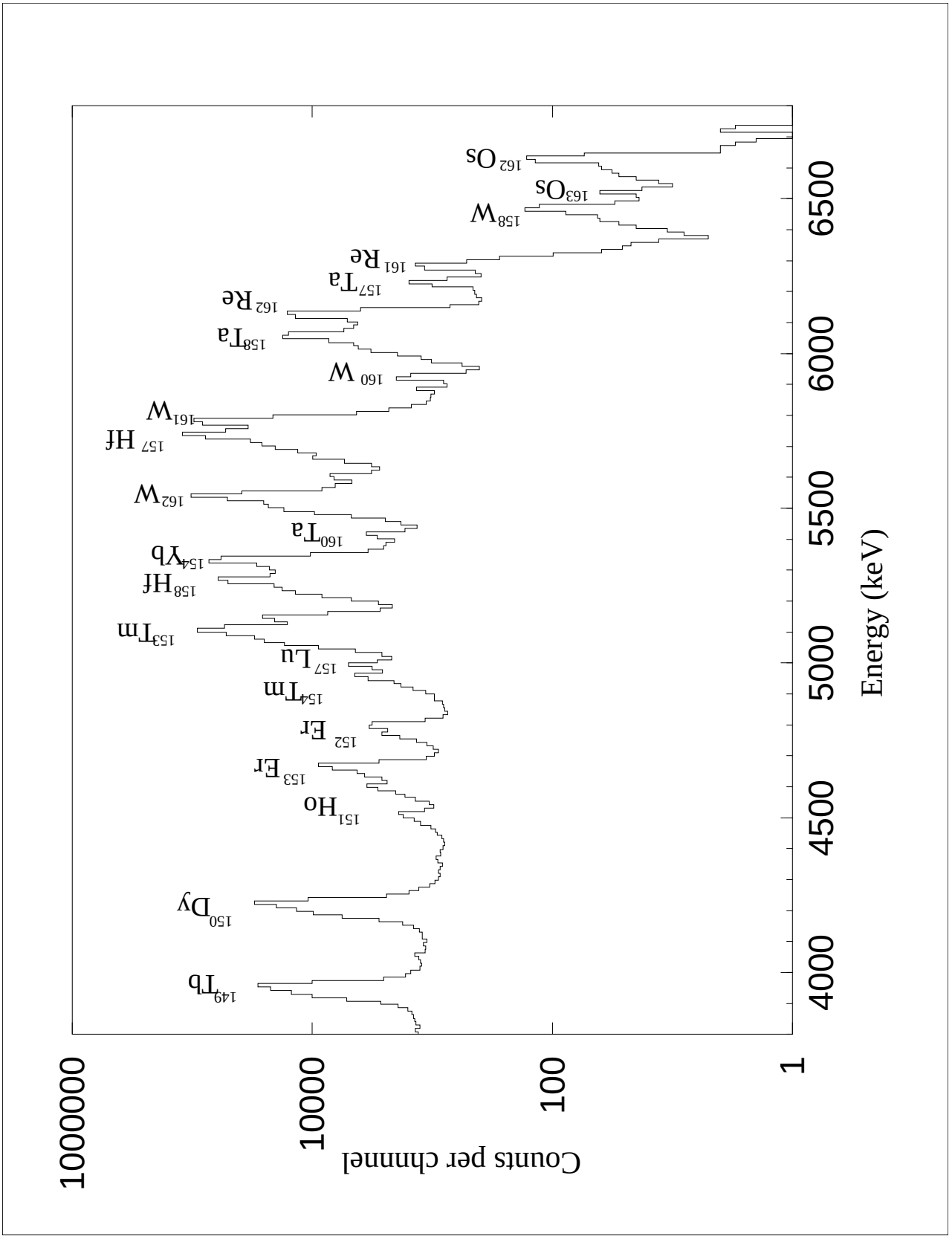

Figure 4.6: Alpha decays produced in the ^{161}Re experiment

energies of 1192 ± 6 keV and 1315 ± 7 keV, calibrated with respect to the protons from ^{147}Tm. The energy corrections made for the peaks are detailed in table 4.2.

Peak energy E_{PEAK}	1190.8 ± 5.7 keV	1313.9 ± 6.7 keV
Proton pulse height deficit PHD_p	3.0 keV	3.1 keV
Recoil Energy E_R	7.5 keV	8.2 keV
Recoil contribution to pulse height E_{RC}	1.5 ± 0.8 keV	1.6 ± 0.8 keV
Proton screening correction E_{sc}	15.0 keV	15.0 keV
Proton energy $E_p = E_{PEAK} + PHD_p - E_{RC}$	1192 ± 6 keV	1315 ± 7 keV
$Q_p = E_p + E_R$	1199 ± 6 keV	1323 ± 7 keV
$Q_{p,nuc} = Q_p + E_{sc}$	1214 ± 6 keV	1338 ± 7 keV

Table 4.2: Calculation of proton energies for ^{161}Re peaks.

The proton peaks at 1192 keV and 1315 keV are assigned to states in ^{161}Re on the basis of the above mass assignment and proton-α correlations. The two peaks contain an approximately equal number of a counts and the yields correspond to production cross-sections of ∼150 nb for both peaks.

The half-life of the 1192 keV peak is calculated as 0.37 ± 0.04 ms. No corresponding alpha line with a similar half-life was observed, and due to the small value of $t_{1/2}$, competition from β decay was considered to be negligible. The proton branching ratio from this state is therefore calculated to be 100 ± 7 %. The half-life of the 1315 keV peak was measured to be $15.4^{+1.7}_{-1.4}$ ms, consistent with the value of 16 ± 1 ms measured for the known alpha from ^{161}Re. The energy of this alpha peak was measured as 6272 ± 7 keV compared to a previous measurement[Pag96] of 6265 ± 6 keV (previous measured half-life of ^{161}Re = 14 ± 2 ms). We conclude that the 1315 keV proton and 6272 keV alpha come from the same state in the parent nucleus. By comparing yields of protons and alphas

and neglecting any small contribution there might be from a weak β branch, the proton branch from this state was calculated to be 4.8 $\pm$ 0.6 %, and the proton partial half-life, 325 $\pm$ 44 ms.

4.1.4 Level Assignments for ^{157}Ta and ^{161}Re Protons

As demonstrated in section 2.1.1, a comparison of measured and calculated proton partial half-lives can be used to determine the angular momentum of the proton-emitting states in the parent nuclei. Table 4.3 shows the results of calculations for the three proton lines observed from ^{157}Ta and ^{161}Re using the WKB barrier transmission approximation with the real part of the optical model potential of Becchetti and Greenlees [Bec69] for the available proton orbitals in this region, $s_{1/2}$, $d_{3/2}$ and $h_{11/2}$. The experimentally determined proton partial half-lives are also given.

For the 927 $\pm$ 7 keV proton decay from ^{157}Ta the $d_{3/2}$ and $h_{11/2}$ levels can be excluded as origins of the activity as the predicted half-lives are clearly too long. The prediction for the $s_{1/2}$ orbital, however, is in reasonably good agreement with the measured value indicating the proton can only be an l=0 transition from the $s_{1/2}$ state in ^{157}Ta to the J=0 ground state in ^{156}Hf. Similarly, the 1192 keV peak from ^{161}Re is best explained as the l=0 decay of the $s_{1/2}$ ground state and the 1315 keV peak can only be the l=5 decay of the $h_{11/2}$ state, both transitions going to the J=0 ground state of ^{160}W.

Nuclide	E_p (keV)	Measured partial half-life(ms)	Proton Orbital	Calculated partial half-life(ms)
^{157}Ta	927(7)keV	300(110)	$s_{1/2}$	167
			$d_{3/2}$	1470
			$h_{11/2}$	4020000
^{161}Re	1192(6)keV	0.37(4)	$s_{1/2}$	0.142
			$d_{3/2}$	1.18
			$h_{11/2}$	2600
^{161}Re	1315(7)keV	325(44)	$s_{1/2}$	0.0062
			$d_{3/2}$	0.051
			$h_{11/2}$	107

Table 4.3: Comparison of measured partial proton decay half-lives for proton emitters ^{161}Re and ^{157}Ta with those calculated using a WKB approximation with the optical-model potential of Becchetti and Greenlees.

4.1.5 Decay Scheme for ^{161}Re and ^{157}Ta

The proposed decay scheme is represented in figure 4.7. Only one alpha transition

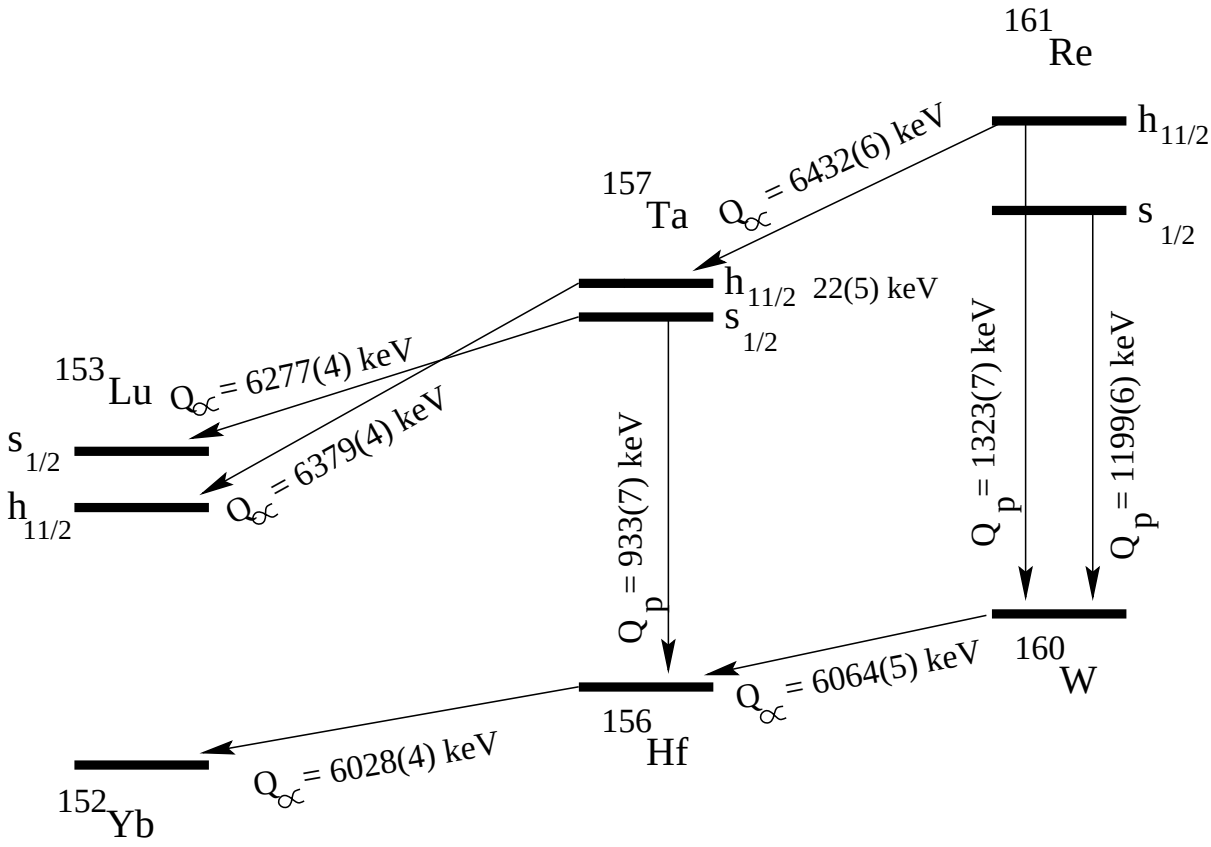

Figure 4.7: Proposed decay scheme

is observed from ^{161}Re, with a half-life of 16 ± 1 ms suggesting it originates from the same level ($h_{11/2}$) as the 1315 keV proton (measured half-life $15.4^{+1.7}_{-1.4}$ ms). Barrier penetration calculations, assuming a relative reduced width of unity compared to ^{212}Po, suggest an alpha partial half-life of ∼20 ms for an l=0 alpha and ∼400 ms for an l=5 alpha (compared to a measured partial half-life of 17 ± 1 ms) so the decay is assigned to a favoured l=0 transition from the $h_{11/2}$ state in ^{161}Re to the $h_{11/2}$ state in ^{157}Ta. The excitation energy of the $h_{11/2}$ state is 123.8 ± 1.3 keV, given by the difference in Q values between the two proton

transition from ^{161}Re. The relatively small error in this number compared to those for the individual Q values reflects the insensitivity of the energy difference to the absolute energy calibration.

Our knowledge of the proton and alpha decays from ^{157}Ta, ^{161}Re and their daughter nuclei can be exploited to give excitation energies and proton decay Q values of states from which no protons are observed. The combined Q values

$$Q_p(^{161}\mathrm{Re}[\mathrm{h}_{11/2}]) \; + \; Q_\alpha(^{160}\mathrm{W}) \; - \; [Q_\alpha(^{161}\mathrm{Re}) \; + \; Q_p(^{157}\mathrm{Ta})]$$

give an excitation energy of 22 $\pm$ 5 keV for the $\mathrm{h}_{11/2}$ state with respect to the ground state in ^{157}Ta. Hence the energy available for proton decay from the $\mathrm{h}_{11/2}$ state in ^{157}Ta is 955 $\pm$ 9 keV. Using this value in a barrier penetration calculation for l=5 proton emission to the J=0 ground state of ^{156}Hf, one obtains a proton partial half-life of around 2000 seconds. This could not compete with the observed alpha which has a half-life of 4.3 $\pm$ 0.1 ms. The expected proton branch from this state is approximately 0.0002 %. As there were $\sim$ 60000 counts in the full energy ^{157}Ta peak, the Q value is consistent with the non-observation of a proton corresponding to this transition. Similarly, the Q value for alpha decay from the $\mathrm{s}_{1/2}$ ground state in ^{161}Re to the $\mathrm{s}_{1/2}$ state in ^{157}Ta is 6330 $\pm$ 8 keV, which gives a lower limit for the proton partial half-life of $\sim$ 50 ms, too long to compete with the 0.37 ms proton decay. Again this is consistent with the non-observation of such an alpha transition.

Further, the combined Q values $\mathrm{Q}_p(^{157}\mathrm{Ta}[\mathrm{h}_{11/2}]) + \mathrm{Q}_\alpha(^{156}\mathrm{Hf}) - \mathrm{Q}_\alpha(^{157}\mathrm{Ta}[\mathrm{h}_{11/2}])$ and $\mathrm{Q}_p(^{157}\mathrm{Ta}[\mathrm{s}_{1/2}]) + \mathrm{Q}_\alpha(^{156}\mathrm{Hf}) - \mathrm{Q}_\alpha(^{157}\mathrm{Ta}[\mathrm{s}_{1/2}])$ give the energy available for proton decay from the $\mathrm{h}_{11/2}$ and $\mathrm{s}_{1/2}$ levels in the N=82 closed shell nuclide ^{153}Lu as 604 $\pm$ 10 keV and 684 $\pm$ 9 keV, respectively. Barrier penetration calculations predict proton partial half-lives of 10^{10} s and 10^4 s from these states to the J=0 ground state in ^{152}Yb. Therefore although the drip-line is clearly crossed, proton decay is unable to compete with β decay for this nucleus and protons from these states were not observed. It is interesting to note that the above results indicate

that the $s_{1/2}$ state lies 80 $\pm$ 5 keV above the $h_{11/2}$ state in ^{153}Lu, the levels being inverted with respect to ^{161}Re and ^{157}Ta. This gives an explanation why only the proton from the $h_{11/2}$ state in ^{151}Lu is observed. Assuming a similar energy gap for the $s_{1/2}$ level the proton would have a partial half-life of <1 μs, too fast to be observed with current techniques.

4.1.6 Comparison with previous results

The above results show a marked difference from those for ^{156}Ta and ^{160}Re [Liv93], in which proton emission is assigned to a ground state $[\pi d_{3/2}\nu f_{7/2}]$ 2^- configuration. This lowering in energy of the $[\pi d_{3/2}\nu f_{7/2}]$ 2^- sate relative to competing $[\pi s_{1/2}\nu f_{7/2}]$ 3^- and $[\pi h_{11/2}\nu f_{7/2}]$ 2^+ states can be found in the Nordheim strong rule. This states that the interaction between an odd neutron and odd proton occurs for the antiparallel coupling where one odd nucleon has $j = l + 1/2$ (the $f_{7/2}$ neutron) and the other odd nucleon has $j = l$ - 1/2 (the $d_{3/2}$ proton). Therefore it is the interaction strength between the odd neutron and odd proton rather than the single particle energies that plays a decisive role in determining level ordering in the odd-odd nuclei.

4.2 Proton decay from ^{167}Ir and ^{171}Au

In June 1994, an experiment took place at Argonne National Laboratory to search for proton emission from light gold isotopes. Evaporation residues from the reaction of ^{78}Kr on a 400μg/cm^2 ^{96}Ru target on a 700μg/cm^2 Al backing were separated by the FMA and implanted into a 48×48 DSSD. Beam energies of 389 MeV and 420 MeV were used to produce ^{171}Au and ^{170}Au via the 1p2n and 1p3n evaporation channels respectively. The detector instrumentation was similar to that mentioned previously, except that a different set of amplifiers were used, giving generally poorer performance. Dead-time for detecting decays was typically

as long as 500-1000 μs after an implantation event.

4.2.1 Proton decay from ^{171}Au

Figure 4.8(a) shows an energy spectrum of all decays from the reaction

$$^{78}\mathrm{Kr}\,(389\ \mathrm{MeV})\ +\ ^{96}\mathrm{Ru}\,(400\ \mu\mathrm{g/cm}^2)\ \longrightarrow\ ^{174}\mathrm{Hg}^*$$

The spectrum has the familiar shape comprising a number of discrete alpha peaks (strongest labelled) and the escape alpha hump. The inset shows the region of this spectrum between 6500 and 7200 MeV and reveals a new peak at energy 6996 $\pm$ 6 keV. This was found to be correlated with the subsequent known 6410 $\pm$ 5 keV alpha line from ^{167}Ir and therefore was assigned to the alpha decay of ^{171}Au. The half-life of this alpha group was calculated to be $1.10\ ^{+0.22}_{-0.16}$ ms. Fig 4.8(b) shows decay events occurring within 100ms of mass 171 implantation events and the spectrum is dominated by the alpha peaks from ^{171}Pt (E_α = 6453 $\pm$ 3 keV, $t_{1/2}$ = 43 $\pm$ 3 ms) and ^{171}Ir (E_α = 5945 $\pm$ 4 keV, $t_{1/2}$ = 1300 $\pm$ 200 ms). Again the inset shows the region between 6.5 and 7.2 MeV and the mass assignment of the ^{171}Au alpha peak is confirmed. Figure 4.8(c) shows the same data as (b) subject to the additional requirements that a subsequent decay event occurred in the same pixel within 100ms of the first one, with an energy of 6550 keV, the known alpha decay of ^{170}Pt. The peak, with an energy of 1689 $\pm$ 10 keV, cannot be an alpha particle because of energy considerations and is therefore identified as a proton from ^{171}Au. The half-life calculated from the proton peak was $1.05\ ^{+0.30}_{-0.22}$ ms, in agreement with that of the ^{171}Au alpha peak. It is therefore likely that the protons and alphas come from the same state. The short half-life suggests β-decay from this state will be negligible, and the proton branching ratio is calculated to be 0.37 $\pm$ 0.12, giving a proton partial half-life of 2.9 $\pm$ 1.1 ms.

From the ^{171}Au – ^{167}Ir α–α correlation, an alpha branching ratio of 0.8 $\pm$ 0.1 was deduced for the state in ^{167}Ir populated by the 6996(6) keV alpha decay of

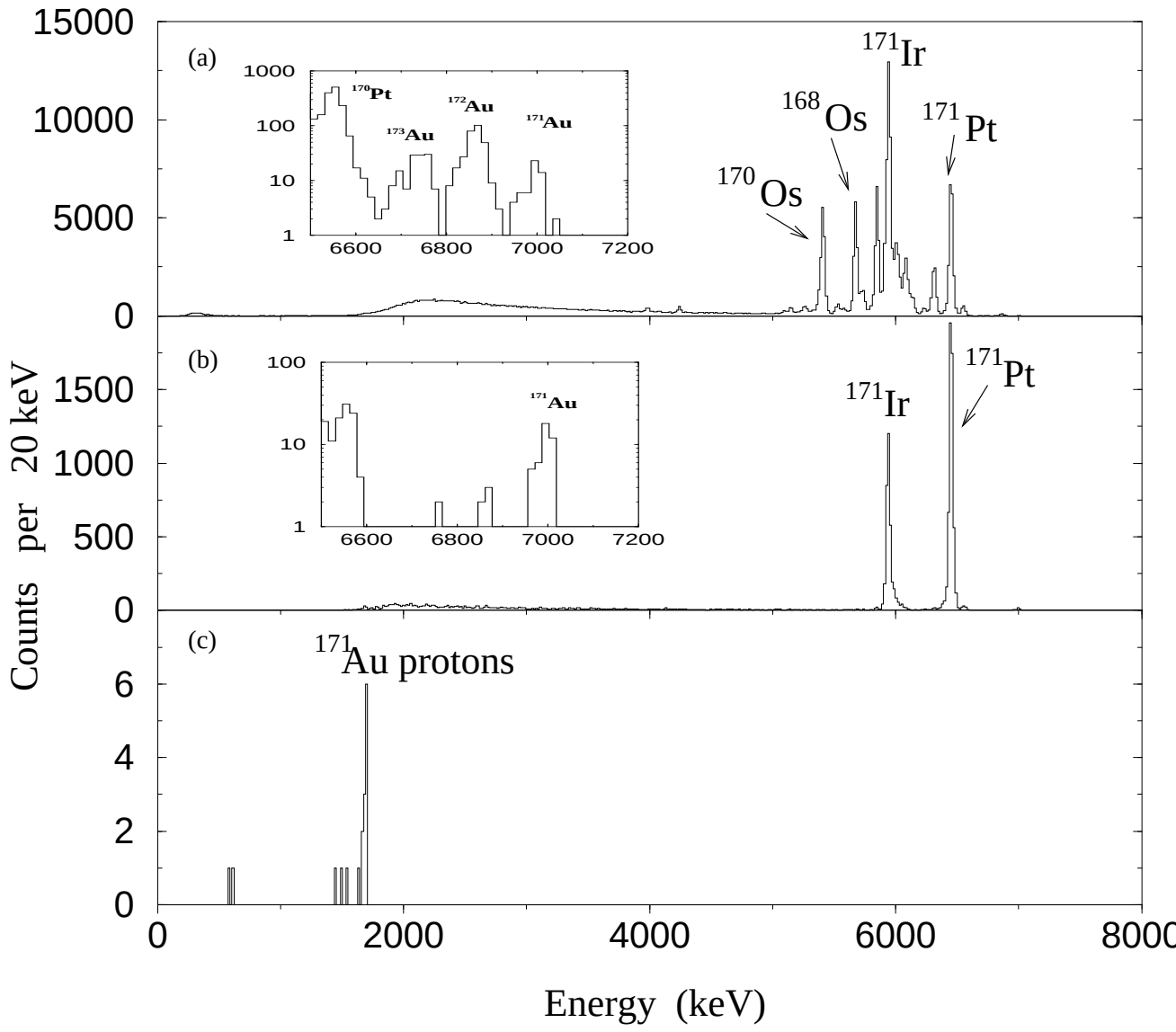

Figure 4.8: (a) Energy spectrum of all decay events in the reaction of 389 MeV ^{78}Kr ions on a ^{96}Ru target. Assignments for the strongest alpha lines have been made. The inset shows the weaker alpha lines between 6500 and 7200 MeV including the new alpha from ^{171}Au at 6996 $\pm$ 6 keV. (b) Decays occurring in the 100 ms after and in the same pixel as a mass 171 implantation event. (c) As (b) but with the additional requirement the a subsequent decay occurred in the same pixel within 100ms of the first one with an energy corresponding to the known alpha from ^{170}Pt.

^{171}Au.

4.2.2 Proton decay from ^{167}Ir

The second part of the experiment used the reaction

$$^{78}\mathrm{Kr}\,(420\ \mathrm{MeV})\ +\ ^{96}\mathrm{Ru}\,(400\ \mu\mathrm{g/cm}^2)\ \longrightarrow\ ^{174}\mathrm{Hg}^*$$

to produce ^{170}Au via the 1p3n evaporation channel. Fig 4.9(a) shows an energy spectrum of all decay events in the DSSD for this reaction. The inset shows a

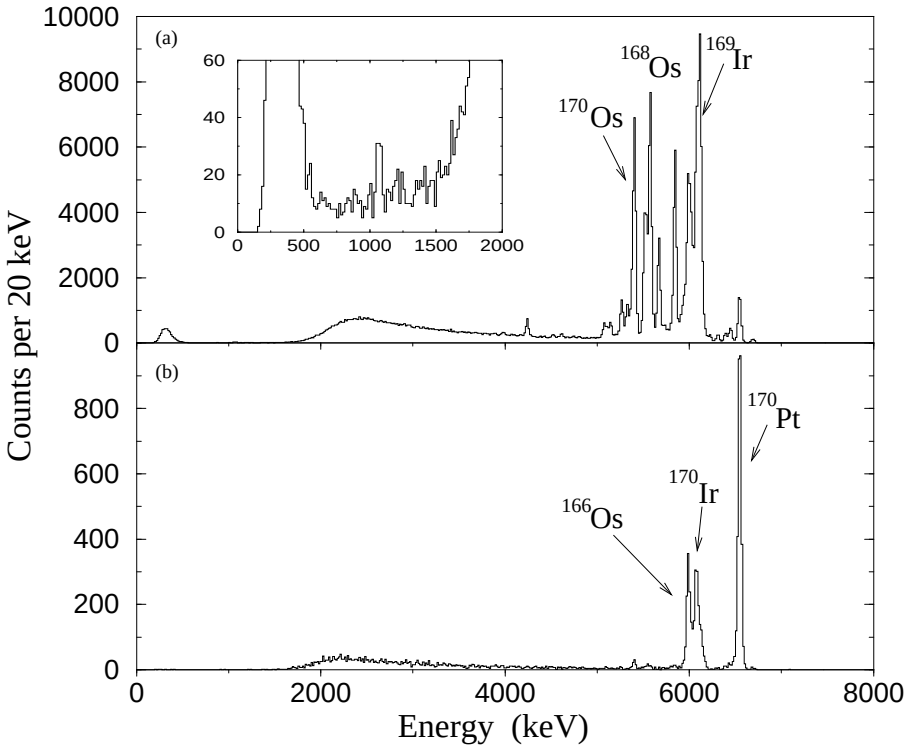

Figure 4.9: (a) Energy spectrum of all decays observed in the reaction of 420 MeV ^{78}Kr + ^{96}Ru. The inset shows a blown-up region of this spectrum between 0 and 2 MeV (b) Mass 170 decays with a 100 ms recoil-decay time gate.

blown up region of this spectrum between 0 and 2 MeV, revealing a low energy peak at around 1 MeV, which is too low in energy to be an alpha peak. However

this can not be attributed to the proton decay of ^{170}Au because the peak is not present in a mass 170 gated decay spectrum, as shown in figure 4.9(b). Indeed a spectrum of decay events correlated with a mass 170 implantation event and a subsequent ^{169}Pt alpha decay (the daughter of a ^{170}Au proton decay) within 100 ms, has no counts. No lines corresponding to the alpha decay of ^{170}Au were observed either.

Figure 4.10(b) shows an energy spectrum of decays correlated with mass 167 implantation events with a time gate of 100ms. The proton group is clearly visible as a small peak at the left side of the spectrum. It has an energy of 1066 $\pm$ 7 keV and clearly originates from implanted ions of mass 167. Figure 4.10(c) shows those decays with the above mass gate with the extra condition that a further decay occurred in the same pixel within 500ms, with an energy of 6000 keV, the known alpha decay energy of ^{166}Os. The obvious peak at 1066 $\pm$ 7 keV is identified as being from the proton decay of ^{167}Ir, produced in the reaction by the αp2n evaporation channel. The half-life of this peak was calculated as 38 $\pm$ 5 ms. A second group of four counts can be seen in this spectrum with an energy just higher ($\sim$ 1240 keV) than the main ^{167}Ir proton peak. This is suggestive of another proton decay from the same nucleus, but the evidence here is inconclusive.

4.2.3 Remeasurement of the proton lines from ^{171}Au and ^{167}Ir

Further experiments were carried out with the FMA at Argonne National Laboratory with the newer Edinburgh electronics to improve the measurements made on proton emission from ^{171}Au and ^{167}Ir, and to search for new proton radioactivities from ^{165}Ir and ^{166}Ir. The results are presented in [Dav97] and are summarised below.

Proton radioactivity from ^{171}Au was remeasured with the new electronics reducing recoil-decay deadtime to $\sim$ 30 μs. An improved energy measurement of

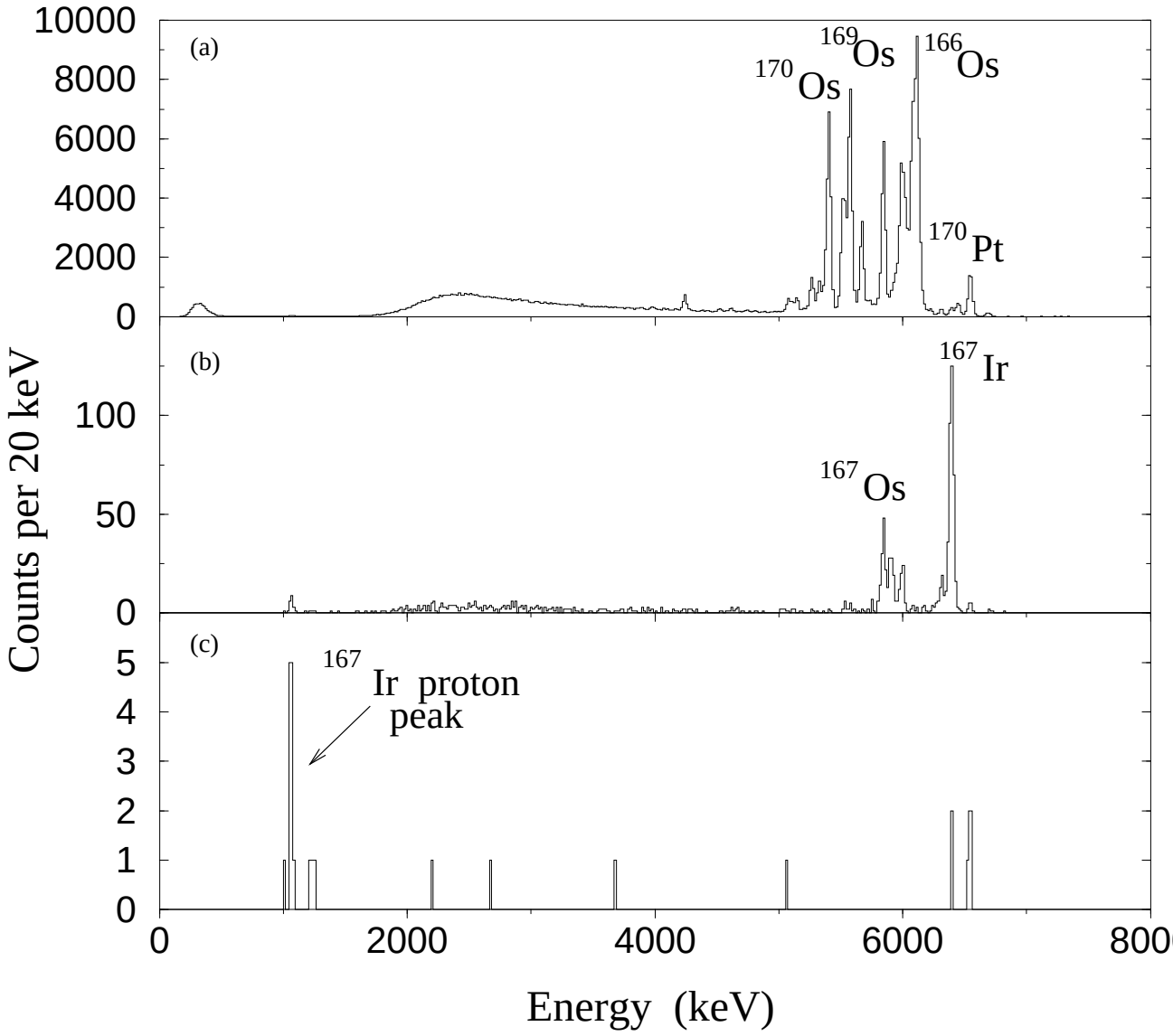

Figure 4.10: (a) All decays observed in the DSSD in the reaction of 420 MeV ^{78}Kr + ^{96}Ru. (b) Mass 167 decays with a 100ms time gate. (c) Same data as (b) with the additional condition that a second decay occurred in the same pixel within 500ms, with an energy of 6000 keV, the energy of the known alpha decay from ^{166}Os.

1692 ± 6 keV was made and the half-life was calculated as 1.02 ± 0.10 ms. The proton branching ratio was measured as 0.46 ± 0.04, yielding a proton partial half-life for the state of 2.22 ± 0.29 ms. The cross-section for production of ^{171}Au was 2 μb.

Proton emission from ^{167}Ir was remeasured using the reaction

$$^{78}\mathrm{Kr}\,(357\ \mathrm{MeV})\ +\ ^{92}\mathrm{Mo}\ \longrightarrow\ ^{170}\mathrm{Pt}$$

which produces ^{167}Ir via the 1p2n evaporation process rather than the α1p2n mechanism. Two lines at energies of 1064 ± 6 keV and 1238 ± 7 keV, with half-lives of 34.3 ± 2.2 ms and 34 ± 9 ms, respectively, were observed correlating with mass 167 implantation events and subsequent ^{166}Os alpha decays. This confirms the existence of a second weaker proton transition from ^{167}Ir. Two alpha lines associated with ^{167}Ir were observed, the known peak with an improved energy measurement of 6410 ± 5 keV and a previously unobserved weaker group with an energy of 6351 ± 5 keV. Their measured half-lives are 30.0 ± 0.6 ms and 39.7 ± 4.9 ms. One cannot determine which proton and alpha groups are associated with each state in ^{167}Ir on the basis of the measured half-lives because they are so similar. An alternative approach based on Q-value considerations, which is discussed in section 4.2.4, is required.

In the reaction of 384 MeV ^{78}Kr ions on a ^{92}Mo target two proton groups were observed from the decay of ^{166}Ir. The assignment was made on the basis of correlations with preceding mass 166 implantation events and the subsequent known alpha decays from ^{165}Os, at 6188 ± 7 keV. The energies of these lines are 1316 ± 8 keV and 1145 ± 8 keV, with half-lives of 11.4 ± 5.8 and 19 ± 9 ms, respectively. Two corresponding alpha groups associated with ^{166}Ir were observed with energies of 6561 ± 5 keV ($t_{1/2}$ = 15.2 ± 0.9 ms) and 6562 ± 6 keV ($t_{1/2}$ = 10.2 ± 2.2 ms). The former group is correlated with known alphas from ^{162}Re and ^{158}Ta. The latter is correlated with a previously unobserved alpha from ^{162}Re with energy 6086 ± 5 keV ($t_{1/2}$ = 107 ± 13 ms) and a known alpha group from

^{158}Ta.

In the same reaction, the proton decay of ^{165}Ir, produced via the p4n evaporation channel (the first time this channel has been successfully used), was identified by a correlation with a mass 165 implantation event (5 ms time gate) and with the subsequent 6321 keV alpha decay of ^{164}Os. One proton group was observed having an energy of 1707 $\pm$ 7 keV and a half-life of 0.29 $\pm$ 0.06 ms. Alpha decays from ^{165}Ir were also observed with an energy of 6715 $\pm$ 7 keV and a measured half-life of 0.39 $\pm$ 0.16 ms. Since both particles have a similar half-life, it is likely they come from the same state in the parent nucleus.

4.2.4 Assignments for ^{171}Au and ^{167}Ir protons

Table 4.4 shows the calculated values of the proton partial half-lives for the proton decays of ^{171}Au and ^{167}Ir along with the experimentally determined values.

From the table it is clear that the 1692 keV proton decay from ^{171}Au can best be interpreted as the l=5 decay of the $h_{11/2}$ state to the J=0 ground state of ^{170}Pt. Interpreting it as a decay from one of the other states would imply a large hindrance of 10^3-10^5 which is not expected in this region. Assuming proton decay from the $h_{11/2}$ state, the measured partial half-life is still about 5 times larger than the calculated value. This is discussed further in section 5.4.

Based on results from the decay of ^{167}Ir, we expect ^{171}Au to exhibit proton and alpha decay from a low-lying $s_{1/2}$ state. However this was not observed, implying the half-life of the state must be < 30 μs, the dead-time for detecting decays with our experimental set-up. The time-of-flight for recoil ions through the FMA is about 1 μs, so the decays of nuclei with half-lives between 1 and 30 μs remain unobserved but evidence of their existence is left in the DSSD, as the decay of the daughter nucleus correlated with an implanted ion of the parent's mass. In the case of proton decay from the $s_{1/2}$ state in ^{171}Au, this would mean ^{170}Pt alpha decays correlated with mass 171 implantation events. An excess of such events

Nuclide	E_p (keV)	Measured partial half-life(ms)	Proton Orbital	Calculated partial half-life
^{171}Au	1692(6)keV	2.22(29)	$s_{1/2}$	38 ns
			$d_{3/2}$	280 ns
			$h_{11/2}$	415 μs
^{167}Ir	1064(6) keV	110(15)	$s_{1/2}$	28.4 ms
			$d_{3/2}$	230 ms
			$h_{11/2}$	471 s
^{167}Ir	1238(7) keV	7500(1900)	$s_{1/2}$	162 μs
			$d_{3/2}$	230 ms
			$h_{11/2}$	2.47 s

Table 4.4: Comparison of measured partial proton decay half-lives for proton emitters ^{171}Au and ^{167}Ir with those calculated using a WKB approximation with the optical-model potential of Becchetti and Greenlees.

were observed over the background level due to random decays. This imposes a lower limit on the half-life of the $s_{1/2}$ state of 1 μs, ie. the decay occurs after the recoil has passed through the FMA.

Using these limits on the half-life in barrier penetration calculations, one can obtain upper and lower limits on the proton decay energy of 1.43 MeV and 1.59 MeV. This is below the 1.692 MeV observed for the decay of the $h_{11/2}$ state, so this state is identified as a metastable state in ^{171}Au with an excitation energy of 0.10-0.26 MeV (now measured at 0.249 MeV [Woo98]). The decay scheme deduced for ^{171}Au is shown in figure 4.11. The alpha decay from ^{171}Au is consistent with an unhindered Δl=0 transition between the $11/2^-$ in ^{171}Au and ^{167}Ir.

An alternative approach is required to determine the parent states of proton and alpha decays from ^{167}Ir, because the measured half-lives of the decays are so similar. Assignments can be made by examining Q value loops. The 6996

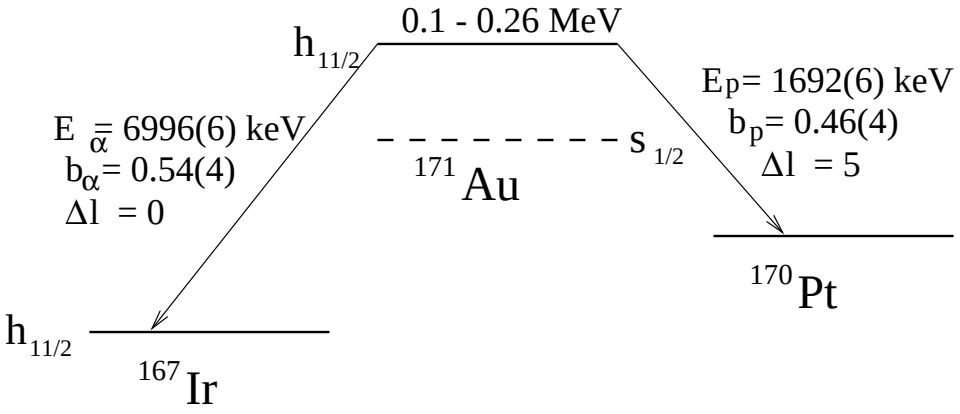

Figure 4.11: Decay scheme of ^{171}Au.

keV alpha from the $h_{11/2}$ state in ^{171}Au populates the $h_{11/2}$ state in ^{167}Ir, which emits the 6410 keV alpha (section 4.2.1). The proton from ^{171}Au is correlated with the 6550 keV alpha from ^{170}Pt. Using measured Q values, the decay energy for proton emission from the $h_{11/2}$ state in ^{167}Ta can be predicted, as shown in figure 4.12. The predicted Q value is 1246(11) keV which corresponds to a proton energy of 1239(11) keV, in good agreement with the higher energy proton line from ^{167}Ir at 1238(7) keV. Since the 6410(5) keV alpha line originates from the same state as the 1238(7) keV proton, the new 6351(5) keV alpha must be paired with the strong proton line at 1064(6) keV. The half-lives of the metastable $h_{11/2}$ and $s_{1/2}$ ground states can now be calculated as 30.0 $\pm$ 0.6 ms and 35.2 $\pm$ 2.0 ms, respectively. Proton branching ratios of 0.004 $\pm$ 0.001 and 0.32 $\pm$ 0.06 were deduced for these states.

From a comparison of the measured and calculated half-lives shown in table 4.4 indicates the 1064(6) keV proton line is best explained as the Δl=0 decay of the $s_{1/2}$ state ground state in ^{167}Ir, since the values calculated for the $d_{3/2}$ and $h_{11/2}$ levels are longer than the measured value. The 1238(7) keV line can only be explained as the Δl=5 decay from a isomeric $h_{11/2}$ state with an excitation energy of 175.3 $\pm$ 2.2 keV, calculated from the difference in proton peak centroids. The

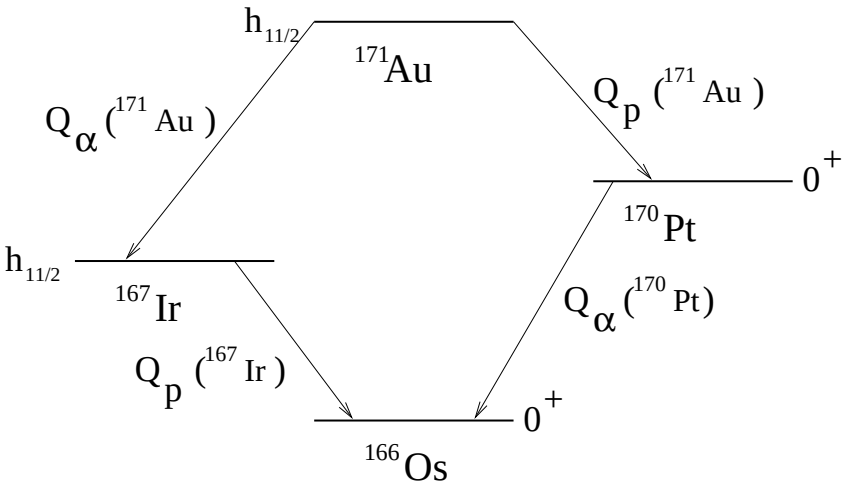

$$Q_p(^{167}\mathrm{Ir}) = Q_p(^{171}\mathrm{Au}) + Q_\alpha(^{170}\mathrm{Pt}) - Q_\alpha(^{171}\mathrm{Au})$$

Figure 4.12: Q value loop for decay involving $h_{11/2}$ states of ^{171}Au and ^{167}Ir.

decay scheme for ^{167}Ir is shown in figure 4.13. The reduced widths of both alpha transitions were consistent with unhindered Δl=0 decays, and therefore the 6410 keV line was assigned to an $11/2^- \longrightarrow 11/2^-$ transition and the 6351 keV line to an $1/2^+ \longrightarrow 1/2^+$ transition.

4.3 ^{141}Ho proton decay

Proton radioactivity in the region immediately below Z=69 is of particular interest since mass models, such as the Möller-Nix, predict these nuclei will have a high prolate deformation. A search was made at the Nuclear Structure Facility, Daresbury, for proton emission from isotopes with Z=61-67 [Liv93], including ^{142}Ho. No proton peaks above background were seen and an upper limit on the cross-section of 80nb for ^{142}Ho was inferred. It was concluded that the proton drip-line had not been crossed far enough for this decay mode to compete with

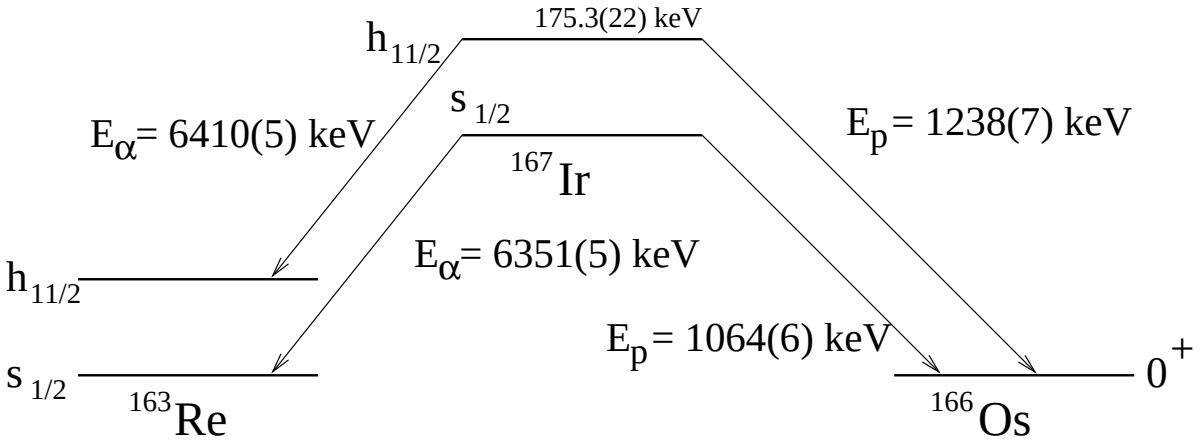

Figure 4.13: Decay scheme of ^{167}Ir

β^+-decay.

This section describes the search for proton emission from ^{141}Ho. There are no alpha decays in this region of the nuclear chart so positive identification of any decay is more difficult. Correlations can only be made to the preceding implanted ion and assignments are made using the mass information provided by this.

4.3.1 Experimental details

The detector set-up for this experiment was a 48×48 strip DSSD 40cm downstream of the focal plane with the BOX and Back Silicon detectors around it as detailed in section 3.4.5. This was necessary since much β-delayed proton activity is expected in this region and the continuum formed by this and any escape alphas (produced from contaminants in the target) would serve to hide any proton decay signals. The absence of daughter alpha decays to provide additional correlations needed to clean up spectra makes the use of these additional detectors even more important. During the setting-up period it was found that the beam was melting a hole in the stationary target, so in the main reaction the target frame was moved to offset the beam spot from the central target position and the target was rotated to disperse the deposited energy over a larger area.

Decay amplifiers with a lower threshold were used in this experiment since it was expected that the proton might have a low energy. A consequence of using these lower threshold amplifiers is that the overload recovery is poorer, allowing a maximum overload of only 2 times the maximum range of the decay amps (20 MeV) before a pedestal effect is seen, as mentioned in section 3.5.2. This compares with a figure of 4 times maximum overload for the standard decay amplifiers. A consequence of this is that a degrader foil had to be introduced in front of the DSSD to slow the recoils down to below 40 MeV. The degrader foil used was 1mg/cm^2 of aluminium.

Initially, a 285 MeV 2pnA beam of ^{54}Fe ions was used to bombard a 1mg/cm^2 ^{92}Mo target for a period of ∼13 hours to produce the compound nucleus ^{146}Er at a centre-of-target excitation energy of 76 MeV, calculated to maximise the yield of ^{141}Ho via the 1p4n evaporation channel. The excitation energy range covered within the target thickness was E_{ex} = 71-81 MeV. The FMA setting were M=141, Q=26 and E=81.5 MeV, and in this configuration, three charge states were passed (see figure 4.14) with no reduction in efficiency as was seen in the Re and Ta experiments. Later, the beam energy was increased to 305 MeV, with the hope that the yield of evaporation residues would increase. In fact, the count rate stayed approximately the same as the experiment continued for a further 9 hours. With this set-up the centre-of-target excitation energy was ∼88 MeV and the FMA was set up to transmit a mass 141 residue in charge state 27 with 87.4 MeV energy in its central trajectory.

4.3.2 Results on ^{141}Ho proton decay

Fig 4.15(a) is an energy spectrum of all decays in the DSSD for the reaction

$$^{54}\mathrm{Fe} + {}^{92}\mathrm{Mo} \longrightarrow {}^{146}\mathrm{Er}^{*} \xrightarrow{1p4n} {}^{141}\mathrm{Ho}$$

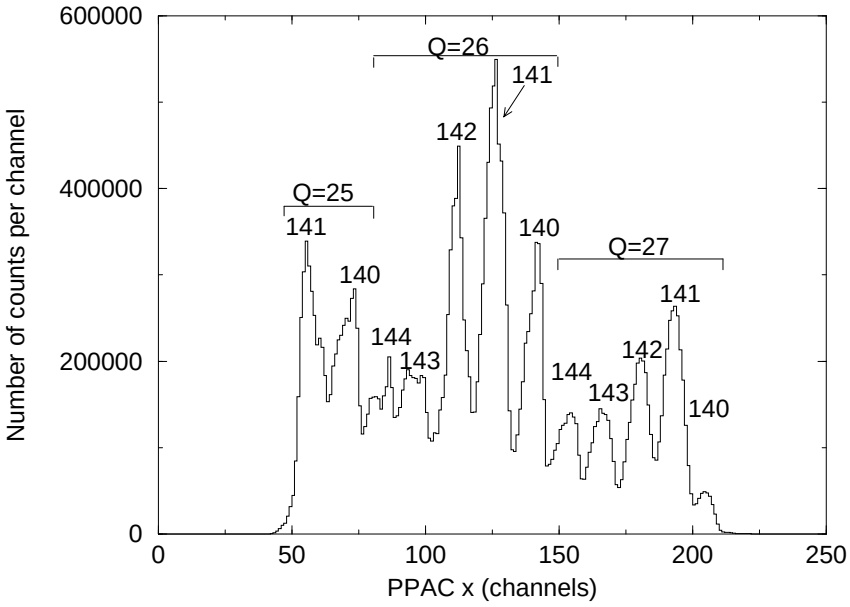

Figure 4.14: Focal plane x-position of recoil groups in the PPAC detector. Mass and charge states are indicated for each group.

with the BOX and Back Silicon detectors acting as vetos to eliminate as much β-delayed proton and escape-alpha background as possible. The two alphas at around 4 MeV, from ^{149}Tb and ^{150}Dy, are produced from beam reacting with heavier molybdenum isotopes present as contaminants in the target. The low energy background at around 500 keV is probably due to electronic pick-up. A low energy peak at around 1.2 MeV can be clearly seen in this spectrum. From energy considerations this cannot be an alpha decay. Applying a mass 141 gate with no time conditions to the data, as in figure (b), reduces the intensity of the alpha peaks without really affecting the lower energy peak. It does not entirely remove the alphas since most mass 141 implanted nuclei decay by beta emission which is largely undetected in the DSSD. The long-lived alphas (^{149}Tb $t_{1/2}$ = 4.1 hrs, ^{150}Dy $t_{1/2}$ = 7.2 min) then have a fair chance of randomly correlating with

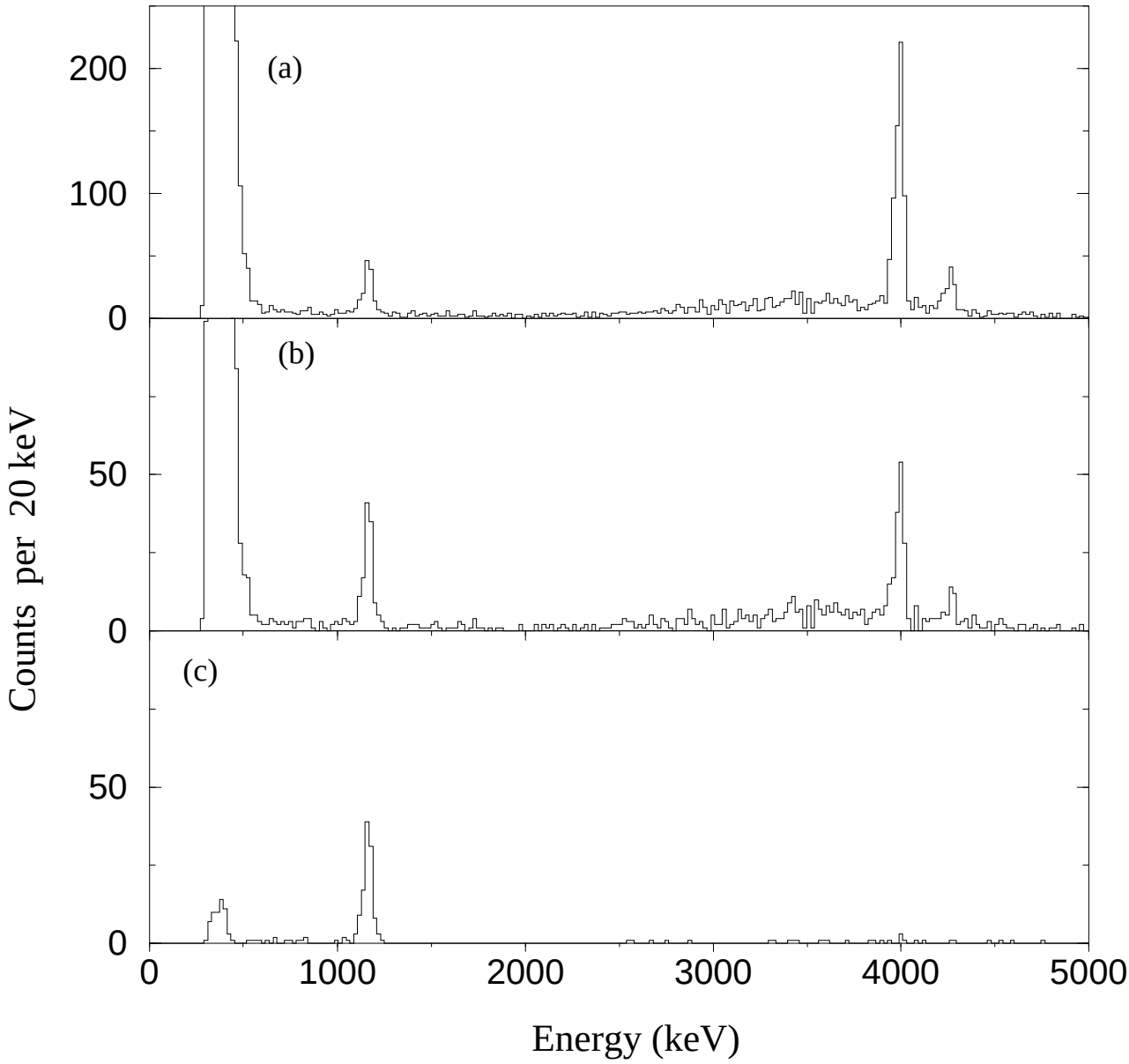

Figure 4.15: (a) Energy spectrum of decay events in the DSSD without corresponding BOX or Back Silicon detector signals. (b) Mass 141 gated spectrum with no recoil-decay time conditions. (c) Mass 141 gated spectrum with recoil-decay time < 100 ms.

the implanted ions. The application of a 100 ms recoil decay time gate to this spectrum as in figure 4.15(c) removes almost all the alphas and most of the β's. The proton peak remains unaffected, showing an unambiguous correlation with mass 141 implants.

The energy of the proton peak was measured as 1169 $\pm$ 8 keV, calibrated with respect to the ^{147}Tm protons and after the usual corrections for pulse height deficit and recoil contribution to pulse height were made, as detailed in table 4.5. The half-life of the transition is 4.2 $\pm$ 0.4 ms, calculated by the method of maximum likelihood. The cross-section for production of protons from ^{141}Ho was determined to be $\sim$200 nb.

Peak energy E_{PEAK}	1167.7 keV
Proton pulse height deficit PHD_p	3.0 keV
Recoil Energy E_R	8.4 keV
Recoil contribution to pulse height E_{RC}	1.7 $\pm$ 0.8 keV
Proton screening correction E_{sc}	12.5 keV
Proton energy E_p	1169 $\pm$ 8 keV
$Q_p = E_p + E_R$	1177 $\pm$ 8 keV
$Q_{p,nuc} = Q_p + E_{sc}$	1190 $\pm$ 8 keV

Table 4.5: Calculation of proton energy for ^{141}Ho.

The Q-value of 1.177 $\pm$ 0.008 MeV calculated for the decay is in good agreement with the prediction (1.15 MeV) of the Liran-Zeldes mass model, which is known to reproduce well proton decay Q-values in this region. Predictions for neighbouring A=141 isobars ^{141}Dy and ^{141}Tb suggest they are proton bound, and hence they were considered very unlikely to be the origin of the observed protons.

Table 4.6 shows the theoretical calculations of the half-life of ^{141}Ho using the same method used in this chapter for Re, Ta, Ir and Au. The half-life of ^{141}Ho is very short compared to the predicted β partial half-life of 0.27 s [Möl97a], imply-

ing a very small β branch ($\sim$ 1.6%), so the partial half-life has been approximated by the measured half-life. It is clear from a comparison of the figures in table 4.6

Nuclide	E_p (keV)	Measured partial half-life(ms)	Proton Orbital	Calculated partial half-life
^{141}Ho	1169 $\pm$ 8	4.2 $\pm$ 0.4 ms	$s_{1/2}$	1 μs
			$d_{3/2}$	10 μs
			$h_{11/2}$	37 ms

Table 4.6: Calculated proton partial half-lives for proton emission from the $s_{1/2}$, $d_{3/2}$ and $h_{11/2}$ levels in ^{141}Ho.

that proton decay from ^{141}Ho is not well described by a simple barrier penetration model; decays from the $s_{1/2}$ of $d_{3/2}$ levels would require hinderances of $\sim$500 and $\sim$4000, respectively, and the calculated value for the $h_{11/2}$ orbital is clearly too long. Since the major assumption in these calculations is a spherical nucleus, the failure of the theoretical predictions in reproducing the observed half-life is strongly indicative of a deformed nucleus, as predicted by the macroscopic-microscopic mass model of Möller *et al.* [Möl95]. A half-life calculation which includes the effects of deformation is discussed in the following chapter.

4.4 Other experiments at ANL

Other recent experiments at Argonne have succeeded in identifying proton emission from an excited state in ^{185}Bi [Dav96] and from the ground state and an excited state in ^{177}Tl. The former represents the heaviest proton emitter observed to date and is of particular interest since ^{185}Bi has a single proton outside the Z=82 closed shell, and represents the first proton radioactivity measurement in this region of the nuclear chart.

Because competition from fission is high for nuclei produced at high angular

momentum, ^{185}Bi was produced via the 1p1n evaporation channel using the relatively cold compound nucleus reaction ^{92}Mo + ^{95}Mo $\longrightarrow$ ^{187}Po at excitation energies between 25 and 30 MeV. A proton line having an energy of 1594 $\pm$ 9 keV and a half-life of 44 $\pm$ 16 μs was observed and assigned to ^{185}Bi on the basis of correlations with a preceding implanted ion of mass 185 and the subsequent ^{184}Pb alpha decay. The origin of this fast decay was concluded to be a low-lying intruder state in ^{185}Bi. Details can be found in the original paper [Dav96].

In another experiment, Poli et al. [Pol98], using the ^{78}Kr + ^{102}Pd reaction at 370 MeV, observed two proton groups from ^{177}Tl with energies and half-lives of 1918 $\pm$ 10 keV (241(32) μs) and 1178 $\pm$ 19 keV (24(7) ms). Two corresponding alphas were observed also. Both proton groups were correlated with known alphas from ^{176}Hg and ^{172}Pt. The low energy proton group has been interpreted as the decay of the $1/2^+$ ground state of ^{177}Tl with a proton branching ratio of 0.2. The other proton line is assigned to an isomer at 744(21) keV excitation energy.

4.5 Summary of Experimental Results

Tables 4.7 and 4.8 give a summary of new transitions measured in proton radioactivity experiments using the FMA at Argonne National Laboratory. At least 13 new proton transitions and six new alpha transitions have been discovered. These provide a wealth of spectroscopic information, which is discussed in the following chapter.

Nucleus	Beam+Target	Cross-section	Energy(keV)	Half-life(ms)
^{157}Ta	270 MeV ^{58}Ni + ^{102}Pd	20 nb	927 ± 7	10.1 ± 0.4
^{161}Re	270 MeV ^{58}Ni + ^{106}Cd	150 nb	1192 ± 6	0.37 ± 0.04
^{161m}Re	”	150 nb	1315 ± 7	16 ± 1
^{141}Ho	285 MeV ^{54}Fe + ^{92}Mo	200 nb	1169 ± 8	4.2 ± 0.4
^{171}Au	389 MeV ^{78}Kr + ^{96}Ru	2 μb	1692 ± 6	1.02 ±0.10
^{165}Ir	384 MeV ^{78}Kr + ^{92}Mo	200 nb	1707 ± 7	0.30 ± 0.06
^{166}Ir	”	300 nb	1145 ± 8	10.5± 2.2
^{166m}Ir	”	6 μb	1316 ± 8	15.1 ± 0.9
^{167}Ir	357 MeV ^{78}Kr + ^{92}Mo	10 μb	1064 ± 6	35.2 ± 2.0
^{167m}Ir	”	100 μb	1238 ± 5	30.0 ± 0.6
^{185m}Bi	410 MeV ^{92}Mo + ^{95}Mo	100 nb	1585 ± 9	0.044 ± 0.016
^{177}Tl	370 MeV ^{78}Kr + ^{102}Pd	–	1178 ± 19	24 ± 7
^{177m}Tl	”	–	1918 ± 10	0.241 ± 32

Table 4.7: New proton emitters identified at Argonne National Lab

Parent nucleus	Alpha particle energy (keV)	Half-life (ms)
^{157}Ta	6117 ± 4	10.4 ± 0.4
^{167}Ir	6351 ± 5	35.2 ± 2.0
^{163}Re	5870 ± 5	390 ± 72
^{166}Ir	6562 ± 6	10.5 ± 2.2
^{162}Re	6086 ± 5	107 ± 13
^{165}Ir	6715 ± 7	0.39 ± 0.16

Table 4.8: New alpha decays identified at Argonne

Chapter 5

Discussion

The proton emitters presented in the previous chapter along with those studied at GSI and Daresbury complete a continuous chain of odd-Z proton emitting nuclei from Z=67-83. This wealth of new information on a diverse range of nuclei, from those expected to be highly deformed to ones described well by a spherical model of the nucleus, allows us to develop our understanding of the proton decay mechanism and the nuclear structure at the proton drip-line.

5.1 Spectroscopic factors for spherical nuclei

Proton-decaying nuclei in the region above Z=68 have been shown to be reasonably well described by a spherical model of the nucleus and half-life predictions using such an approach are sufficiently accurate to assign protons to particular orbitals in parent nuclei. However, some predicted half-lives in this region are up to an order of magnitude greater than the measured values, and a more rigorous treatment of proton decay must include nuclear structure effects, which are described by the use of the spectroscopic factor, as described in section 2.4.

The spherical half-life predictions calculated using the WKB approximation are compared to experimentally measured values in columns two and three of

Nuclide	$t_{1/2,p}^{calc}$	$t_{1/2,p}^{exp}$	S^{calc}	S^{exp}
^{157}Ta	167 ms	300 ± 110 ms	0.56	0.56 ± 0.21
^{161g}Re	0.142 ms	0.37 ± 0.04 ms	0.44	0.38 ± 0.04
^{161m}Re	107 ms	325 ± 44 ms	0.44	0.33 ± 0.05
^{171}Au	0.415 ms	2.22 ± 0.29 ms	0.22	0.19 ± 0.03
^{167g}Ir	28.4 ms	110 ± 15 ms	0.33	0.26 ± 0.07
^{167m}Ir	2.47 s	7.5 ± 1.9 s	0.33	0.33 ± 0.11

Table 5.1: Spectroscopic factors for proton decaying states in ^{157}Ta, ^{161}Re, ^{171}Au and ^{167}Ir

table 5.1 for proton decaying states in ^{157}Ta, ^{161}Re, ^{166,167}Ir and ^{171}Au. The table also compares the experimental spectroscopic factors with those calculated in the '$p/9$' formalism presented in section 2.4. The agreement is remarkable considering the simplicity of the model. Application of this method to all the known proton emitters in the region $65 \leq Z \leq 81$ yields the results shown in figure 5.1. The straight line shows the S(p)=p/9 prediction of the model and the experimental data points confirm that spectroscopic factors do increase toward unity as Z approaches 64. The points showing the largest disagreement with the model are all protons decaying from the $d_{3/2}$ orbital. The large error bars on the data points for the lighter proton emitters reflect large uncertainties in the beta branches for these nuclei.

Table 5.2 compares proton decay half-lives calculated by the DWBA method [Åbe97] (see section 2.3.1) with experimental values for the same nuclei. Experimental spectroscopic factors S^{exp} are compared to those obtained in BCS theory. Again, agreement is good for these odd-even nuclei. Åberg's paper [Åbe97] gives results for all proton emitters discovered so far except ^{141}Ho. The odd-odd proton emitters show generally poorer agreement with theory, especially in the cases of ^{112}Cs(which is expected to be deformed), ^{160}Re and ^{166}Ir. The discrepancy in the

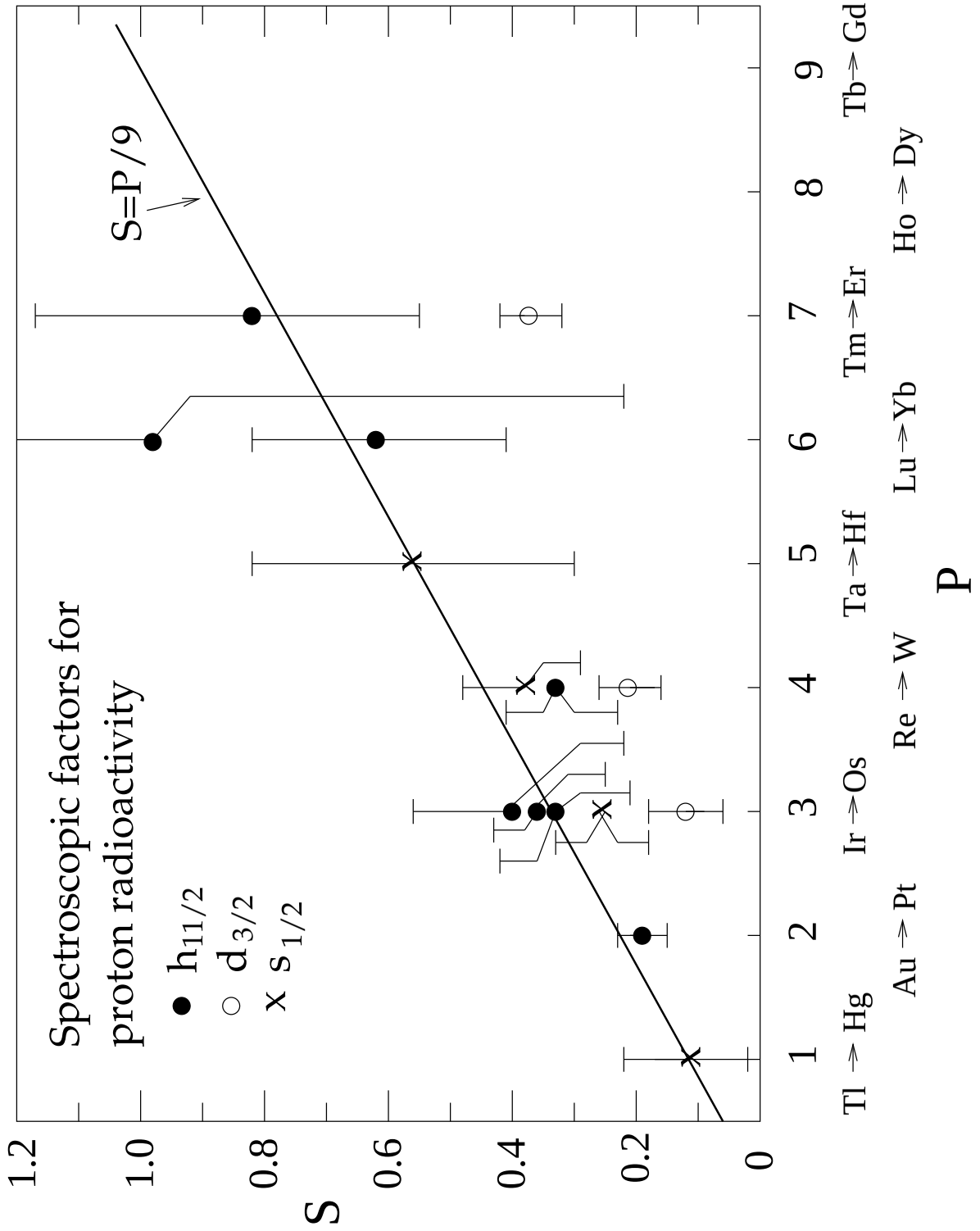

Figure 5.1: Spectroscopic factors for proton emitters with $65 \leq Z \leq 82$.

Nuclide	$t_{1/2,p}^{exp}$	$t_{1/2,p}^{th}$	S^{exp}	S^{th}
^{157}Ta	300±110 ms	220±60 ms	0.74±0.34	0.66
^{161g}Re	0.37±0.04 ms	0.19±0.03 ms	0.51±0.10	0.59
^{161m}Re	325±44 ms	86±14 ms	0.27 ±0.06	0.33
^{171}Au	2.22±0.29 ms	0.35±0.04 ms	0.16±0.03	0.14
^{167g}Ir	110±15 ms	36±7 ms	0.33±0.08	0.51
^{167m}Ir	7.5±1.9 ms	2.0±0.4 ms	0.27±0.09	0.23

Table 5.2: Comparison of experimental and theoretical half-lives and spectroscopic factors using DWBA calculations and BCS theory [Åbe97].

latter two might be due to the residual np interaction mixing the $\pi d_{3/2}\nu f_{7/2}$ and $\pi s_{1/2}\nu f_{7/2}$ configurations, hence reducing single particle strengths .

5.2 Proton Decay of Deformed Nuclei

The comparison, presented in section 4.4.2, of WKB half-life predictions with the experimentally measured value for ^{141}Ho clearly suggests this nucleus is not well described by the simple spherical shell model. This is in accordance with the calculations of Möller *et al.*[Mol95], which predict ^{141}Ho to be in a region of high prolate deformation compared to the proton emitters described above, which are predicted to be approximately spherical or just modestly deformed.

Figure 5.2 shows a plot of the quadrupole deformation parameter β_2 against proton and neutron number as calculated in this model. The stable isotopes are shown as black squares and the expected position of the proton drip-line as calculated from the mass tables of Comay, Kelson and Zidon [Com88] is shown by the black line. The examples of proton radioactivity to date are indicated by the black circles, except ^{141}Ho, represented by a white circle. Above Z=67, all proton emitters have a relatively modest deformation ($\beta_2 < 0.15$) while ^{141}Ho has a β_2

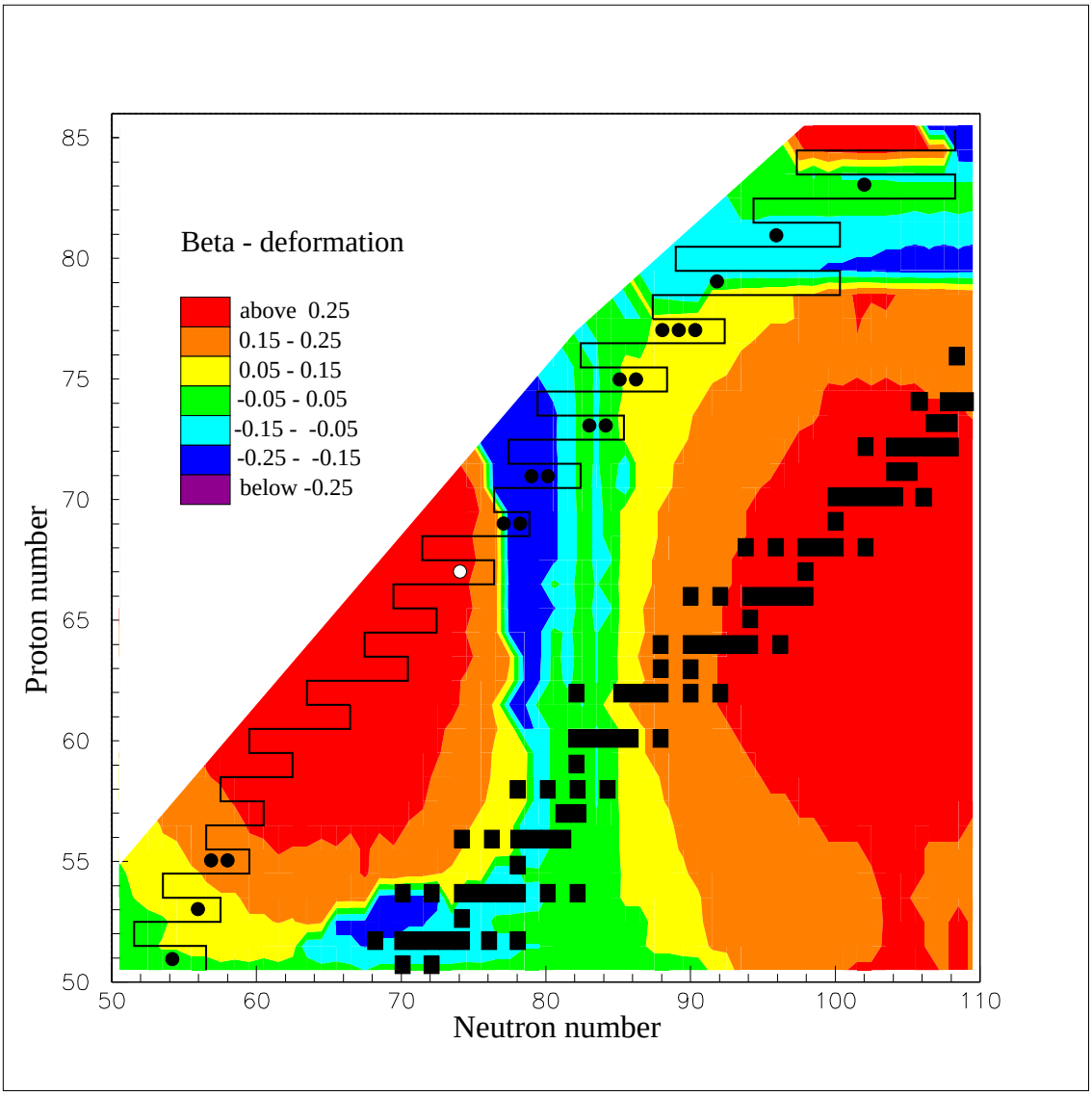

Figure 5.2: Plot of quadrupole β deformation parameter β_2 versus proton and neutron number.

value of 0.29. The model predicts an extremely rapid transition between mildly oblate and highly prolate deformation between Tm and Ho isotopes. Therefore one might expect that the simple spherical one-particle barrier penetration model does not work as well for ^{141}Ho as for the heavier proton emitters.

Figure 5.3 shows the Nilsson one-particle proton levels calculated for ^{141}Ho by Möller [Möl97b] as a function of deformation parameter ϵ_2 (relationship between ϵ_2 and β_2 given in sect. 2.4.1), which is predicted to be 0.26 for ^{141}Ho. For the region $0.2 \leq \epsilon_2 \leq 0.3$, indicated by the vertical dashed lines in the diagram, the outermost proton of ^{141}Ho (Z=67) can be determined to be in the $7/2^-[523]$ orbital by counting pairs of protons into the levels above Z=56, although the $1/2^+[411]$ state is predicted to be close to it in energy and therefore must be considered as a candidate level too. The ground state spin and parity of ^{141}Ho are given as $7/2^-$ by Möller, Nix and Kratz [Möl97a] in their table of nuclear properties derived from the finite-range droplet model [Möl95], described in section 2.4.1.

The multiparticle theory of Kadmensky and Burgov[Kad95], described in section 2.3.1, provides a method of calculating half-lives of deformed nuclei, and has produced predictions in reasonable agreement with experiment for deformed nuclei ^{109}I and ^{113}Cs [Bug89, Bog90]. Proton decay rates for these nuclei were not well reproduced using the simple barrier penetration model. A calculation using the multiparticle theory has been performed [Dav97b] to predict the proton partial half-life of ^{141}Ho, using β_2 values between 0.25 and 0.35, and neglecting the effects of pairing in the daughter wavefunction. Half-lives were calculated assuming the proton occupied the $7/2^-[523]$ and $1/2^+[411]$ Nilsson orbitals. The latter was discounted because it gave a prediction of ~ 15 μs for the half-life. The $7/2^-[523]$ calculations are shown in figure 5.4 and are consistent with the measured half-life of 4.2 ± 0.4 ms over the range of β_2 values from around 0.27 to 0.33.

Thus the seemingly anomalous decay rate of ^{141}Ho can be explained as an effect of deformation. The remarkable agreement of the quadrupole deformation

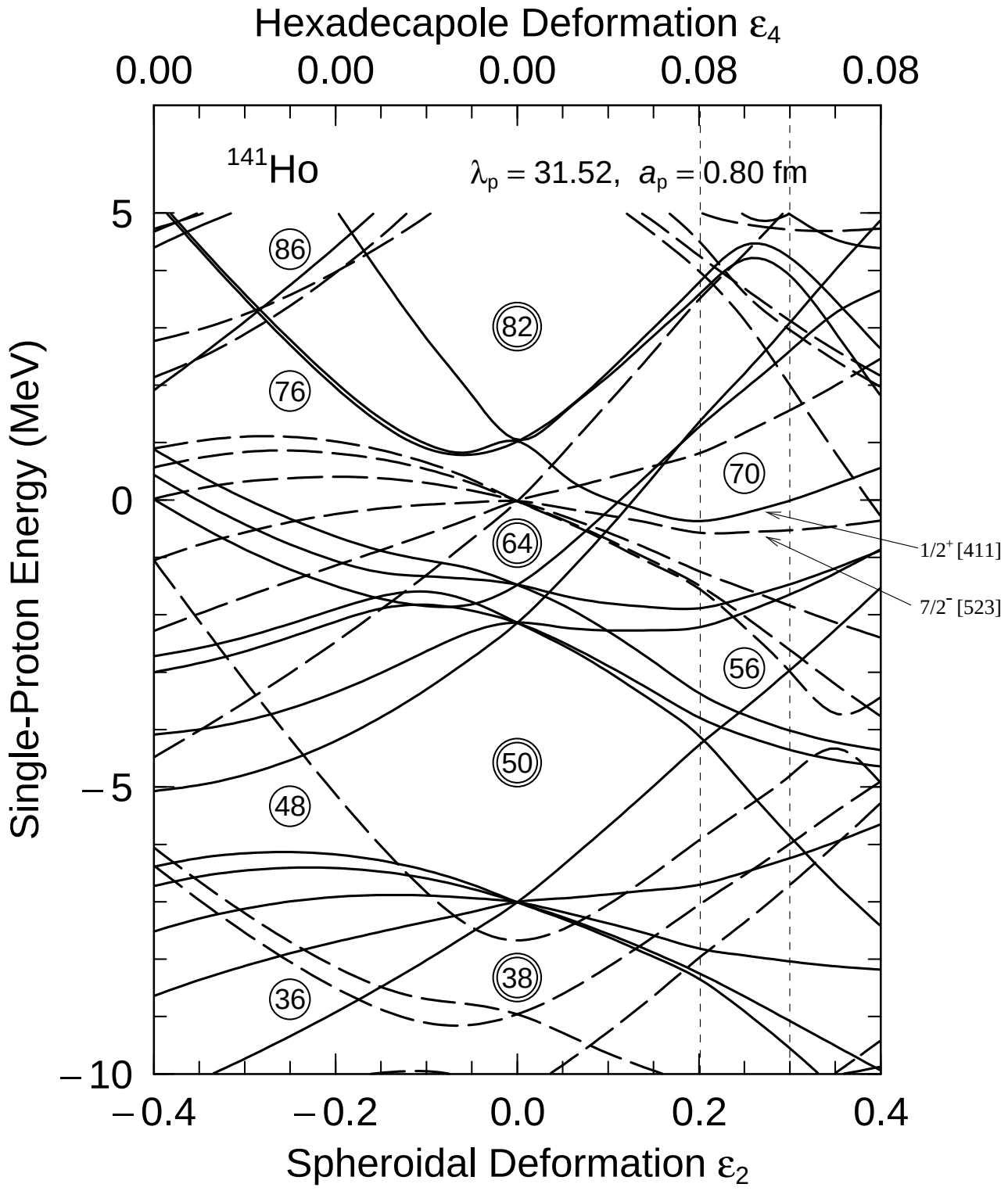

Figure 5.3: Single proton energy levels as a function of deformation for ^{141}Ho calculated by Möller [Mol97b].

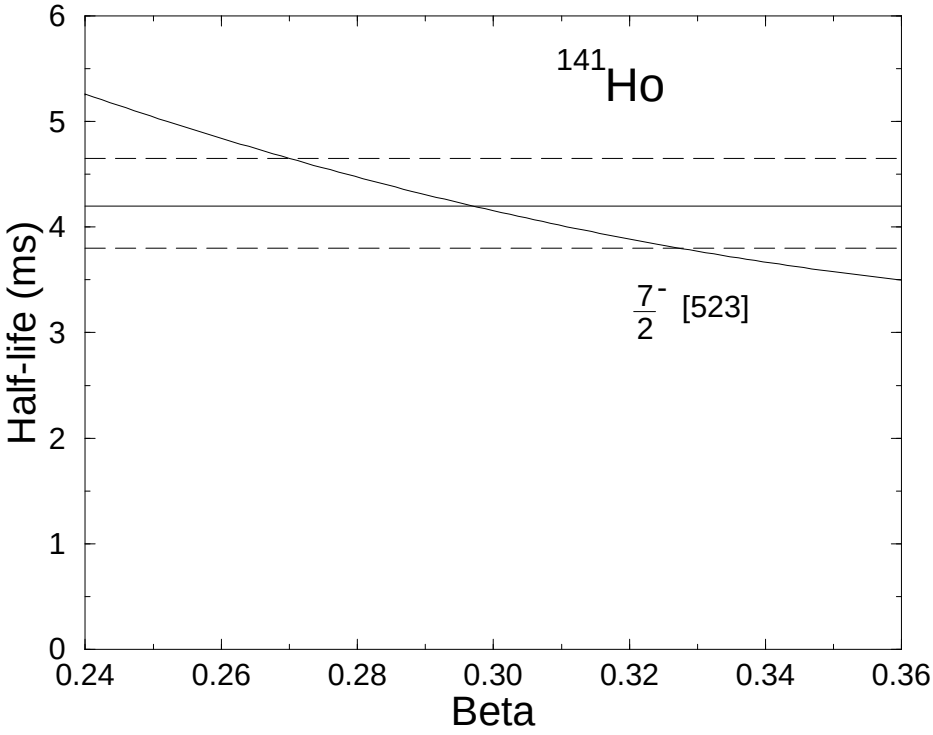

Figure 5.4: Calculated proton decay half-life for ^{141}Ho based on the $7/2^-[523]$ Nilsson orbital. The observed half-life is between the values indicated by the dashed lines.

predicted using the multiparticle theory with that predicted by the macroscopic-microscopic model gives strong support to the validity of using a deformation-dependent model of proton decay in this region.

5.3 Q_p value predictions and mass models

As discussed in section 4.1.5, Q value loops can be exploited to provide predictions of proton separation energies for nuclei from which proton decay has not been observed. Given proton and alpha decay energies of a state in a nucleus and the alpha decay energy of the proton daughter, one can calculate the proton decay

Q value for the analogous state in the alpha daughter nucleus. Energies of 604 ± 10 keV and 684 ± 9 keV were predicted for the $h_{11/2}$ and $s_{1/2}$ states in ^{153}Lu. Assignment of the 1238 ± 7 keV line from ^{167}Ir to the $h_{11/2}$ state was made on the basis of the Q_p prediction provided by the proton and alpha decays from the $h_{11/2}$ state in ^{171}Au.

Figure 5.5 shows the alpha decay chains following the decay of ^{167}Ir and the calculated Q values for proton decay from the $h_{11/2}$ and $s_{1/2}$ states in the daughter nuclei. There are two alpha decay chains, starting with the Q_α=6567(5) and 6507(5) keV decays from ^{167}Ir, both being consistent with $\Delta l = 0$ transitions, which connect the $h_{11/2}$ and $s_{1/2}$ states in the chains, respectively. A full discussion of the decay chain can be found in [Dav97a]. It should be noted that only the protons from ^{167}Ir have been observed. Proton decays from ^{163}Re, ^{159}Ta and ^{155}Lu have energies consistent with partial half-lives too long to be experimentally observed, as shown in table 5.3. ^{151}Lu has negative Q_p values for both states, i.e., they are bound to proton decay.

Nuclide	Proton Orbital	Q_p (keV)	Predicted partial half-life
^{163m}Re	$h_{11/2}$	826 ± 10	$\sim$ 3 Ms
^{163}Re	$s_{1/2}$	712 ± 9	$\sim$ 70 ks
^{159m}Ta	$h_{11/2}$	438 ± 12	$\sim 10^{18}$ s
^{159}Ta	$s_{1/2}$	376 ± 11	$\sim 10^{17}$ s
^{155m}Lu	$s_{1/2}$	120 ± 12	$\gg 10^{40}$ s
^{155}Lu	$h_{11/2}$	99 ± 13	$\gg 10^{40}$ s

Table 5.3: Predicted proton partial half-lives for ^{163}Re, ^{159}Ta and ^{155}Lu using Q_p values in figure 5.5.

In a similar way, measurement of the proton decays from ^{165,166}Ir and ^{177}Tl

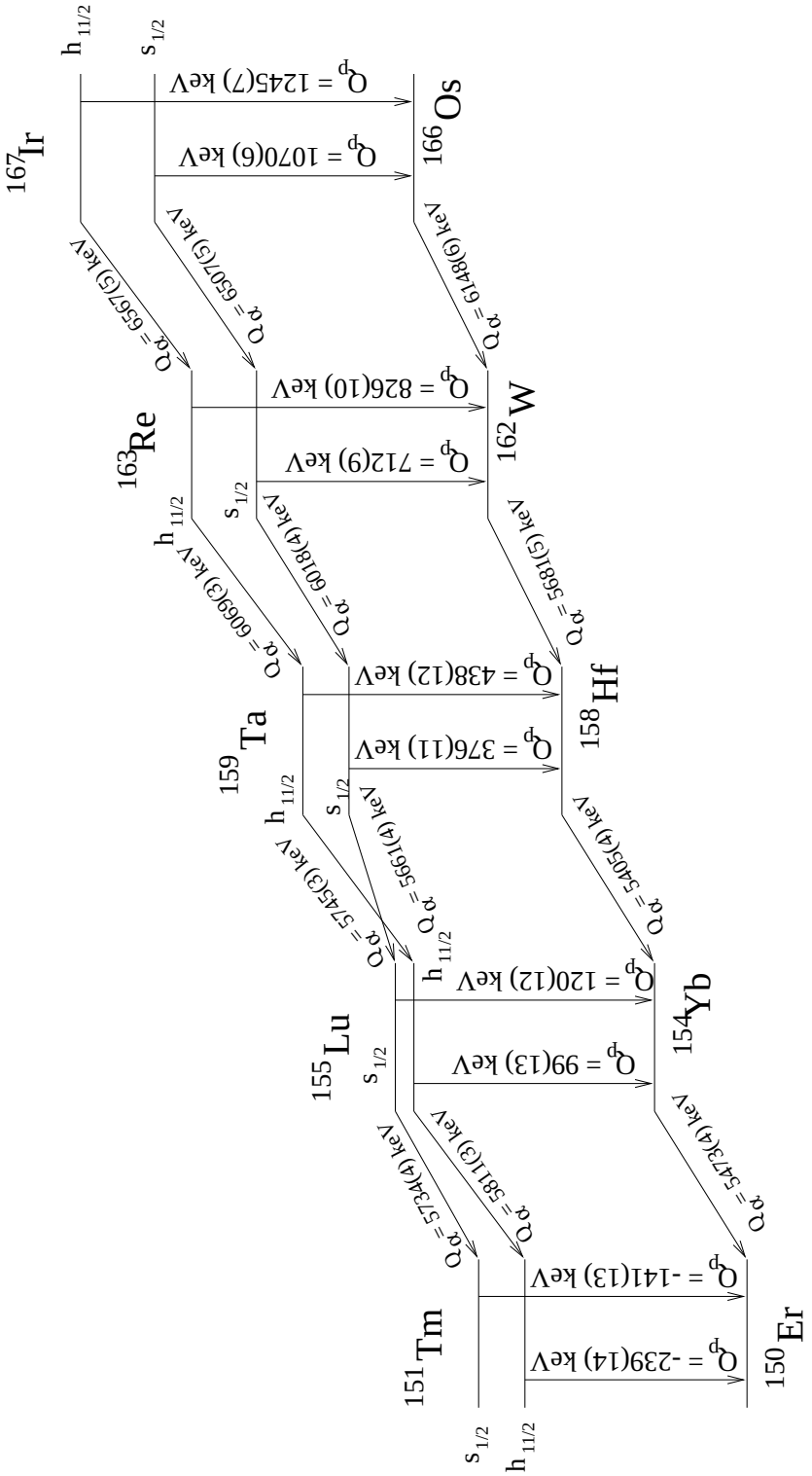

Figure 5.5: Decay cascade from ^{167}Ir used to calculate Q_p values.

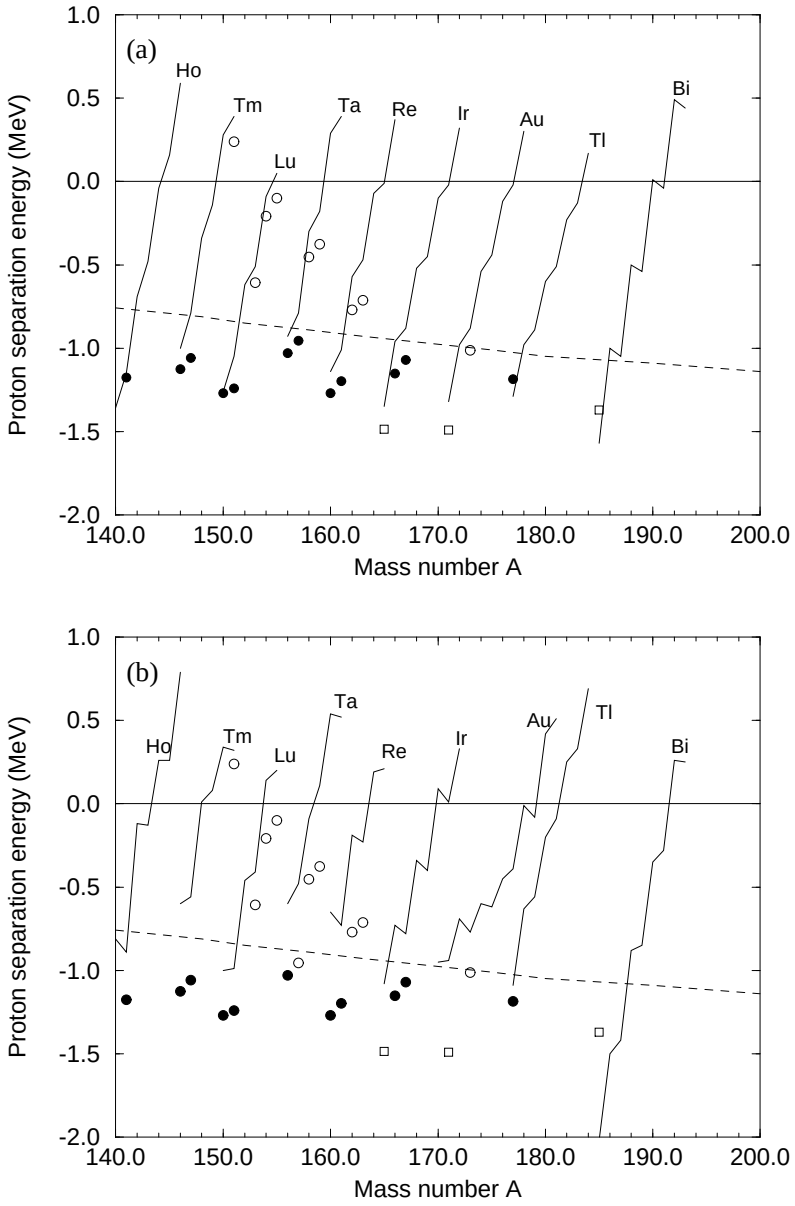

Figure 5.6: (a)Measured and derived proton separation energies for ground state proton emitters compared to the predictions of Liran and Zeldes [Lir76]. Filled circles represent measurements of ground state proton radioactivity, open circles denote those calculated from Q value loops and squares are predictions using estimations of excitation energies.(b) As (a) but with the predictions of Möller et al.[Mol95]

allow the calculation of Q_p values for states in ^{161,162}Re, ^{157,158}Ta, ^{153,154}Lu and ^{173}Au. Figure 5.6(a) shows a plot of measured and derived proton separation energies for ground state proton emitters of the odd-Z elements from Ho(Z=67) to Bi(Z=83), compared to the predictions of the mass model of Liran and Zeldes [Lir76], which are represented by the solid lines. The filled circles represent measurements of ground state proton decay. The squares are predictions of the ground state proton energies based on observed proton decays from excited states and estimates of the excitation energies of those states. The open circles denote the ground state proton energies calculated from Q value loops for nuclei which are the daughters of the proton emitters ^{177}Tl, ^{167}Ir, ^{166}Ir and ^{157}Ta. The dashed line represents the experimental limit for observation of the proton decays in this region; proton emitters with separation energies above this line will have half-lives $>$ 1s. Figure 5.6(b) shows the same data compared the the predictions of Möller et al. [Möl95].

From figure 5.6 it can be seen that the Liran-Zeldes mass models predicts the proton separation energies remarkably well, although an overestimation of the proton binding of about 200 keV is evident for most of the nuclei. The mass model of Möller at al. predicts the values rather less well, with the overestimation being about 500 keV. The most striking difference between the predictions of the two models is the Möller-Nix giving a strong odd-even staggering effect reflecting a stronger interaction between the unpaired proton and neutron. As mentioned in the original paper [Lir76], the Liran-Zeldes model is relatively insensitive to local structure effects and tends to smooth out any slope discontinuities in the experimental data. Nevertheless, both models give reasonably good predictions for the proton separation energies of the nuclei observed at GSI and Daresbury. The success of the Liran-Zeldes model in predicting proton decay Q-values is outstanding considering it was devised before the first example of proton radioactivity was discovered and therefore does not incorporate any proton decay measurements

into its database.

5.4 Mass excesses derived from the proton and alpha decays of ^{167}Ir

Additional information, in the area of mass excesses, can be obtained from these experiments if one of the nuclei on a decay chain has a known mass. A recent measurement of the mass excess of the 2^- state in ^{150}Ho as -61950(27) keV using the ISOLTRAP facility [Bec96] provides us with a starting point since the the Q value for electron capture from ^{150}Er to the 2^- state in ^{150}Ho has been measured to be 4108(5) keV [Aud93]. This gives a value of -57842 keV for the mass excess of ^{150}Er. Using the Q_α values in figure 5.5, the mass excesses of ^{154}Yb, ^{158}Hf, ^{162}W and ^{166}Os, the alpha decay parents of ^{150}Er can be calculated. These are listed in table 5.4, along with the mass excesses of ^{171m}Au and ^{167}Ir, obtained from their proton decay Q values. The mass excesses of the nuclei alpha decay chain terminating at ^{151}Tm can also be calculated using the known alpha decay Q values given in figure 5.8. These are also shown in table 5.4 as well as the results of the systematic predictions of the 1995 update to the Atomic Mass Evaluation (AME95)[Aud95]. The differences between the experimental mass excesses and those of AME95 show a smooth increase moving further from the line of β stability.

Nuclide	Mass Excess (keV)	Systematic Prediction(keV)	Difference(keV)
^{150}Er	-57842(31)	-59970(100)	128(105)
^{154}Yb	-49943(31)	-50080(100)	137(105)
^{158}Hf	-42112(31)	-42250(100)	138(105)
^{162}W	-34006(32)	-34150(100)	144(105)
^{166}Os	-25433(32)	-25590(100)	157(105)
^{170}Pt	-16300(33)	-16460(100)	160(105)
^{171}Au($s_{1/2}$)	-7529(115)	-7660(250)	131(275)
^{167}Ir($s_{1/2}$)	-17074(33)	17190(100)	116(105)
^{163}Re($s_{1/2}$)	-26006(33)	-26110(110)	104(115)
^{159}Ta($s_{1/2}$)	-34449(33)	-34550(120)	101(124)
^{155}Lu($s_{1/2}$)	-42555(34)	-42630(130)	75(134)
^{151}Tm($s_{1/2}$)	-50791(34)	-50830(140)	39(144)

Table 5.4: Calculated mass excesses for nuclei in the two decay chains from ^{161}Ir and for ^{171}Au compared to those predicted from systematics [Aud95].

Chapter 6

Conclusion

6.1 Summary

The experiments described in this thesis were carried out at Argonne National Laboratory using the Fragment Mass Analyser in conjunction with a double-sided silicon strip detector. This continued the work done at the Daresbury Recoil Mass Separator (RMS) in mapping the proton drip-line beyond Z=50. The experiments were greatly aided by the range of energies and variety of beam species available from the ATLAS accelerator. The high transmission of the FMA ($\sim$ 15 %) compared to the RMS ($\sim$ 3 %) increased the sensitivity of the experiments to nuclei with smaller production cross-sections.

A series of experiments were performed and thirteen new proton transitions have been observed, including ones from ^{141}Ho, ^{157}Ta, ^{161}Re, ^{167}Ir and ^{171}Au, the analysis of which forms the major part of this work. The proton drip-line has now been mapped for a continuous chain of odd-Z isotopes from Z=67-83, as shown in figure 6.1. The red squares represent nuclides from which a proton branch has been directly observed, the yellow squares denote nuclides which alpha decay and the pink squares are those which beta decay only. Measurement of the decays from the odd-even nuclei ^{157}Ta, ^{161}Re, ^{167}Ir and ^{171}Au has provided valuable information

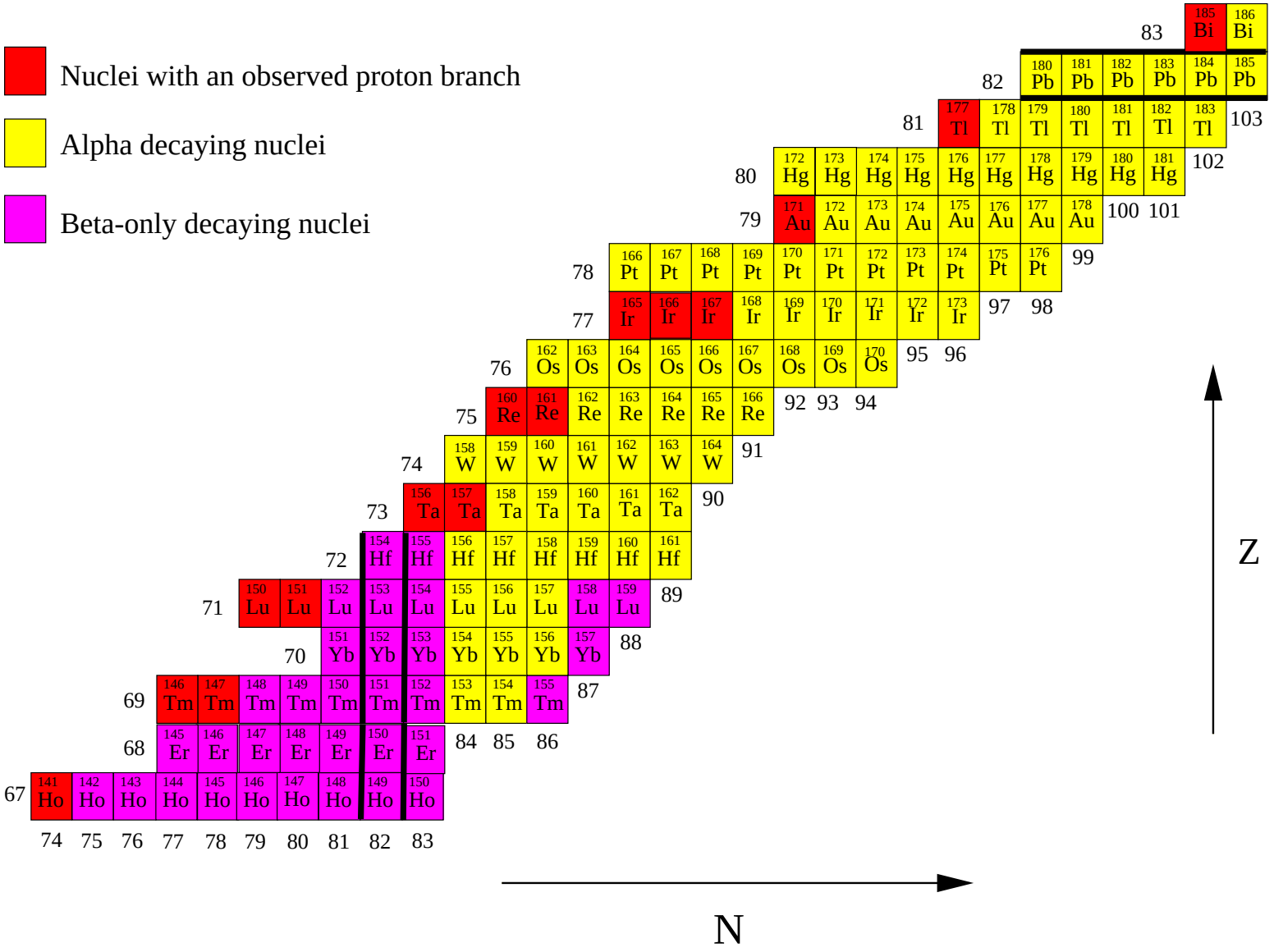

Figure 6.1: The proton dripline from Z=67-83

on level orderings in this region. It was deduced that a proton in the $s_{1/2}$ orbital formed the ground state in these nuclei, with the excitation energy of the $h_{11/2}$ state above the ground state increasing with Z.

Information from the proton decay of ^{167}Ir and the alpha decay chains from ^{167}Ir and ^{166}Os, terminating at ^{151}Tm and ^{150}Er, enabled deductions of proton separation energies for four nuclei from which proton decay has been unobserved, ^{163}Re, ^{159}Ta, ^{155}Lu and ^{151}Tm. These energies were consistent with either partial half-lives too long to be observable or a bound outer proton (^{151}Tm). For ^{155}Lu and ^{151}Tm a switching of the $s_{1/2}$ and $h_{11/2}$ was deduced, with the latter forming the ground state configuration. A similar switching of the levels occurs between ^{157}Ta and ^{153}Lu.

Calculations based on a low-seniority shell model for the wavefunctions of the proton emitters in this region $65 \leq Z \leq 82$, with a model space of 18 particles in degenerate $s_{1/2}$, $d_{3/2}$ and $h_{11/2}$ orbitals, and assuming a simple form for the spectroscopic factor, provided good agreement with the experimental measurements.

Proton emission from ^{141}Ho required a different approach since it is expected to have a high prolate deformation and has a half-life at least an order of magnitude different from any simple barrier penetration model prediction. A calculation using the multiparticle theory of Kadmensky and Bugrov produced a theoretical half-life in extremely good agreement with the measured value, assuming an occupancy of 1 for the $7/2^-[523]$ Nilsson orbital.

The large number of Q_p values provided by these experiments has allowed an extensive test of the predictions of the mass models. The Liran-Zeldes model predictions agree remarkably well with the data, while the model of Möller et al. performs relatively poorly. The measurements also provided a link to the known mass surface and enabled the calculation of 12 new ground state masses, via the $^{167}\text{Ir} \longrightarrow {}^{151}\text{Tm}$ and $^{166}\text{Os} \longrightarrow {}^{150}\text{Er}$ alpha decay chains.

6.2 Future research on drip-line nuclei

The scope for discovery of new proton emitters is now somewhat limited. Competition from fission becomes overwhelming as one tries to produce drip-line nuclei with Z>83 with fusion-evaporation reactions because they create the compound nuclei with high angular momentum. At lower masses, the Q window for observable proton decay is very small and it becomes increasingly unlikely with decreasing Z that a particular element will have a proton-unstable isotope with a half-life in the range accessible with current separator techniques (1 μs $\leq$ $t_{1/2}$ $\leq$ 1 s).

However, there are still gaps to be filled. Since the completion of the work described here, proton emission from ^{131}Eu has been observed at Argonne [Dav98]. This is another example of proton emission from a nucleus with a high prolate deformation (β_2=0.331 [Möl97]). As yet, no proton emitters have been observed in the elements La, Pr, Pm and Tb. The discovery of these would establish a continuous chain of 17 odd-Z proton emitters from Z=51-83 and would provide a wealth of nuclear structure information on nuclei with a wide range of deformation.

The technique of recoil decay tagging (RDT) has already been used to study the structure of ^{109}I ^{147}Tm and ^{157}Ta, and with the coupling of the Gammasphere germanium detector array to the FMA in late 1997, the prospect for further nuclear structure studies on drip-line nuclei is good. Gamma-ray studies of nuclear structure will provide more information for theoretical calculations of proton emission from deformed nuclei which is an archetypal example of the more general phenomenon of quantum tunneling in a deformed potential.

Bibliography

[Åbe97] S. Åberg, P.B. Semmes and W. Nazarewicz, *Spherical Proton Emitters*, submitted for publication (1997).

[And70] B.L. Anderson, B.B. Back and J.M. Bang, Nucl. Phys. **A147**, 33(1970)

[Bec69] F.D. Becchetti and G.W. Greenless, Phys. Rev. **182**, 1190 (1969).

[Ben85] T. Bengtsson and I. Ragnarsson, Nucl. Phys. **A346**, 14 (1985).

[Bet37] H.A. Bethe, Rev. Mod. Phys. **9**, 69 (1937).

[Bog90] D.D. Bogdanov, V.P. Bugrov and S.G. Kadmensky, Sov. J. Nucl. Phys. **52**, 229 (1990)

[Boh69] A. Bohr and B.R. Mottelson, *Nuclear Structure*, vol. 1, published by W.A. Benjamin, New York (1969)

[Bor91] V. Borrel, J.C. Jacmart, F. Pougheon, R. Anne, C. Détraz, D. Guillemaud-Mueller, A.C. Mueller, D. Bazin, R. Del Moral, J.P. Dufor, F. Hubert, M.S. Pravikoff and E. Roeckl, Nucl. Phys. **A531**, 353 (1991)

[Bug85a] V.P. Bugrov, S.G. Kadmensky, V.I. Furman and V.G. Khlebostoev, Sov. J. Nucl. Phys. **41**, 717 (1985)

[Bug85b] V.P. Bugrov, S.G. Kadmensky, V.I. Furman and V.G. Khlebostoev, Sov. J. Nucl. Phys. **42**, 34 (1985)

[Bug89] V.P. Bugrov and S.G. Kadmensky, Sov. J. Nucl. Phys. **49**, 967 (1989)

[Cha92] A.E. Champagne and M. Wiescher, Annu. Rev. Nucl. Part. Sci. **42**, 34

(1992)

[Cso93] A. Csoto, Phys. Lett. **B315**, 542 (1993)

[Dal84] P.J. Daly, in *Proc. 4th Nordic Meeting on Nuclear Physics*, Jyväsylä, Finland (1984)

[Dav92] C.N. Davids, B.B. Back, K. Bindra, D.J. Henderson, W. Kutschera, T. Lauritsen, Y. Nagame, P. Sugathan, A.V. Ramayya and W.B. Walters, Nucl. Instrum. Methods Phys. Res. B**70**, 358 (1992)

[Dav96] C.N. Davids, P.J. Woods, H.T. Pentillä, J.C. Batchelder, C.R. Bingham, D.J. Blumenthal, L.T. Brown, B.C. Busse, L.F. Conticchio, T. Davinson, D.J. Henderson, R.J. Irvine, D. Seweryniak, K.S. Toth, W.B. Walters, B.E. Zimmerman, Phys. Rev. Lett. **76**, 592 (1992).

[Dav97] C.N. Davids, P.J. Woods, J.C. Batchelder, C.R. Bingham, D.J. Blumenthal, L.T. Brown, B.C. Busse, L.F. Conticchio, T. Davinson, S.J. Freeman, D.J. Henderson, R.J. Irvine, R.D. Page, H.T. Pentillä, D. Seweryniak, K.S. Toth, W.B. Walters and B.E. Zimmerman, Phys. Rev. **C55**, 2255 (1997).

[Dav98] C.N. Davids, P.J. Woods, D. Seweryniak, A.A. Sonzogni, J.C. Batchelder, C.R. Bingham, T. Davinson, D.J. Henderson, R.J. Irvine, G.L. Poli, J. Uusitalo and W.B. Walters, to be published in Phys. Rev. Lett. March 1998.

[Fae84] T. Faesterman, A. Gillitzer, T. Hartel, P. Kienle and E. Nolte, Phys. Lett. **B137**, 23 (1984)

[Fes92] H. Feshback, *Theoretical Nuclear Physics: Nuclear Reactions*, published by John Wiley and Sons, inc., New York (1996).

[Gam28] G.Z. Gamow, Phys. **51**, 204 (1928).

[Gil87] A. Gillitzer, T. Faestermann, K. Hartel, P. Kienle and E. Nolte, Z. Phys

A326 107, 1987

[Gur29] R.W. Gurney, and E.U. Condon, Phys. Rev. **33**, 127, 1929

[Gur88] S.A. Gurvitz, Phys. Rev **A38**, 1747 (1988)

[Hag79] E. Hagberg, P.G. Hansen, P. Hornshøj, B. Jonson, S. Mattsson and P. Tidemand-Petersson, Nucl. Phys. **A318**, 29 (1979)

[Hen62] P. Henrici, *Discrete Variable Methods in Ordinary Differential Equations* ch. 6, Wiley, New York, 1962.

[Hof81] S. Hofmann, G. Münzenberg, W. Faust, F.P. Heßberger, W. Reisdorf, J.R.H. Schneider, P. Armbruster, K. Güttner and B. Thuma, in *Proc. 4th Int. Conf. on Nuclei Far From Stability*, Eds. P.G. Hansen and O.B. Nielsen, CERN 81-09, CERN, Geneva, 190 (1981)

[Hof82] S. Hofmann, W. Reisdorf, G. Münzenberg, F.P. Heßberger, J.R.H. Schneider and P. Armbruster, Z. Phys. **A305**, 111 (1982)

[Hof84] S. Hofmann, Y.K. Agarwal, P. Armbruster, F.P. Heßberger, P.O. Larsson, G. Münzenberg, K. Poppensieker, W. Reisdorf, J.R.H. Schneider and H.J. Schött, in *Proc. 7th Int. Conf. on Atomic Masses and Fundamental Constants*, Ed. O. Klepper, THD-Schriftenreihe Wissenschaft und Technik, 26 (1984)

[Hof89] S. Hofmann, in *Particle emission from Nuclei*, Eds. D.N. Poenaru and M.S. Ivascu, CRC Press, Inc., Florida (1989)

[Hof96] S. Hofmann, in *Nuclear Decay Modes*, Eds. D.N. Poenaru and W. Greiner, published by IOP, Bristol 1996

[Irv97] R.J. Irvine, C.N. Davids, P.J. Woods, D.J. Blumenthal, L.T. Brown, L.F. Conticchio, T. Davinson, D.J. Henderson, J.A. Mackenzie, H.T. Pentillä, D. Sew-

eryniak, W.B. Walters, Phys. Rev. **C55**, R1621 (1997).

[Jac70] K.P. Jackson, C.U. Cardinal, H.C. Evans, N.A. Jelley and J. Cerny, Phys. Lett. **B206**, 592 (1993)

[Jam88] A.N. James, T.P. Morrison, K.L. King, K.A. Connel, H.G. Price and J. Simpson, Nucl. Instr. and Meth. **A267**, 144 (1988)

[Kad71] S.G. Kadmenski, and V.E. Kalechtis, Sov J Nucl Phys. **12**, 37 (1971)

[Kad96] S.G. Kadmenski and V.P. Bugrov, Phys. At. Nucl. **59**, 399 (1996)

[Kle82] O. Klepper, T. Batsch, S. Hofmann, R. Kirchner, W. Kurcewicz, W. Reisdorf, E. Roeckl, D. Schardt and G. Nymen, Z. Phys **A305**, 125 (1982)

[Kle83] P. Kleinheinz, in *Proc. Int. Symp. on Electromagnetic Properties of Atomic Nuclei*, Eds. H. Horie and H. Ohnuma, Tokyo Institute of Technology, Tokyo (1983)

[Lar83] P.O. Larsson, T. Batsch, R. Kirchner, O. Klepper, W. Kurcewicz, E. Roeckl, D. Schardt, W.F. Feix, G. Nyman and P. Tidemand-Petersson, Z. Phys. **A314**, 9 (1983)

[Lir76] S Liran and N Zeldes et al., At. Data Nucl. Data Tables **17**, 431(1976)

[Liv93a] K. Livingston, Ph.D Thesis, University of Edinburgh (1993)

[Liv93b] K. Livingston, P.J. Woods, T. Davinson, N.J. Davis, S. Hofmann, A.N. James, R.D. Page, P.J. Sellin and A.C. Shotter, Phys. Rev. **C48**, 2151 (1993)

[Liv93c] K. Livingston, P.J. Woods, T. Davinson, N.J. Davis, S. Hofmann, A.N. James, R.D. Page, P.J. Sellin and A.C. Shotter, phys. Lett. **B312**, 46 (1993)

[Liv93d] K. Livingston, P.J. Woods, T. Davinson, N.J. Davis, S. Hofmann, A.N. James, R.D. Page, P.J. Sellin and A.C. Shotter, Phys. Rev. **C48**, 2151 (1993)

[Mac65] R.D. Macfarlane, Phys. Rev. **137/6B**, 1448 (1965)

[Moh91] M.F. Mohar, D. Bazin, W. Benenson, D.J. Morrissey, N.A. Orr, B.M. Sherril, D. Swan, J.M. Winger, A.C. Mueller and D. Guillemaud-Mueller, Phys. Rev. Lett. **66**, 1571 (1991)

[Möl81] P. Möller and J.R. Nix, Nucl. Phys. **361**, 117 (1981)

[Möl88] P. Möller and J.R. Nix, At. Nucl. Data Tables **492**, 349 (1989)

[Möl95] P. Möller, J.R. Nix, W.D. Myers and W.J. Swiatecki, Atomic Data and Nuclear Data Tables **59**, 185 (1995)

[Möl97] P. Möller, J.R. Nix and K.L. Kratz, At. Nucl. Data Tables **66**, 131(1997)

[Mun79] G. Münzenberg, W. Faust, S. Hofmann, P. Armbruster, K. Güttner and H. Ewald, Nucl. Instr. and Meth. **161**, 65 (1979)

[Mye77] W.D. Myers, *Droplet Model of Atomic Nuclei*, Published by IFI/Plenum, New York, 1977.

[Nil55] S.G. Nilsson, Dan. Mat.-Fys. Medd **29**, 16 (1955)

[Pag92] R.D. Page, P.J. Woods, R.A. Cunningham, T. Davinson, N.J. Davis, A.N. James, S. Hofmann, K. Livingston, P.J. Sellin and A.C. Shotter, Phys. Rev. Lett. **68**, 1287 (1992). [Pag96] R.D. Page, P.J. Woods, R.A. Cunningham, T. Davinson, N.J. Davis, A.N. James, K. Livingston, P.J. Sellin and A.C. Shotter, Phys. Rev. **C53**, 660 (1996).

[Per72] C.M. Perey and F.G. Perey, Nuclear Data Tables **10**, 539 (1972)

[Poe89] *Particle Emission from Nuclei*, vol. 3, Eds. D.N. Poenaru and M.S.

Ivascu, CRC Press, Inc., Florida (1989)

[Pra73] HC Pradhan, Y Nogami and J Law, Nucl Phys A201 357 (1973)

[Pol98] G.L. Poli - paper in preparation

[Ras66] J.O. Rasmussen, in *Alpha,beta and gamma ray spectroscopy,* Ed. K. Seigbahn, North-Holland, Amsterdam, 1966, 701.

[Sat83] G.R. Satchler, *Direct Nuclear Reactions*, Oxford Science Publications (1983)

[Sel92a] P.J. Sellin, P.J. Woods, D. Branford, T. Davinson, N.J. Davis, D.G. Ireland, K. Livingston, R.D. Page and A.C. Shotter, S. Hofmann, R.A. Hunt A.N. James, M.A.C. Hotchkins, M.A. Freer and S.L. Thomas, Nucl. Instrum. Methods Phys. Res. A**311**, 217 (1992)

[Sel92b] P.J. Sellin, Ph.D Thesis, University of Edinburgh (1992)

[Sew97] D. Seweryniak, C.N. Davids, W.B. Walters, P.J. Woods, I. Ahmad, H. Amro, D.J. Blumenthal, L.T. Brown, M.P. Carpenter, T. Davinson, S.M. Fischer, D.J. Henderson, I. Hibbert, R.J. Irvine, R.V.F. Janssens, T.L. Khoo, C.J. Lister, J.A. Mackenzie, D. Nisius, C. Parry, R. Wadsworth, Phys. Rev. **C55**, 2137(1997)

[Str67] V.M. Strutinsky, Nucl Phys **A95**, 420(1967)

[Str68] V.M. Strutinsky, Nucl Phys **A122**, 1 (1968)

[Tan85] I. Tanihata, H. Hamagaki, O. Hashimoto, Y. Shida, N. Yoshikawa, K. Shigomoto, O. Yamakawa, T. Kobayashi and N. Takahashi, Phys. Rev. Lett. **55**, 2676 (1985)

[Tan88] I. Tanihata, T. Kobayashi, O. Yamakawa, S. Shimours, K. Ekuni, K. Su-

gimoto, N. Takahashi, T. Shimoda and H. Sato, Phys. Lett. **B206**, 592 (1993)

[Ver96] J. Vervier, Progress in Nucl. and Part. Phys. **37**, 435 (1996).

[Woo54] R.D. Woods and D.S. Saxon, Phys. Rev. **95**, 577 (1954)

[Woo89] P.J. Woods, S.J. Bennet, M. Freer, B.R. Fulton, R.D. Page, K.A. Connel, R.A. Cunningham, J, Groves, A.N. James, M.A.C. Hotchkins and W.D.M. Rae, Nucl. Instr. and Meth. **A276**, 195 (1989)

[Woo97] P.J. Woods and C.N. Davids, Annu. Rev. Nucl. Part. Sci. 47, 541(1997)

[Woo98] P.J. Woods, private communication